

Control of dipolar collisions in the quantum regime

by

Marcio H. G. de Miranda

B.Sc., Federal University of Pernambuco, 2002

M.Sc., Federal University of Pernambuco, 2004

M.A., University of Colorado at Boulder, 2008

A thesis submitted to the
Faculty of the Graduate School of the
University of Colorado in partial fulfillment
of the requirements for the degree of
Doctor of Philosophy
Department of Physics

2010

This thesis entitled:
Control of dipolar collisions in the quantum regime
written by Marcio H. G. de Miranda
has been approved for the Department of Physics

Dr. Jun Ye

Dr. Deborah S. Jin

Date _____

The final copy of this thesis has been examined by the signatories, and we find that both the content and the form meet acceptable presentation standards of scholarly work in the above mentioned discipline.

Miranda, Marcio H. G. de (Ph.D., Physics)

Control of dipolar collisions in the quantum regime

Thesis directed by Professor Dr. Jun Ye

The preparation of ultracold polar molecular gases close to quantum degeneracy opens novel research prospects ranging from dipolar quantum many-body physics to ultracold chemistry. With a near quantum degenerate gas of fermionic $^{40}\text{K}^{87}\text{Rb}$ polar molecules, this thesis presents studies on dipolar collision and chemical reaction dynamics, exhibiting long range interactions and spatial anisotropy. With full control over the internal quantum state of the molecules, we show how quantum statistics of the molecule determines the rate of chemical reactivity in the limit of vanishing collisional energy. Manipulating the interaction potential between indistinguishable polar molecules by means of control over the dipole moment of the molecules, we study the dramatic influence of the dipolar interaction on the chemical reaction rate. In particular, we show that the chemical reaction rate increases steeply with the dipole moment following a characteristic power law. This power law reflects the long-range character of the dipole-dipole interaction. Studies on thermodynamics in the molecular quantum gas reveal the anisotropic properties of the dipolar interaction. Finally, combining control over the molecular dipole moment and the dimensionality of the spatial confinement, we suppress inelastic collisions between polar molecules by up to two orders of magnitude. The suppression of inelastic collisions is achieved by changing the geometry of the confinement from three-dimensional to two-dimensional optical trapping. With the combination of a sufficiently tight 2D confinement and Fermi statistics of the molecules, two polar molecules approach each other only in a “side-by-side” collision, where the inelastic collisions are suppressed by the repulsive dipole-dipole interaction. This suppression requires quantum state control of internal (electronic, vibrational, rotational and hyperfine states) and external (harmonic oscillator levels of the optical lattice) degrees of freedom of

the molecules. This is a fundamental advance in stabilizing a polar molecular gas for future applications in quantum many-body systems.

Dedication

To my mother Leda, to my brother Marcelo and to my dear wife Fabiana for all love and support.

Acknowledgements

To be a physicist is not an easy thing. If you want to be a fully realized physicist one day, you have to go through a Ph.D. program, for most of the average people. I chose to follow this path in 1998 when I started as a student in the Federal University of Pernambuco in my home town Recife. After spending 4 years to get bachelors and 2 years to get my masters, I decided to do a Ph.D. when my application was accepted at the University of Colorado at Boulder.

My Ph.D. work would be impossible without help of many people. I will start by thanking Jun Ye for giving me the chance to work in his lab, for providing such an amazing scientific environment, and for being on my side in all decisive moments. I thank Deborah Jin for her attention and patience. I thank John Bohn for his patience and for answering my dumb questions with a good mood. Thanks to Ana Maria Rey for stimulating discussions. Thanks to John Hall for providing a stable laser source and lots of nice conversations about lasers, physics, and life in general.

Thanks to Seth Foreman (“A” as in America), Daren Hudson, Michael Thorpe, Matt Stowe, and Thomas Schibili for interesting discussions and frequency comb secrets that they shared with me.

Thanks to the KRb group that I was part of. Thanks to Avi Pe’er who is an incredibly patient person, very sharp and fun to work with. Thanks to Silke Ospelkaus for all she taught me about cold atoms and molecules and for all that she did for me. Silke is the advisor that any student would want to have. Thanks to Kang-Kuen Ni who taught me so

much and sided with me most of the time despite of some disagreements. Thanks to Dajun Wang (“Dajunio”) who is a hard working and sharp scientist. Thanks to Brian Neyenhuis who is a very sharp guy and patient. Thanks to my French friend Amodsen Chotia who is smart, has a nice sense of humor, and was a pleasure to work with. Thanks to another French friend Goulven Quéméner (Goulvinho “vote em mim”) for many good discussions and explanations, for his theoretical support, and for his nice sense of humor with no French accent. Thanks to Steve Moses who is going to be in charge of our frequency comb from now on and who is also an excellent reinforcement for our group.

Thanks to my frequency comb friends Dylon Yost, Kevin Cossel, Travis Briels, Ticijana Ban, Thomas Allison, Aleksandra Matyba, Arman Cingoz, Florian Adler, and Piotr Maslowski.

Thanks to my Sr friends Sebastian Blatt, Andrew Ludlow, Martin Boyd, Matt Swallows, Travis Nicholson, Michael Martin, Michael Bishof, Gretchen Campbell, Tanya Zelevinzky, Thomas Zanon, Jan Thomsen, Yige Lin, Ben Bloom, and Jason Williams.

Thanks to my OH friends Brian Sawyer, Benjamin Stuhl, Eng Hiang Yeo, Matthew Hummon, and Yong Xia.

Thanks to my friends from theory and soccer games such as Murray Holland, Javier Von Stecher, Dominic Meiser, Brandon Peden, David Tieri, and Ron Pepino.

Thanks to the electronic shop staff Terry Brown (the master Yoda of microwave electronics), James Fung-A-Fat, Michael J. Whitmore, David J. Tegart, Carl Sauer and Paul Beckingham for the excellent development and support with electronics.

Thanks also to J.R. Raith, Michael Page and Alan Dunwell for the excellent support on computers.

Thanks to the machine shop staff Hans Green, Kim R. Hagen, Paul Ariel, Todd R. Asnicar, Thomas P. Foote, Blaine P. Horner, Tracy Keep and David Alchenberger for high quality of technical assistance.

Thanks to the supply office staff Jeff Sauter, Brian Lynch, Randall Holliness, and

William Blue for providing such efficient support. Thanks to Diana Moreland and Krista Beck for being so organized and helpful. Thanks to Agnieska Lynch for taking care of financial paper work. Thanks to Jeanne M. Nijhowne for her efficient work and kindness.

Thanks to my friends Fan-Chi Lin, Yu-Li Liang, Oliver Lin, Ricardo Jimenes, Sungsoo Choi, Eduardo Calleja, Quan Zhang and Qing Li, Max Brown, Shannon Sankar, Chester Rubbo, and Qing Chao.

Thanks to Mike Dubson for help me with my comps II exam.

Thanks to my my dear Brazilian friends Paulo Berton, Leila Grieger, Helena Berton, Doris Berton, Felipe Nievinsky, Giovana Vazatta, Jose D’Incao, Valeria Gabarra, Eloisa D’Incao, Nick McCulloch (the one who has a Brazilian spirit) and Daiana McCulloch for being so entertaining, nice and extremely helpful in hard times.

Thanks to professor Lúcio Hora Acioli for assisting me with my masters and helping me come to JILA.

Thanks to my mother Leda and to my brother Marcelo for their love, dedication, care and sacrifice that they did in order to raise me like a honest, educated and hard working person. Thanks to my dear wife Fabiana for all her love, patience, sacrifice, care and for being so understanding when I had to spend so much time working and not with her.

Thanks to CAPES and Fulbright for financial support.

Contents

Chapter	
1	Introduction 1
1.1	From ultracold atoms to ultracold molecules 1
1.2	Dipolar interactions 4
1.3	Overview of this thesis 5
1.4	Outline of the thesis 7
2	Experimental Apparatus 9
2.1	From ultracold K and Rb atoms to ultracold ground-state molecules 10
2.1.1	Preparation of a near quantum-degenerate mixture of ^{40}K and ^{87}Rb 10
2.1.2	Feshbach molecule creation 11
2.1.3	Two-photon coherent transfer - STIRAP 12
2.1.4	Preparation of ground-state polar molecules 23
2.2	Essential manipulation techniques for ground-state polar molecules 26
2.2.1	Electric dipole moment of the molecules 27
2.3	Tuning the geometry of the external confinement - 1D Optical Lattice 29
3	Dipolar $^{40}\text{K}^{87}\text{Rb}$ Molecules in 3D geometry 32
3.1	Bimolecular chemical reactions at ultracold temperature 33
3.2	The role of quantum statistics in determining the chemical reaction rate 34
3.3	The experimental system 35

3.4	Bimolecular chemical reactions at vanishing dipole moment	36
3.4.1	p-wave collisions	36
3.4.2	s-wave collisions	41
3.5	Dipolar collisions with ultracold $^{40}\text{K}^{87}\text{Rb}$ in 3D geometry	42
3.5.1	Dipoles and chemical reactions	42
3.5.2	The experiment	44
3.5.3	Controlling chemical reactions by means of the dipole moment of the molecules	44
3.5.4	Thermodynamics of dipolar collisions	48
3.5.5	Anisotropy of heating	49
4	Polar Molecules in an 1D Optical Lattice: Going to 2D Geometry	54
4.1	Atoms in an one-dimensional optical lattice	55
4.1.1	Optical dipole traps for neutral atoms and molecules	55
4.1.2	One-dimensional optical lattice	57
4.1.3	Experimental realization of a 1D optical lattice	59
4.1.4	Quantum mechanical description of a particle confined in a periodic potential: Bloch bands	60
4.2	Characterizing the optical lattice	65
4.2.1	Measuring the trapping frequencies by parametric heating	65
4.2.2	Kapitza-Dirac Scattering	67
4.3	Loading atoms into the optical lattice	69
4.3.1	Loading atoms in the optical lattice	72
4.4	Probing the quasimomentum distribution of atoms in optical lattices.	74
4.5	$^{40}\text{K}^{87}\text{Rb}$ molecules in the optical lattice	79
5	Suppression of Inelastic Collisions in 2D geometry	85
5.1	Chemical Reaction Rates and Stereodynamics	86

	xi
5.2 Collisions between Polar Molecules in Quasi-2D Geometry	87
5.3 Band Mapping of Molecules	90
5.4 Suppression of Inelastic Collisions in the Optical Lattice	95
6 Conclusion and Future Work	103
6.1 Conclusion	103
6.2 Future work	103
Bibliography	105

Figures

Figure

- 1.1 p-wave centrifugal barrier for dipolar collisions between fermionic polar molecules. (A), The effective intermolecular potential for fermionic molecules at zero electric field. At intermediate intermolecular separation, two colliding molecules are repelled by a large centrifugal barrier for p-wave collisions. (B), For a relatively small applied electric field, the spatially anisotropic dipolar interactions reduce the barrier for head-to-tail collisions and increase the barrier for side-by-side collisions. From [40]. 8
- 2.1 Potential curves for ^{40}K - ^{87}Rb molecules and energy levels used for STIRAP transfer of Feshbach molecules to ground-state. The Feshbach molecules are formed in the initial state $|i\rangle = a^3\Sigma$. The intermediate state $|e\rangle = (v' = 23)$ is in the electronically excited potential of $2^3\Sigma$, and the final state $|g\rangle$ is in the ro-vibronic ground state $N = 0, v = 0$ of $X^3\Sigma$. The initial and the final states are about 125 THz apart from each other. This figure is reproduced from reference [26]. 14

- 2.2 The schematic diagram of STIRAP pulse sequence. In (a), the molecules are in the initial state. In (b), the intensity of laser 2 is adiabatically ramped up, coupling states $|e\rangle$ and $|g\rangle$. In (c), the transfer of molecules in state $|i\rangle$ to state $|g\rangle$ happens by adiabatically ramping the intensities of laser 2 down and laser 1 up. In (d), laser 1 intensity is ramped down, and (e) is the end of the process, where about 90% of the Feshbach molecules are transferred to the ground state. 16
- 2.3 Schematic picture of the spectrum of the frequency comb. The two CW lasers at frequencies ν_{690} and ν_{970} are phase-locked to the comb. 18
- 2.4 Frequency comb laser set up. This schematic diagram shows the Ti:S cavity (red box), the f-2f interferometer (blue box), the heterodyne beats for f_{rep} (dashed blue box), and the ν_{690} (dashed red box) and ν_{970} (orange box) phase-locks. The the light from the Ti:S is then spectrally broadened in the photonic crystal fiber (PCF) to cover a range from 500 nm to 1100 nm. The input power to the PCF is 680 mW. f_{ceo} is stabilized via a f-2f interferometer. f_{rep} is phase-locked to a narrow YAG laser at 1064 nm. The several optical components are used to deliver the light with the right wavelength to their respective heterodyne beat set ups. F2, F3, F4, F5, and F6 are all band pass filters with FWHM 10 nm, at 532, 690, 1064, 1064, and 970 nm respectively. F4 also is used as a “mirror” to reflect 970 nm light. F1 is a high pass filter with R(532 nm)/T(600 nm - 850 nm). BS1 and BS2 are dichroic beam splitters where the reflection and transmission of the first are R(950 nm - 1100 nm)/T(500 nm - 920 nm), and for the second are R(532 nm)/T(920 nm - 1100 nm). 19

- 2.5 Locking electronics for f_{rep} . The beat signal of f_{rep} and the Nd:YAG laser is amplified, goes to a band pass filter (BPF), and then to a home built digital phase detector, where the frequency is divided and the signal is mixed to a direct digital synthesiser (DDS). The DDS is referenced to a 10 MHz commercial quartz clock (Wenzel Associates). The error signal goes to a home built loop filter, where the signal is divided and sent to a PZT driver to a fast PZT (≈ 50 kHz bandwidth), and to a slow integrator box (with time constant of ≈ 45 seconds), to a high voltage driver to a slow PZT. Using both fast and slow PZTs guarantee short and long term stability for f_{rep} 20
- 2.6 f_{ceo} detection via f-2f interferometer. From a broad spectrum, for f_{ceo} detection, the important wavelengths are 532 nm (high frequency portion) and 1064 nm (low frequency portion). The low frequency portion is doubled in a BBO crystal, and overlapped with the high frequency portion. The difference between the doubled low frequency portion and the high frequency portion is f_{ceo} . Figure reproduced from reference [55]. 21
- 2.7 Locking electronics for f_{ceo} . The f_{ceo} beat signal is amplified, fed to a band pass filter (BPF), and then to a home built digital phase detector, where the frequency is divided and the signal is mixed to a direct digital synthesiser (DDS). The DDS is referenced to a 10 MHz commercial quartz clock (Wenzel Associates). The error signal goes to a home built loop filter, to a bias box, which puts an offset in the output voltage going to an AOM driver, feeding back the AOM that controls the intensity of the Verdi 10W laser. 22
- 2.8 Raman laser system for 970 nm transition. This system has three outputs: one for a wavemeter, one for the frequency comb and one for the STIRAP transfer. The power of the laser is amplified by using a tapered amplifier. . . 23

- 2.9 Raman laser system for 690 nm transition. This system has three outputs: one for a wavemeter, one for the frequency comb and one for the STIRAP transfer. The power of the laser is amplified by using another diode laser (slave laser) seeded with ≈ 1 mW of power from the master laser. The slave laser is locked via injection lock. 24
- 2.10 Timing diagram of the coherent two-photon transfer (STIRAP) from Feshbach molecules to the absolute rovibrational ground state $X^1\Sigma (v = 0)$. (a) STIRAP pulse sequence, where I_1 and I_2 are the intensities of laser 1 and laser 2. (b) Measured population in the initial Feshbach state during the STIRAP pulse sequence. Starting with $4 \cdot 10^4$ Feshbach molecules, the molecules are coherently transferred to the rovibrational ground state $X^1\Sigma (v = 0)$ by the first pulse sequence ($t = 15$ to $20\mu\text{s}$). The rovibrational ground state molecules are invisible to the detection light. Reversing the pulse sequence, $X^1\Sigma (v = 0)$ molecules are converted back to weakly bound Feshbach molecules ($t = 45$ to $t = 50\mu\text{s}$). This figure is reproduced from reference [48]. 25
- 2.11 Comparison of the kinetic energy of the Feshbach molecules before STIRAP transfer (blue circles) and after a round-trip STIRAP process (red circles). The latter can be interpreted as an upper limit on the kinetic energy of the rovibrational ground state molecules. The temperature of both clouds is extracted by time of flight expansion analysis. We extract $T = 400(15)$ nK for the Feshbach molecules and $T = 430(20)$ nK for rovibrational ground-state molecules. The analysis shows that the transfer process does not cause any noticeable heating on the molecules. This figure is reproduced from reference [48]. 26

- 2.12 Stark spectroscopy of the singlet $v = 0$ molecules. The bottom panel shows the Stark shift of the rovibrational ground-state of the singlet potential ($v = 0, N = 0$ of $X^1\Sigma$), and the top panel shows the shift of the $v = 0, N = 2$ state. The systematic error in the applied electric field is 3% (horizontal error bars). The level difference between $N = 0$ and $N = 2$ is 6.6836(5) GHz, which yields a rotational constant B of 1.1139(1) GHz. Given the measured B, the fit of the Stark shift (line in lower panel) gives a permanent electric dipole moment of 0.566(17) D. The theory curves for $N = 2$ for different $|m_N\rangle$ projections (lines in upper panel) are calculated using the measured B and the dipole moment derived from the $N = 0$ fit. This figure is reproduced from reference [26]. 27
- 2.13 Calculated dipole moment versus applied DC electric field. In our experiment we can go to electric fields as high as 5.0 kV/cm. 28
- 2.14 Schematic figure of the electric field plates and 1D optical lattice set up. The maximum output power of the fiber is 1.7 W. The polarization is set to be parallel to the optical table. The intensity of the optical lattice is stabilized via an AOM, which also shifts the frequency by +80 MHz. 30
- 3.1 Hyperfine structure of rovibronic ground-state $^{40}\text{K}^{87}\text{Rb}$ molecules at a magnetic field of 545.9 G. Here we have 36 nuclear spin states by their spin projections, m_I^{Rb} and m_I^K . The energy spacing between hyperfine states is $h \cdot 130$ kHz for $|m_I^K| = 1$ and $h \cdot 760$ kHz for $|m_I^{Rb}| = 1$. By comparison, at a temperature of 300 nK, the molecules thermal energy is equivalent to $h \cdot 6$ kHz, which is more than an order of magnitude smaller than the spin flip energy. Molecules can be prepared in either a single state or in a mixture of The $| -4, 1/2 \rangle$ and the lowest-energy state $| -4, 3/2 \rangle$ (open ellipses). Figure reproduced from reference [39]. 37

- 3.2 Transfer from the rovibrational ground state $| -4, 1/2 \rangle$ to the absolute ground state $| -4, 3/2 \rangle$ via coherent Rabi transfer. The intermediate state is in the rotational level $N = 1$ and it is a mixed state with $g \approx 5 \%$ 38
- 3.3 Inelastic collisions between spin-polarized (indistinguishable) or different spin-state (distinguishable) fermionic molecules in the rovibronic ground state of $^{40}\text{K}^{87}\text{Rb}$. (A) Data showing the time dependence of the molecule number density. Here the molecules are prepared in a single hyperfine state, $| -4, 1/2 \rangle$, and the molecular density decays slowly with a rate coefficient of $3.3(\pm 0.7) \cdot 10^{12} \text{ cm}^3 \text{ s}^{-1}$ at $T = 250 \text{ nK}$. (B) Loss rate coefficient as function of the temperature. The loss rate increases linearly with temperature for spin-polarized molecules, which collide via p-wave [inset in (A)] at low temperature. Data were taken for molecules prepared in either $| -4, 1/2 \rangle$ (solid circles) or the lowest-energy state $| -4, 3/2 \rangle$ (open triangles). A linear fit (solid line) to the $| -4, 1/2 \rangle$ data yields the temperature-dependent loss rate to be $1.2(\pm 0.3) \cdot 10^5 \text{ cm}^3 \text{ s}^{-1} \text{ K}^{-1}$. For the $| -4, 3/2 \rangle$ case, where the collisional loss can only be due to chemically reactive scattering, the loss rate is similar. The dotted and dashed lines are the predictions from the QT and MQDT models, respectively. When the molecules are prepared in a mixture of the $| -4, 1/2 \rangle$ and $| -4, 3/2 \rangle$ states (solid squares), we observe a temperature-independent decay rate that is 10 to 100 times that for the spin-polarized case. Figure reproduced from reference [39]. 41
- 3.4 p-wave barrier for $^{40}\text{K}^{87}\text{Rb}$ dipolar collisions “head-to-tail” (solid curve in blue) and “side-by-side” (solid curve in red). The dashed line represents the p-wave in the absence of electric-field. 43

3.5 Two-body inelastic loss for fermionic polar molecules. (a), We extract the inelastic loss rate coefficient, β , from a fit (solid lines) to the measured time evolution of the trapped molecular gas density. Data are shown here for induced dipole moments of $d = 0.08$ D (open triangles) and $d = 0.19$ D (filled circles), and $T_0 = 300$ nK. (b), Data points show β/T_0 plotted as a function of d . The dashed line shows a fit to a simple model based on the quantum threshold behavior for tunneling through a dipolar-interaction-modified p-wave barrier. The solid line shows the result of a more complete quantum scattering calculation. Inset, the calculated dependence of d on the applied electric field, E . Figure reproduced from reference [40]. 45

3.6 p-wave barrier for dipolar collisions between fermionic $^{40}\text{K}^{87}\text{Rb}$ molecules. (a), The effective intermolecular potential for fermionic molecules at zero electric field. At intermediate intermolecular separation, two colliding molecules are repelled by a centrifugal barrier for p-wave collisions. (b), For an applied electric field, the spatially anisotropic dipolar interactions reduce the barrier for “head-to-tail” collisions and increase the barrier for “side-by-side” collisions. (c), Height of the p-wave barrier as a function of dipole moment. Dipolar interactions lower the centrifugal barrier for $M = 0$ collisions (V_0) and raise the barrier for $M = \pm 1$ collisions (V_1). The lowering of the $M = \pm 1$ barrier at very large dipole moments is due to mixing with higher L partial waves ($L = 3, 5, 7, \dots$). Figure reproduced from reference [40]. 46

- 3.7 Normalized fractional heating rate, $\dot{T}/T_0^2 n$, versus the dipole moment. The heating rate is extracted from a linear fit to the initial temperature increase and is then normalized by the initial density and temperature of the ensemble. The solid line is the expected heating rate, given by $\dot{T}/T_0^2 n = (\beta/T_0)/12$. Typical experimental initial conditions are $n = 0.3 \cdot 10^{12} \text{ cm}^{-3}$ and $T_0 = 0.5 \mu\text{K}$, and the absolute heating rate ranges from $0.5 \mu\text{K s}^{-1}$ at zero electric field to $2 \mu\text{K s}^{-1}$ at our highest electric fields. Figure reproduced from reference [40]. 50
- 3.8 Cross-dimensional rethermalization in the polar molecule gas. Shown as a function of dipole moment, d , for $T_z > T_x$ (a-c) and $T_z < T_x$ (d-f). The experimental data shows difference between heating the gas in the vertical direction (a-c) and heating it in the horizontal directions (d-f). This provides evidence for the strong anisotropic characteristic of dipolar interactions. The electric field is applied along the \hat{z} direction. Figure reproduced from reference [40]. . 52
- 4.1 Illustrative contour plot of one-dimensional optical lattice potential. (a) Normalized potential in false color for $w_0 = \lambda$. (b) Potential for $w_0 = 250\lambda$. The point with maximum density are the anti-nodes where, for a red-detuned optical lattice, the particles will be trapped. In our case, the lattice beam waist is $w_0 \approx 250 \mu\text{m}$ 58
- 4.2 Optical lattice's trap frequencies versus the trap depth for ^{87}Rb . This two plots show the axial frequency ν_z compared to the radial frequency ν_r . The confinement in the axial direction is much tighter than the radial direction. The optical lattice parameters are: $\lambda = 1064 \text{ nm}$, and the beam waist is $250 \mu\text{m}$ 60

- 4.3 Bloch bands in the one-dimensional optical lattice. Energy versus quasimomentum in the first Brillouin zone for different lattice depths. The lattice depths are 0, 10, 15, and 20 E_{rec} . As the lattice height increases, the separation between the Bloch bands also increases and the energy levels flatten out. 62
- 4.4 First four energy levels versus the lattice depth with quasimomentum $q = 0$, for an atom in an optical lattice. For lattice depths above $30E_{rec}$, the spacing between the energy levels approaches $\hbar\omega_z$ like a harmonic oscillator energy. 63
- 4.5 Semi-log plot of tunneling time in an 1D optical lattice versus lattice depth. Dotted blue line is for ^{40}K and red dashed line is for ^{87}Rb . For our typical conditions, the tunneling time for ^{40}K is 300 ms (for 19 E_{rec}^K) and for ^{87}Rb is 1 s (for 42 E_{rec}^{Rb}). 65
- 4.6 Trap frequency measurement for Feshbach molecules ^{40}K - ^{87}Rb via parametric heating. σ is the molecular cloud width in the \hat{z} direction. The center frequency is 44 kHz, which indicates that the axial frequency of the optical lattice is 22 kHz. The ramp procedure for this measurement is similar to the one described in chapter 5 in fig. 5.2 except with a sudden turn off of the end of the ramp. 67
- 4.7 Ramp procedure to measure trap depth of the optical lattice. The depth measurement is done with a ^{87}Rb BEC. The optical lattice is adiabatically pulsed on and briefly switched off in order to excite ^{87}Rb atoms to higher bands. The hold time is varied on the order of tens of microseconds. The time of flight is 5 ms, and the lattice height is 42 E_{rec} 69
- 4.8 ^{87}Rb BEC matter-wave diffraction into discrete momentum components. 70

4.9	Extracted relative population of momentum components versus pulse duration. The lines show a fit to eq. 4.19. The optical lattice depth as a free parameter, and the extracted one from the data is $42 E_{rec}$. The optical lattice parameters are $\lambda = 1064$ nm, beam waist of $250 \mu\text{m}$, and laser power of 1 W. The three curves show the $0\hbar k$ (solid blue), $\pm 2\hbar k$ (solid green), and $\pm 4\hbar k$ (solid red) momentum components.	71
4.10	Energy gap between lowest and first excited Bloch bands for different quasimomenta. Solid blue line is for $q = 0$, dashed green line is for $q = 0.5 \hbar k$, and red dotted line is for $q = \hbar k$	72
4.11	Ramping procedure to adiabatically load ^{40}K and ^{87}Rb in the optical lattice. The optical lattice depth for ^{87}Rb is $42 E_{rec}^{Rb}$ and for ^{40}K is $19 E_{rec}^K$	73
4.12	Lifetime of ^{87}Rb and ^{40}K atoms and respective heating rates in the optical lattice.	74
4.13	Calculated functions for the distribution in quasimomentum space at the first Brillouin zone in the optical lattice. Red dotted curve is a gaussian function, green dashed curve is a Heaviside function, and solid blue line is the convolved curve that is used to fit the atomic cloud along the lattice axis.	75
4.14	Band mapping with filtering of ^{40}K in higher bands. The optical lattice is adiabatically ramped up exponentially in 150 ms to $17.7 E_{rec}$. At the beginning the optical lattice and the optical trap are combined to hold the atoms against the gravity. The filtering is done for two different lattice heights: $3.2 E_{rec}$, and $14.5 E_{rec}$	76

4.15	Band mapping for the filtering procedure with ^{40}K atoms. (a), and (c) are the atomic cloud images taken with time of flight of 18 ms. The initial temperature of the atoms in (a) is 350 nK and in (b) is 400 nK. The vertical profiles are shown in (b) and (d). In (b) all atoms are in the first Brillouin zone, while in (d) about 28% of the atoms are in the second Brillouin zone. However, a significantly difference in population of bands is observed in the two cases due to a different optical lattice heights ($3.2 E_{rec}$, and $14.5 E_{rec}$) applied for the filtering procedure(see fig. 4.14).	79
4.16	Ramping procedure for formation of ground state $^{40}\text{K}^{87}\text{Rb}$ molecules in the optical lattice. The final lattice depth is $60 E_{rec}^{KRb}$	81
4.17	Heating rate for $^{40}\text{K}^{87}\text{Rb}$ in the optical lattice. The optical lattice depth is $60 E_{rec}^{KRb}$ depth.	82
4.18	Ramp procedure for forming/loading ground state molecules in the optical lattice. The number 1 indicates where the ground state molecules are formed. Then the molecules are loaded in the optical lattice. The number 2 indicates where the ground state molecules are formed. In this case the molecules are formed in the fully ramped up optical lattice. The arrow with the note “Variable Height” means that the final value of the lattice is changed. The maximum height (depth) value that the lattice can go is $120 E_{rec}^{KRb}$	82
4.19	Measurement of the number of ground state molecules versus the optical lattice depth. The black open circles show the molecule number when the molecules are formed in the fully ramped-up optical lattice. The red open squares show the molecule number when the molecules are formed in the partially ramped up optical lattice.	83

- 4.20 Ramp procedure for forming/loading ground state molecules in the optical lattice. The number 3 indicates where the ground state molecules are formed. The molecules are formed in a partially ramped up optical lattice. The arrow with the note “Variable Height” means that the partial value of the lattice is changed. The final height (depth) value of the lattice is $120 E_{rec}^{KRb}$ 84
- 5.1 Quantized stereodynamics of ultracold chemical reactions in quasi-2D. (A) A quasi-2D geometry for collisions is realized for polar molecules confined in a one-dimensional optical lattice. An external electric field is applied along the tight confinement axis. (B) The lowest three adiabatic potentials for collisions are shown schematically as a function of the intermolecular separation, R . These three channels are ordered with increasing magnitude of the centrifugal barrier. The arrows indicate the change in the potential for an increasing external electric field, and hence a growing induced dipole moment. (C) Three different cases are shown schematically for each of the three lowest collision channels. The lowest energy collision channel occurs when two molecules are prepared in different internal states (indicated here by the colors of the molecules). The second channel is realized when two identical molecules are prepared in different vibrational levels v for their \hat{z} motions. The third case has a much reduced loss rate as a consequence of an increased centrifugal barrier when the two identical molecules are prepared in the same vibrational level along \hat{z} . Figure reproduced from reference [74]. 91

- 5.2 Ramp procedure for transferring atoms from the dipole trap to an optical lattice as well as for band mapping for molecules. Molecules are formed after an 150 ms adiabatic ramp. A non-thermal distribution is created by using parametric heating by pulsing a sinusoidal wave with $300 \mu\text{s}$. The band mapping is done by linearly ramping down in $500 \mu\text{s}$. To image the molecules, we reverse our coherent transfer process to bring the molecules back to a weakly bound state where we can detect the molecules with time-of-flight absorption imaging [26]. 93
- 5.3 Relative population of molecules in the lattice vibrational levels. We measure the relative population in each lattice vibrational level using a band-mapping technique. The results are shown for (A) a thermal distribution of molecules and (B) a non-thermal distribution created by parametric heating in \hat{z} . The two images use the same color scale for the optical depth (OD). The images are an average of 5 shots and 7 shots for (A) and (B), respectively, taken after 10 ms of free expansion. Below each image we show a trace along \hat{z} that corresponds to the OD averaged over the transverse direction. A fit (red line) to the trace, which takes into account both the size of the Brillouin zones and our imaging resolution, is used to extract the relative populations, n_v/n_{tot} , in each lattice level v . The horizontal axis corresponds to momentum in \hat{z} and is marked in units of the lattice momentum $\hbar k$, where k is the lattice wavevector. Figure reproduced from reference [74]. 95

- 5.4 Ramp procedure for measurement of chemical reaction rates. The $^{40}\text{K}^{87}\text{Rb}$ molecules are produced when the optical lattice is fully formed at $\approx 100 E_{rec}$, after 150 ms ramp time. The molecules can be excited to higher vibrational levels of the optical lattice via parametric heating. The parametric heating is done via a sinusoidal modulation of the lattice intensity for 300 μs . The electric field is turned on together with the parametric heating and it is turned off 5 ms before we switch off the dipolar trap and the optical lattice. The molecules are held in the combined dipolar trap and the optical lattice for a variable time. After the molecules are released from the trap, the image is taken after 10 ms time of flight. 97
- 5.5 Measurements of 2D loss rates and comparison with theory. (A) A fit (solid lines) to the measured loss curves, with (red circles) and without (black squares) 0.3 ms of parametric heating in \hat{z} , is used to extract the loss rate constants $\beta_{|3\rangle}$ and $\beta_{|2\rangle}$. (B) The extracted loss rate constants for collisions of molecules in the same lattice vibrational level (black squares) and from different lattice vibrational levels (red circles) are plotted for several dipole moments. Measured loss rate constants for molecules prepared in different internal states are shown as green triangles. For comparison with each of these three measurements, we include a quantum scattering calculation for $\nu_z = 23$ kHz, $T = 800$ nK (solid lines). The potentials corresponding to the dominant loss channel for the three cases are shown in matching colors in fig. 5.1 B. Figure reproduced from reference [74]. 101

5.6 Loss rates from 3D to 2D. The effective initial loss rate, β_{initial} , for polar molecules confined in a 2D geometry depends on the fractional population (n_0/n_{tot}) in the lowest harmonic oscillator level in \hat{z} , which for a gas in thermal equilibrium depends on the ratio $\frac{k_B T}{h\nu_z}$. The measured initial loss rates for a dipole moment of 0.174 D are displayed for two different thermal distributions (solid triangles), a non-thermal sample created by parametric heating (the top open triangle), and an extracted pure $\beta_{|3\rangle}$ when the entire population is residing in the lattice ground vibrational level (the bottom open triangle). The experimental results agree well with a simple model (black curve) described in this section. The top line indicates the value of $\beta_{|2\rangle}$ as measured in fig. 5.5 B. (Inset) The intralevel loss rate for identical fermionic $^{40}\text{K}^{87}\text{Rb}$ molecules in 2D (black circles) is compared with the loss rate in 3D (blue triangles). The 3D data for $T = 300$ nK are borrowed from reference [40]. The 2D data were taken at $T = 800$ nK and are converted to 3D rates by multiplication with $\sqrt{\pi}a_{ho}$, where a_{ho} is the harmonic oscillator length in \hat{z} . Figure reproduced from reference [74]. 102

Chapter 1

Introduction

1.1 From ultracold atoms to ultracold molecules

Over the last decades, the field of ultracold atoms has progressed at a tremendous pace. Initial experiments focused on the development of techniques to cool and trap atoms [1, 2, 3], including the decisive techniques of laser cooling and evaporative cooling. Based on these techniques very exciting and important milestones have been achieved: The preparation of Bose-Einstein condensates (BEC) [4, 5, 6, 7] and quantum degenerate Fermi gases in dilute atomic gases [8] opened new avenues in atomic physics. Fano-Feshbach resonances allowed control of atom-atom interactions [9]. This created novel opportunities such as the realization of strongly interacting systems, the study of BEC-BCS crossover physics [10, 11, 12], and the preparation of ultracold weakly bound Feshbach molecules [13, 14] from quantum degenerate gases of atoms.

Compared to atomic quantum systems, molecular quantum systems promise to open new research frontiers. However, the molecules' complex internal structure makes molecular systems very rich but also really challenging. Due to numerous vibrational and rotational quantum degrees of freedom, traditional cooling methods for atoms have not worked for molecules. Experimental efforts towards the creation of quantum gases of molecules have therefore followed two distinct paths. The first approach is to directly cool molecules to low translational temperatures. This can be achieved by Stark deceleration or buffer gas cooling [15, 16, 17]. Unfortunately, these techniques have so far been limited to low densities

(10^8 molecules/cm³) and relatively high temperatures in the milliKelvin range. These parameters correspond to a phase-space density of 10^{-13} and therefore many orders of magnitude away from quantum degeneracy. The second way is to cool and trap atoms first and then associate pairs of cold atoms to tightly bound molecules. A challenge here is the efficient conversion of free atoms to molecules while preserving density and temperature of the initial atomic ensemble. In 2005, Sage *et al.* [18], demonstrated the formation of vibrational ground state RbCs molecules formed via photoassociation from free atoms. Starting from a laser cooled atomic ensemble of 2×10^8 Rb and 3×10^8 Cs atoms at temperatures of $100 \mu\text{K}$ and phase space densities on the order of 10^{-14} , they obtained a conversion efficiency of few percent [18]. These experiments elucidated that to achieve better conversion efficiencies and higher phase space densities, the initial conditions of the atomic ensemble needs to be far closer to quantum degeneracy and the conversion process from free atoms to deeply bound molecules needs to be very efficient. In our lab, this was achieved by combining two techniques. The first is Feshbach molecule creation in ultracold quantum degenerate atomic gases, which allows the efficient conversion of atomic ensembles into weakly bound molecules prepared in a well-defined quantum state.

The next challenge was to transfer the weakly bound molecules into their absolute ground state. Our goal is to transfer to a single internal quantum state without heating the sample of molecules. Therefore, a fully coherent conversion process was needed. The conversion efficiency is also essential to preserve the initial high phase-space density. A technique known as STImulated Raman Adiabatic Passage (STIRAP) [19], involving an electronically excited intermediate state, can be envisioned for the transfer process between the initial and final vibration levels. Because of a nearly complete mismatch between the vibrational wave-functions of the weakly bound and the absolute ground-state molecules, it was largely believed to be impossible to find a suitable intermediate state that could provide sufficient transition strengths for both the upward and downward transitions. A proposal was made to use a train of two-color, phase-coherent pulses that would allow coherent accumulations

of a pump-dump process to implement a fully coherent molecular conversion process [20]. However, systematic and detailed single photon spectroscopy ensued [21], connecting the initial Feshbach state to specific electronically excited states with a CW laser referenced to an optical frequency comb. An intense theory-experiment collaboration led us to the realization that we could use a single stationary intermediate state instead of dynamic wave-packets, which a key point is to have an intermediate state that provides favorable Franck-Condon factors to both the initial weakly bound Feshbach state and the rovibrational ground state.

Coherent conversion of weakly bound molecules into a more deeply bound states has been demonstrated in several experiments [22]. In the work done by our group, Ospelkaus *et al.* [23], STIRAP is used to convert an ensemble of weakly bound ^{40}K - ^{87}Rb molecules, with binding energy of a few hundred kilohertz, into an ensemble of molecules in a vibrational state bound by more than 10 GHz¹. In 2008, we demonstrated that a single step of a coherent transfer can even be used to convert an ensemble of heteronuclear Feshbach molecules into an ensemble of rovibrational ground state polar molecules [26]. In these experiments, the energy difference between the initial and final states is about 125 THz and therefore it is necessary to establish a fixed phase relation between lasers of extremely different frequencies. This task was accomplished by referencing the two lasers to individual teeth of an optical frequency comb laser [27, 28, 29]. Using this technique, we demonstrated the creation of an ultracold high phase space density molecular gas prepared in its lowest internal quantum state. The resulting ground state molecular ensemble has a peak density of 10^{12} molecules/cm³, a temperature of 200 nK, and a phase-space density of 0.06, and is therefore prepared close to quantum degeneracy. Also, the molecules have an electric dipole momentum of 0.566 Debye. This opens exciting perspectives for the study of quantum gases with strong dipole-dipole interaction.

¹ Related work has been done for homonuclear molecules of Cs₂ and Rb₂ by Danzel *et al.* [24] and Lang *et al.* [25] respectively.

1.2 Dipolar interactions

Interactions between particles determines many of the observed phenomena in ultracold quantum degenerate atomic gases. Interactions profoundly modify the static and also the dynamic properties of the system [30]. Short-range and isotropic “contact” interactions dominate the properties of most quantum gases of ultracold atoms, whereas dipole-dipole interactions play only a negligible role. However, recent developments in the manipulation of cold atoms and molecules have opened the way for the study of dipole-dipole interparticle interactions in ultracold quantum gases.

Dipole-dipole interactions have interesting properties. First, the dipole-dipole interaction is spatially anisotropic, which means that the strength and sign of the interaction depends on the relative orientation of the dipoles. Second, the dipole-dipole interaction is long range, where the interaction decays with $1/r^3$, r being the interparticle distance. Third, the electric-dipole moment of molecules is tunable by means of an externally applied field.

Pioneering work on the study of magnetic dipole-dipole interactions in ultracold quantum gases was done in Tilman Pfau’s group [31, 32]. Pfau and coworkers managed to prepare a Bose-Einstein condensate (BEC) of ^{52}Cr atoms. Chromium has a large magnetic dipole moment of 6 Bohr magnetons - a factor of 6 larger than the magnetic-dipole moment of alkali atoms. By enhancing the dipole-dipole interaction by the choice of the atomic species and making use of Fano-Feshbach resonances in chromium to reduce the isotropic contact interaction, the group was able to achieve a regime where the anisotropic magnetic dipole-dipole interaction between ^{52}Cr in the BEC dominates over the short-range interaction. This allowed the study of the anisotropic character of the dipole-dipole interaction in collision and expansion dynamics of the atomic gas [32].

However, interactions between magnetic dipole moments of atoms are typically weaker than those between electric dipole moments of polar molecules. For example, the electric dipole moment of a typical polar molecule is on the order of 1 Debye, where 1 Debye

is $\approx 3.34 \cdot 10^{-30}$ C·m. The interaction energy between polar molecules is then typically a factor of 10000 times larger than the interaction energy between atoms interacting via magnetic dipole-dipole interactions with a typical dipole moment of 1 Bohr magneton (μ_B), $\frac{(1 \text{ Debye})^2 c^2}{(1 \mu_B)^2} \approx 10^4$.

Building on the preparation of an ultracold polar gas of fermionic ^{40}K - ^{87}Rb molecules in our group in 2008 [26], a variety of novel experimental possibilities have opened up based on the control and use of the dipole-dipole interaction between polar molecules. Theoretical proposals range from the study of quantum phase transitions [33] and quantum gas dynamics [34] to quantum simulations of condensed matter spin systems [35] and schemes for quantum information processing [36, 37, 38].

1.3 Overview of this thesis

The main work of this thesis is about the confinement of an ensemble of ground-state polar $^{40}\text{K}^{87}\text{Rb}$ molecules in a quasi-2D geometry to control chemical reactions at ultralow temperature. As a background for my thesis work, I review previous work in ultracold chemistry of $^{40}\text{K}^{87}\text{Rb}$ [39] and dipolar interactions in 3D [40]. These subjects are also discussed in Kang-Kuen Ni Ph.D. thesis [21] to which I contribute. The chemical reaction $\text{KRb} + \text{KRb} \rightarrow \text{K}_2 + \text{Rb}_2$ is exothermic and proceeds without a chemical reaction barrier at short-range. Starting from fermionic polar molecules close to quantum degeneracy, we study this atom-exchange chemical reaction in a regime where the motion of the molecules is strictly quantized. When the ensemble of $^{40}\text{K}^{87}\text{Rb}$ molecules is created in a single quantum state - that means the molecules are indistinguishable fermions - we observe chemical reactions to be strongly suppressed by a long-range p-wave barrier of $24 \mu\text{K}$ that effectively hinders the molecules from coming into short-range [39]. However, changing the quantum statistics of the molecular ensemble by preparing a 50:50 mixture of two spin states, we observe the collisional rate to be enhanced by a factor of 10-100. For these distinguishable molecules, collisions will proceed via the s-wave channel, which means that there is no repulsive colli-

sional barrier at long-range. The two molecules easily get within short-range where reaction loss proceeds with almost unity probability.

With this basic understanding of how chemical reactions occur in the quantum regime, we make use of the large tunable electric dipole moment to control the long-range potential between two colliding molecules and therefore the chemical reaction rate. Applying an external electric field induces a dipole moment in the molecule. The dipole-dipole interaction will then strongly determine the collisional processes occurring in the sample. Of particular importance is the anisotropic character of the dipole-dipole interaction. As shown in fig. 1.1, depending on whether the molecules are colliding in a “head-to-tail” (attractive) or “side-by-side” configuration (repulsive), chemical reactions will either be enhanced or suppressed. This is because the long range dipole-dipole interaction significantly modifies the height of the centrifugal barrier and thus changes the inelastic collision rate. The attractive nature of dipole-dipole interactions for polar molecules colliding “head-to-tail” lowers the barrier, whereas the repulsive dipole-dipole interaction for polar molecules colliding “side-by-side” raises the barrier. In a three-dimensional geometry, both “side-by-side” and “head-to-tail” collisions are allowed and will occur in the molecular sample. In our experiment, we show that for high electric fields, “head-to-tail” collisions dominate the loss process and we observe the exothermic bimolecular reactions to steeply rise with the 6th power in the dipole moment due to attractive “side-by-side” collisions [40, 41]. The larger the electric dipole-moment the faster will be the inelastic decay of the molecular ensemble.

These experiments show that due to the long inelastic collisional loss process in a 3D geometry, it will not be possible to prepare a sample of quantum degenerate polar molecules in such geometry. In particular, evaporative cooling of the molecules towards quantum degeneracy does not seem to be feasible. This challenge is addressed in this thesis, where we prevent “head-to-tail” dipole-dipole interactions. “Head-to-tail” dipole-dipole interactions can be suppressed if these molecules are confined in a 2D geometry [42, 43]. We use an one-dimensional optical lattice to confine the fermionic polar molecules in a quasi-two-

dimensional, pancake-like geometry. The dipoles are oriented along the tight axis of confinement. The combination of tight confinement (restricting the movement of the molecules along the axis of strong confinement to a single motional state) and Fermi statistics of the molecules strictly forbids molecules to approach in a “head-to-tail” configuration. Two polar molecules can approach each other only in a “side-by-side” collision, where the chemical reaction rate is suppressed by the repulsive dipole-dipole interaction. This quantum stereodynamics of the ultracold collisions can be exploited to suppress the chemical reaction rate by nearly two orders of magnitude. The suppression of chemical reactions for polar molecules in a quasi-two-dimensional trap opens the way for investigation of a dipolar molecular quantum gas.

1.4 Outline of the thesis

Chapter 2 gives a short overview of the experimental set up: the apparatus for the preparation of a two-species quantum degenerate ensemble of ^{40}K and ^{87}Rb , the creation of Feshbach molecules, and the laser system for the realization of the STIRAP transfer. Also, I will review how to realize a two-dimensional geometry by means of a one-dimensional optical lattice. In Chapter 3, I will discuss basic properties of the dipole-dipole interactions in 3D geometry, which sets the stage for $^{40}\text{K}^{87}\text{Rb}$ molecules in 2D geometry. In Chapter 4, I present the basic concepts of a 1D optical lattices, adiabatic loading of ^{40}K and ^{87}Rb atoms into the lattice, and formation of $^{40}\text{K}^{87}\text{Rb}$ molecules in the optical lattice. In Chapter 5, I discuss and present the suppression of inelastic collisions in the tight confinement regime. In Chapter 6, I summarize the thesis and discuss future work.

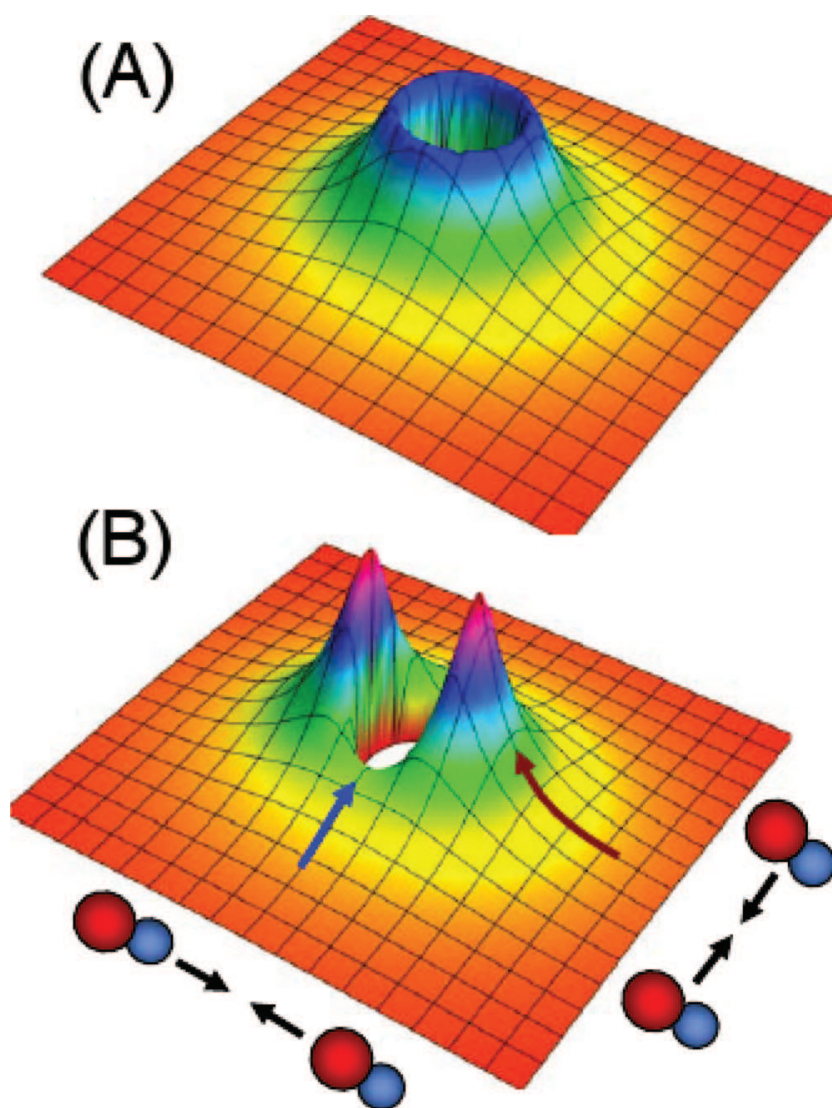


Figure 1.1: p-wave centrifugal barrier for dipolar collisions between fermionic polar molecules. (A), The effective intermolecular potential for fermionic molecules at zero electric field. At intermediate intermolecular separation, two colliding molecules are repelled by a large centrifugal barrier for p-wave collisions. (B), For a relatively small applied electric field, the spatially anisotropic dipolar interactions reduce the barrier for head-to-tail collisions and increase the barrier for side-by-side collisions. From [40].

Chapter 2

Experimental Apparatus

The basis for the experiments presented in this thesis is a reliable apparatus for the preparation of high-phase space density gases of ultracold polar ^{40}K - ^{87}Rb molecules in their rotational and vibrational ground state. In this chapter, I will give an overview of the experimental techniques and the experimental apparatus for the preparation of ground state polar molecules. As already mentioned in the introduction, our approach for the preparation of a high-density gas of ultracold ground state polar molecules is to cool and trap the constituent atoms ^{40}K and ^{87}Rb first and then implement a controlled chemical reaction at ultracold temperature. The latter is done via a two-step process, where in the first step, weakly bound molecules with a binding energy of $h \cdot 300$ kHz are formed in the vicinity of a Fano-Feshbach resonance [44]. These molecules are also called Feshbach molecules (FBM). Once these FBMs are formed, we transfer the molecules to the electronic, vibrational and rotational ground state via a single step of STImulated Raman Adiabatic Passage (STIRAP). In the following, we will call the resulting molecules ground state molecules (GSM). The heteronuclear $^{40}\text{K}^{87}\text{Rb}$ GSMs have an electric-dipole moment of 0.56 Debye [26], which allows the study of dipolar collisions controlled by external electric fields.

In the following, I will review our experimental path from the preparation of ultracold ^{40}K and ^{87}Rb atoms to the manipulation of ground state molecules. I will also discuss basic manipulation techniques for the ground-state molecules such as precise control over the dipole moment of the molecules by means of external electric fields and techniques for controlling

the confinement geometry of the molecules via dipole and optical lattice potentials.

2.1 From ultracold K and Rb atoms to ultracold ground-state molecules

2.1.1 Preparation of a near quantum-degenerate mixture of ^{40}K and ^{87}Rb

The starting point for the formation of a high-phase space density gas of ground state molecules is the preparation of a near quantum-degenerate mixture of two atomic species. In our case, we are working with the alkali atoms ^{40}K and ^{87}Rb . Both atoms are nowadays workhorses for atomic physics experiments in the quantum degenerate regime, and cooling and trapping techniques are therefore well established. In the following, I will briefly summarize the main experimental steps. For more details please refer to the Ph.D. thesis of Josh Zirbel [45].

Cooling and trapping of ^{40}K and ^{87}Rb starts with a two-species magneto-optical trap (MOT). Typical atom numbers in the MOTs are $2 - 4 \times 10^9$ for Rb and 10^7 for ^{40}K , respectively. After a short sub-Doppler cooling, optical pumping and compression state, these atoms are loaded into a quadrupole magnetic trap, which is then subsequently moved to a second part of the vacuum apparatus - the so-called science chamber. In the science chamber, the atoms are transferred into a Ioffe-Pritchard (IP) magnetic trap, where both ^{87}Rb and ^{40}K are cooled to temperatures on the order of $1 \mu\text{K}$. This is performed by evaporative cooling of Rb atoms via microwave radiation, which drives high energy ^{87}Rb atoms in the stretched $|F = 2, m_F = 2\rangle$ hyperfine state to an untrapped state $|1, 1\rangle$. Here F is the total atomic spin number and m_F is the projection. ^{40}K atoms prepared in the stretched $|9/2, 9/2\rangle$ state are sympathetically cooled in the bath of ^{87}Rb atoms. At the end of the evaporation in the IP trap, we typically achieve atom numbers of $6 - 7 \times 10^5$ for ^{40}K and $2 - 3 \times 10^6$ for ^{87}Rb , respectively, at temperature of $1 \mu\text{K}$.

Magnetic trapping is restricted to low-field seeking atomic states. However, for the preparation of Feshbach molecules, often high-field seeking states are needed to access a

Fano-Feshbach scattering resonance. Also, it is desirable to be able to choose the magnetic field freely, independent of any trapping potentials. In a next step, we therefore transfer the atomic mixture into an optical trap (OT). In our case, the OT is realized using a crossed beam configuration. In the experiment, we have chosen two elliptically shaped Gaussian beams with beam waists of $40 \mu\text{m}$ in the vertical and $200 \mu\text{m}$ in the horizontal direction, respectively. These two beams intersect at the center of the IP trap and have a wavelength of 1064 nm . The potential is pancake-shaped with an aspect ratio of 1:5.

The OT is loaded with ^{40}K and ^{87}Rb in the $|9/2, 9/2\rangle$ and $|2, 2\rangle$ states, respectively. We then transfer these atoms to their lowest hyperfine states, $|9/2, -9/2\rangle$ and $|1, 1\rangle$ performed via two adiabatic rapid passages, by sweeping RF (for ^{40}K) and microwave frequencies (for ^{87}Rb) at a magnetic field of 31.29 G . Choosing these two atomic quantum states has two distinct advantages. First of all, these quantum states are collisionally stable. Second, they allow access to a relatively broad Feshbach resonance between ^{40}K and ^{87}Rb at about 546 G [46, 47]. In preparation for Feshbach molecule creation, the magnetic field is ramped to 553.3 G and the atoms are evaporatively cooled closer to quantum degeneracy by decreasing the depth of the optical trapping potential. This procedure achieves temperatures of $200\text{--}300 \text{ nK}$, with ^{40}K and ^{87}Rb numbers of 2.5×10^5 and 3.5×10^5 - an ideal starting point for the preparation of $^{40}\text{K}^{87}\text{Rb}$ Feshbach molecules.

2.1.2 Feshbach molecule creation

For Feshbach molecule creation, we use a Fano-Feshbach resonance at a magnetic field of 546.7 G [46, 47]. This Feshbach resonance has a width of approximately 3 G and occurs via an avoided crossing between the open scattering channel K $|F = 9/2, m_F = -9/2\rangle + \text{Rb } |1, 1\rangle$ and the closed molecular scattering channel K $|7/2, -7/2\rangle + \text{Rb } |1, 0\rangle$. Starting from a mixture of approximately $2.5 \cdot 10^5$ ^{40}K atoms and $3.5 \cdot 10^5$ ^{87}Rb atoms at 200 nK prepared in the optical dipole trap at a magnetic field of 553 G , we ramp the magnetic field through the Feshbach resonance to a field of 545.90 G in 4 ms . This results in the formation

of approximately $6 \cdot 10^4$ Feshbach molecules with an expansion energy of $k_B \cdot 300\text{nK}$. At the magnetic field of 545.9 G, the Feshbach molecules are very weakly bound with a binding energy of $h \times 240$ kHz and a size of approximately 300 Bohr radii.

In the experiment, we observe conversion efficiencies from free atoms to Feshbach molecules of about 15 – 25%. The conversion efficiency is somewhat limited by a trade-off between high phase-space density of the initial atomic gases and good spatial overlap between the two species. To achieve good spatial overlap, the different quantum statistical character of ^{40}K (fermion) and ^{87}Rb (bosons) requires a temperature of the atomic gases just at the onset of quantum degeneracy - instead of starting deep in the quantum degenerate regime. Another limiting factor for the conversion efficiency is strong inelastic losses between ^{87}Rb and $^{40}\text{K}^{87}\text{Rb}$ in the vicinity of the Feshbach resonance.

2.1.3 Two-photon coherent transfer - STIRAP

To prepare a high phase-space density ensemble of ground-state polar molecules, the ensemble of Feshbach molecules has to be transferred into the rotational and vibrational ground-state. The transfer has to be done coherently to preserve density and temperature - and therefore phase-space density - of the initial Feshbach molecule gas.

We make use of a two-photon coherent transfer to transfer Feshbach molecules, prepared in the least bound vibrational state of the electronic ground-state molecular potential, to the rotational and vibrational ground state. The rotational and vibrational ground state is bound by approximately $h \cdot 125$ THz. A sketch of the scheme is shown in fig. 2.1. The Feshbach molecule state ($|i\rangle$) is coupled via a laser field to a vibrational state in an electronically excited molecular potential ($|e\rangle$). This electronically excited state is then coupled via a second laser field to the rotational and vibrational ground state ($|g\rangle$). Together, the two laser fields provide an effective coupling between the Feshbach state and the rotational and vibrational ground state. As the transfer scheme is fully coherent, the weakly bound Feshbach molecules are directly driven to the rovibrational ground state. This avoids any

heating of the molecules due to spontaneously emitted photons.

In the experiment, we make use of a very robust two-photon coherent transfer scheme - called STIRAP (STImulated Raman adiabatic passage). This specific scheme results in a robust transfer of the initial quantum state $|i\rangle$ to the final quantum state $|e\rangle$ without ever acquiring population in the lossy electronically excited state $|e\rangle$. The latter just provides a bridge between the initial and the final state [19]. Fig. 2.2 shows the details of the specific pulse sequence for the STIRAP transfer. The experiment starts with the entire molecular ensemble prepared in the initial state $|i\rangle$. Then, via the intensity ramp sequence shown in fig. 2.2, a coherent superposition is established between the intermediate state $|e\rangle$ and the final state $|g\rangle$ with laser 2 field. The intensity of laser 2 is adiabatically ramped down in $5 \mu s$, and at the same time, the intensity of laser is ramped up, performing transfer to the final state $|g\rangle$, without populating $|e\rangle$.

However, the actual implementation of the single-step of coherent two-photon transfer is challenging. First, it is very critical to achieve good coupling between the initial Feshbach state and the final ground molecular state. But these two wavefunctions are vastly different in size and the direct wavefunction overlap is very small. It is therefore necessary to identify a bridge in the electronically excited state to achieve the best possible coupling between the initial and the final state. In short, we need to choose an intermediate state with sufficient wave function overlap for both initial and final states, i.e. Franck-Condon factor (FCF). Second, it is critical to have phase coherence between the two lasers involved in the transfer scheme. This is challenging, because the two lasers bridge a frequency gap of 125 THz and have therefore vastly different wavelengths. In the following, we will discuss how we address and solve these experimental challenges.

2.1.3.1 The choice of the intermediate state

As pointed out in the previous paragraph, an appropriate choice of the electronically excited intermediate molecular state is critical for the preparation of a high-phase density gas

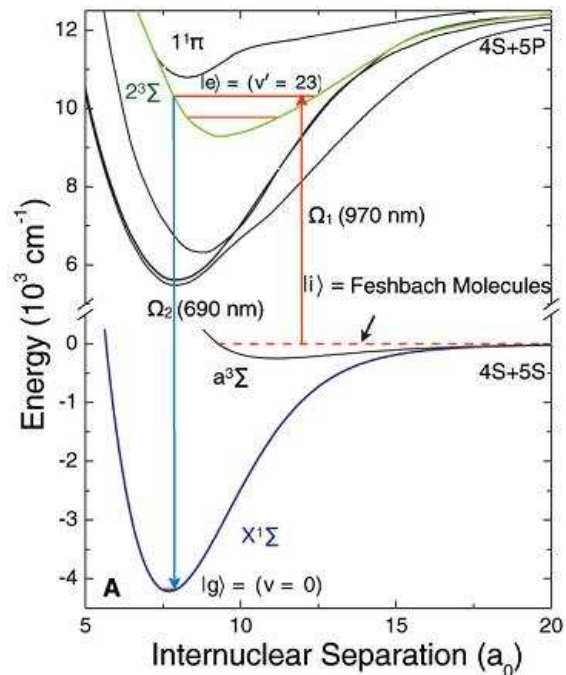


Figure 2.1: Potential curves for $^{40}\text{K}-^{87}\text{Rb}$ molecules and energy levels used for STIRAP transfer of Feshbach molecules to ground-state. The Feshbach molecules are formed in the initial state $|i\rangle = a^3\Sigma$. The intermediate state $|e\rangle = (v' = 23)$ is in the electronically excited potential of $2^3\Sigma$, and the final state $|g\rangle$ is in the ro-vibronic ground state $N = 0, v = 0$ of $X^1\Sigma$. The initial and the final states are about 125 THz apart from each other. This figure is reproduced from reference [26].

of ground state polar molecules. In our experiments, we make use of the scheme sketched in fig. 2.1 [26]. In this scheme, two cw lasers with wavelength of 970 nm and 690 nm couple the Feshbach state in the $^3\Sigma$ electronic ground-state molecular potential and the rovibrational ground-state in the $^1\Sigma$ electronic ground state molecular potential to a common intermediate state. The chosen intermediate state with good Franck-Condon factor for both FBM and GSM is the $v' = 23$ state of the $2^3\Sigma$ electronically excited potential. This state

has a small admixture of singlet spin character due to the proximity of the $^1\Pi$ molecular potential, which allows the transfer of triplet spin character Feshbach molecules to singlet spin character rovibrational ground state molecules. The upward transition strength from the Feshbach molecule state to this intermediate state was determined to be $0.005(2) ea_0$ [48]. The downward transition strength from the intermediate state to the rovibrational ground state has been determined to be $0.012(3) ea_0$ [48].

2.1.3.2 Phase and frequency stabilization of the coherent transfer lasers

In order to implement an efficient coherent transfer between two quantum states using STIRAP, it is essential to realize good phase coherence between the lasers involved in the transfer scheme. Loosely speaking, this means that the relative frequency jitter between the two lasers has to be as small as possible during the time window of the coherent transfer. In our specific application, achieving good phase coherence is a challenging task, since the two lasers involved in the transfer scheme are operating at vastly different wavelengths, corresponding to a frequency difference of 125 THz. A stable two-photon beat between these two lasers can be maintained by referencing each laser individually to a stable optical frequency comb.

The frequency comb

Frequency combs are powerful tools for several applications [49, 50, 51, 52, 53]. In our case, it is used as a stable “frequency ruler”, as shown in fig. 2.3, with 300 THz of spectral range (from 500 nm to 1100 nm). This frequency ruler is used to phase-lock two Raman lasers with a frequency difference of 125 THz [26].

The frequency comb used in our experiments is a solid state, ultracompact femtosecond titanium-sapphire (Ti:S) laser, pumped by a 532 nm Verdi 10W laser from Coherent. The pump power is 4.9 W (where the maximum power pumped to the Ti:S crystal should be no higher than 5.5 W). The laser has a ring cavity, with a 750 MHz repetition rate. The spectrum is centered at 800 nm and is 30 nm wide. The laser was modified to be actively

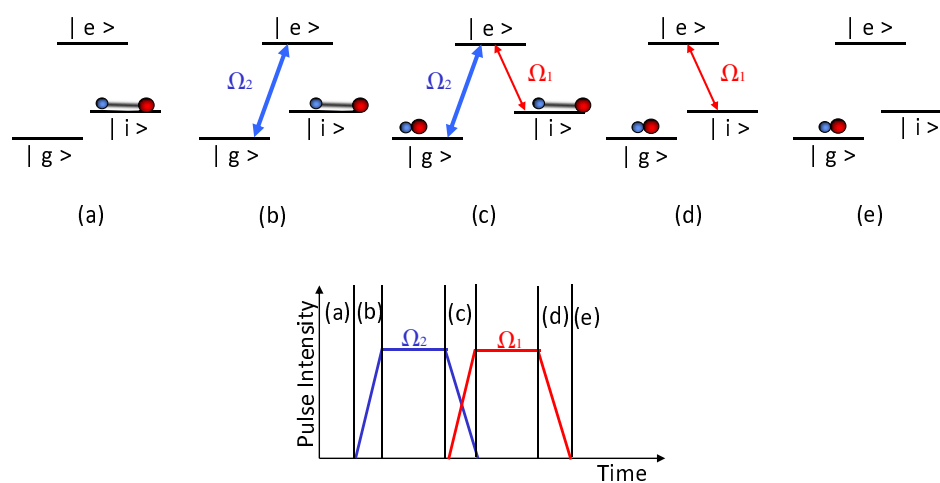


Figure 2.2: The schematic diagram of STIRAP pulse sequence. In (a), the molecules are in the initial state. In (b), the intensity of laser 2 is adiabatically ramped up, coupling states $|e\rangle$ and $|g\rangle$. In (c), the transfer of molecules in state $|i\rangle$ to state $|g\rangle$ happens by adiabatically ramping the intensities of laser 2 down and laser 1 up. In (d), laser 1 intensity is ramped down, and (e) is the end of the process, where about 90% of the Feshbach molecules are transferred to the ground state.

stabilized by controlling two degrees of freedom that determine the frequency of each comb tooth: the repetition rate, f_{rep} , and the carrier-envelope-offset frequency, f_{ceo} . The frequency for each comb tooth is given by the equation:

$$\nu_n = nf_{rep} \pm f_{ceo}, \quad (2.1)$$

where n is a integer number that represents the number of the comb tooth. $f_{rep} = 750$ MHz, and f_{ceo} is in the range of $0 \leq f_{ceo} \leq f_{rep}/2$. To be useful as a “frequency ruler”, both f_{rep} and f_{ceo} have to be stabilized. In the following, I will detail the stabilization of these two degrees of freedom.

Frequency comb stabilization

As already mentioned above, the frequency of the teeth of the optical frequency comb are determined by two degrees of freedom: f_{rep} , and f_{ceo} . These two degrees of freedom need to be controlled precisely. The stabilization of f_{rep} is realized by controlling the Ti:S laser cavity length via two piezoelectrics (PZTs) used as actuators. Using these knobs, f_{rep} is then stabilized by referencing a certain frequency tooth in the spectrum of the comb to a stable 1064 nm Nd:YAG. The Nd:YAG laser itself is locked to a stable cavity in John Hall’s lab and has a linewidth lower than 1 kHz. The locking electronics of f_{rep} are shown in fig. 2.5, where the error signal is fed back to the phase-lock loop electronics to the slow and fast PZTs.

The stabilization of f_{ceo} is a bit trickier. It requires a full octave spanning spectrum. To expand the Ti:Sa laser spectrum, a Photonic Crystal Fiber (PCF) [54], FEMTOWHITE 800 (polarization maintaining fiber and encapsulated from Crystal Fibre) is used [21]. The detection of f_{ceo} is done via a so called f-2f interferometer. This interferometer basically beats the low (1064 nm) and the high (532 nm) frequency portions of the spectrum to extract f_{ceo} [28]. The low frequency portion is doubled using a beta-barium borate (BBO) crystal and beat against the high frequency portion. The essentials of this scheme are schematically shown in fig. 2.6. Eq. 2.2 shows a simple relation that the f-2f interferometer uses to extract

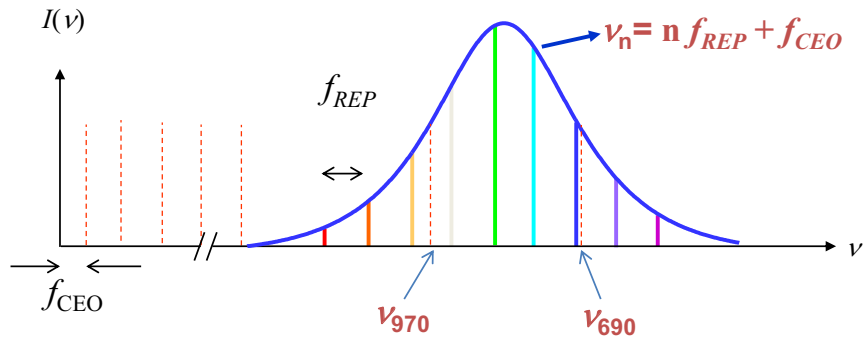


Figure 2.3: Schematic picture of the spectrum of the frequency comb. The two CW lasers at frequencies ν_{690} and ν_{970} are phase-locked to the comb.

f_{ceo} :

$$2\nu_n - \nu_{2n} = 2(nf_{rep} + f_{ceo}) - (2nf_{rep} + f_{ceo}) = f_{ceo}. \quad (2.2)$$

The error signal of f_{ceo} , is fed back via the phase-lock electronics to a Acousto-Optical Modulator (AOM), as shown in fig. 2.7. The AOM controls the Verdi-10W laser intensity by dumping a variable amount of pump power, between 0% to 5%, to the first diffraction order. The zeroth order is used for pumping the Ti:S laser.

Realizing the CW Raman lasers

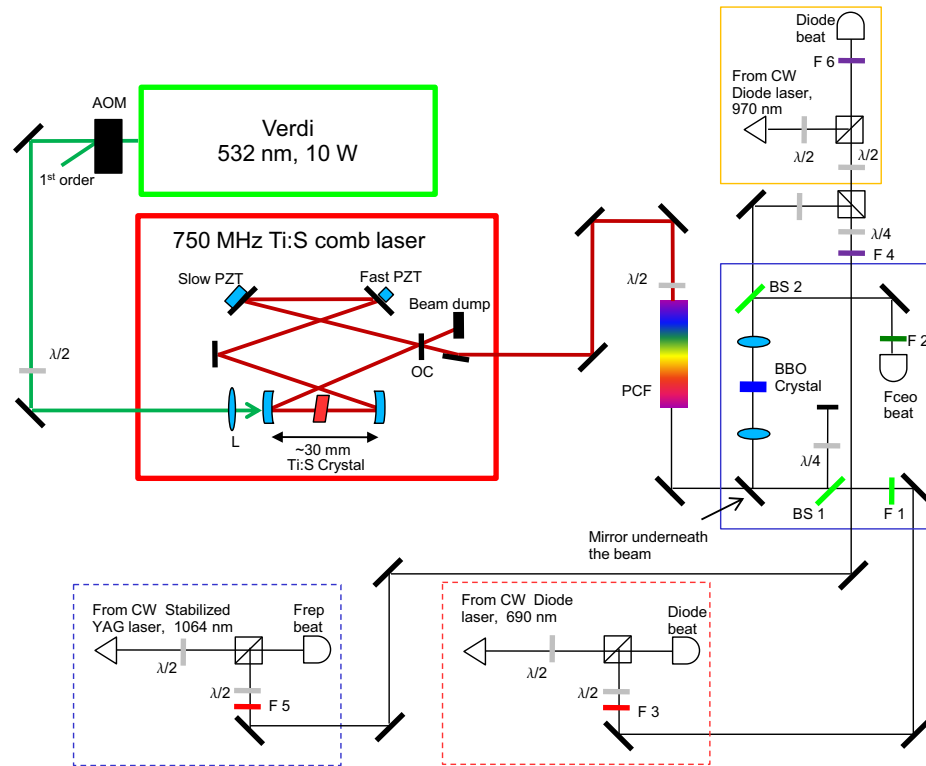


Figure 2.4: Frequency comb laser set up. This schematic diagram shows the Ti:S cavity (red box), the f-2f interferometer (blue box), the heterodyne beats for f_{rep} (dashed blue box), and the ν_{690} (dashed red box) and ν_{970} (orange box) phase-locks. The light from the Ti:S is then spectrally broadened in the photonic crystal fiber (PCF) to cover a range from 500 nm to 1100 nm. The input power to the PCF is 680 mW. f_{ceo} is stabilized via a f-2f interferometer. f_{rep} is phase-locked to a narrow YAG laser at 1064 nm. The several optical components are used to deliver the light with the right wavelength to their respective heterodyne beat set ups. F2, F3, F4, F5, and F6 are all band pass filters with FWHM 10 nm, at 532, 690, 1064, 1064, and 970 nm respectively. F4 also is used as a “mirror” to reflect 970 nm light. F1 is a high pass filter with $R(532 \text{ nm})/T(600 \text{ nm} - 850 \text{ nm})$. BS1 and BS2 are dichroic beam splitters where the reflection and transmission of the first are $R(950 \text{ nm} - 1100 \text{ nm})/T(500 \text{ nm} - 920 \text{ nm})$, and for the second are $R(532 \text{ nm})/T(920 \text{ nm} - 1100 \text{ nm})$.

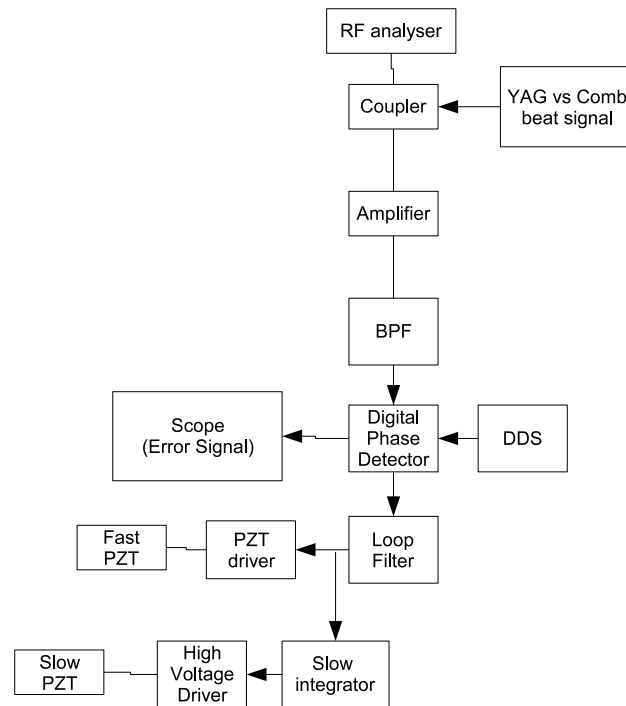


Figure 2.5: Locking electronics for f_{rep} . The beat signal of f_{rep} and the Nd:YAG laser is amplified, goes to a band pass filter (BPF), and then to a home built digital phase detector, where the frequency is divided and the signal is mixed to a direct digital synthesiser (DDS). The DDS is referenced to a 10 MHz commercial quartz clock (Wenzel Associates). The error signal goes to a home built loop filter, where the signal is divided and sent to a PZT driver to a fast PZT (≈ 50 kHz bandwidth), and to a slow integrator box (with time constant of ≈ 45 seconds), to a high voltage driver to a slow PZT. Using both fast and slow PZTs guarantee short and long term stability for f_{rep} .

In the experiment, we make use of grating feedback stabilized laser diodes to provide single frequency laser light at 970 nm and 690 nm. Details on the setup can be found in fig. 2.8 and fig. 2.9, respectively. For both lasers, we use commercially available AR-coated diode lasers from Eagleyard in an external cavity in Littman configuration. We have chosen this laser configuration as opposed to a Littrow configuration to allow for a large frequency tuning

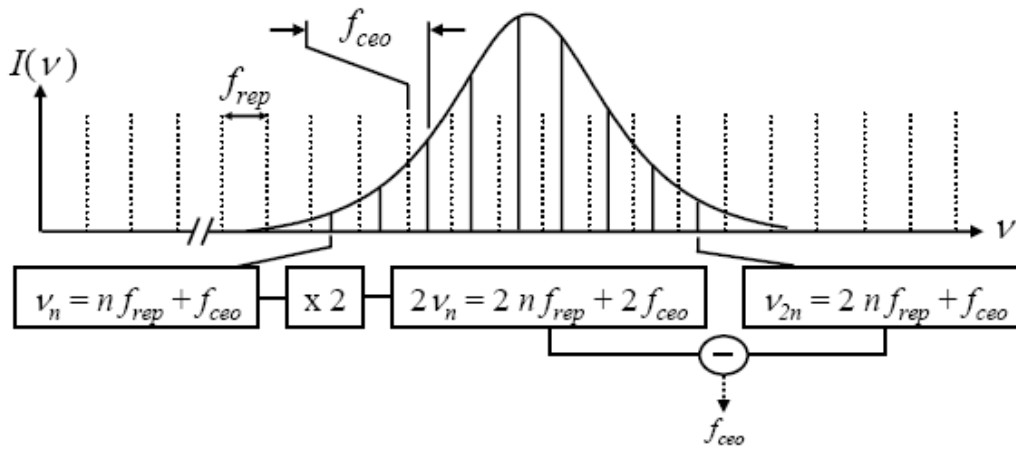


Figure 2.6: f_{ceo} detection via f-2f interferometer. From a broad spectrum, for f_{ceo} detection, the important wavelengths are 532 nm (high frequency portion) and 1064 nm (low frequency portion). The low frequency portion is doubled in a BBO crystal, and overlapped with the high frequency portion. The difference between the doubled low frequency portion and the high frequency portion is f_{ceo} . Figure reproduced from reference [55].

range without changing the beam pointing direction [56, 57]. However, at the same time, some output power is sacrificed as compared to the more common Littrow configuration. The output of the laser is split into three separate beams: one beam is used for monitoring the wavelength with a commercial wavemeter, one for the heterodyne beat with the comb for phase-locking, and the last one is sent to the molecules to perform STIRAP. To achieve large Rabi frequencies on the order of MHz for both the up transition and the down transition of STIRAP, we need to amplify the power of both lasers. The 970 nm light is amplified using a

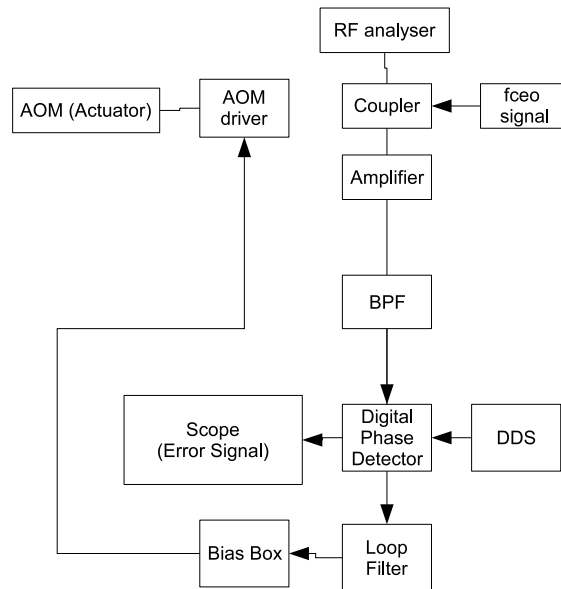


Figure 2.7: Locking electronics for f_{ceo} . The f_{ceo} beat signal is amplified, fed to a band pass filter (BPF), and then to a home built digital phase detector, where the frequency is divided and the signal is mixed to a direct digital synthesiser (DDS). The DDS is referenced to a 10 MHz commercial quartz clock (Wenzel Associates). The error signal goes to a home built loop filter, to a bias box, which puts an offset in the output voltage going to an AOM driver, feeding back the AOM that controls the intensity of the Verdi 10W laser.

tapered amplifier from Eagleyard. The 690 nm light is amplified by an injection locked diode laser. The amplified light is then sent to the experiment via a 10-meter long optical fiber. Typically, we deliver about 50 mW for the 970 nm laser, and 20 mW for the 690 nm laser to the experiment. the Raman laser beams are then focused down onto the atoms. In the experiment, we prepare a spot size of $40 \mu\text{m} \times 200 \mu\text{m}$. This configuration results in Rabi frequencies for the up and down transition of 0.3 MHz and 3.0 MHz, for dipole strengths of

$0.005(2) ea_0$ and $0.012(3) ea_0$ respectively [26].

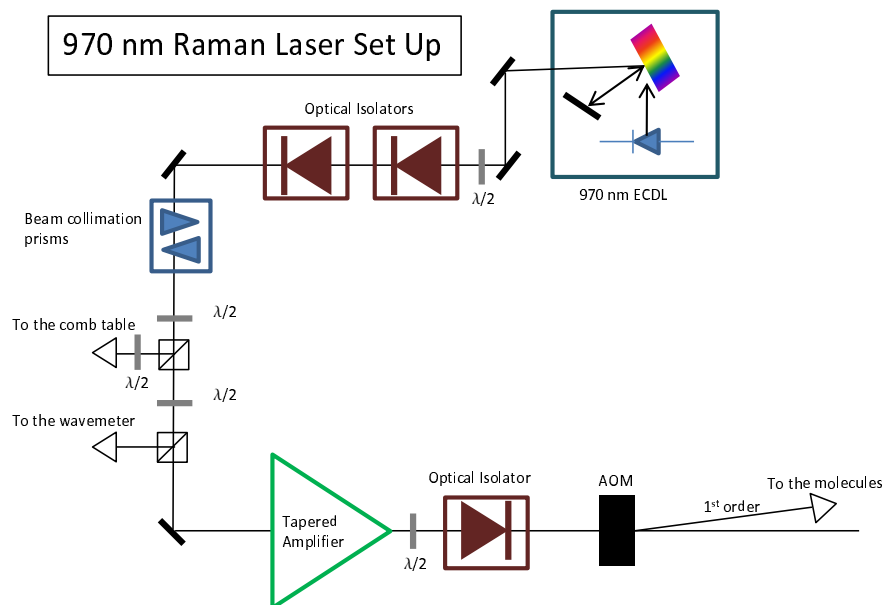


Figure 2.8: Raman laser system for 970 nm transition. This system has three outputs: one for a wavemeter, one for the frequency comb and one for the STIRAP transfer. The power of the laser is amplified by using a tapered amplifier.

2.1.4 Preparation of ground-state polar molecules

With these experimental prerequisites in place, we can transfer Feshbach molecules to the rovibrational ground state. Our experimental data are shown in fig. 2.10. In the

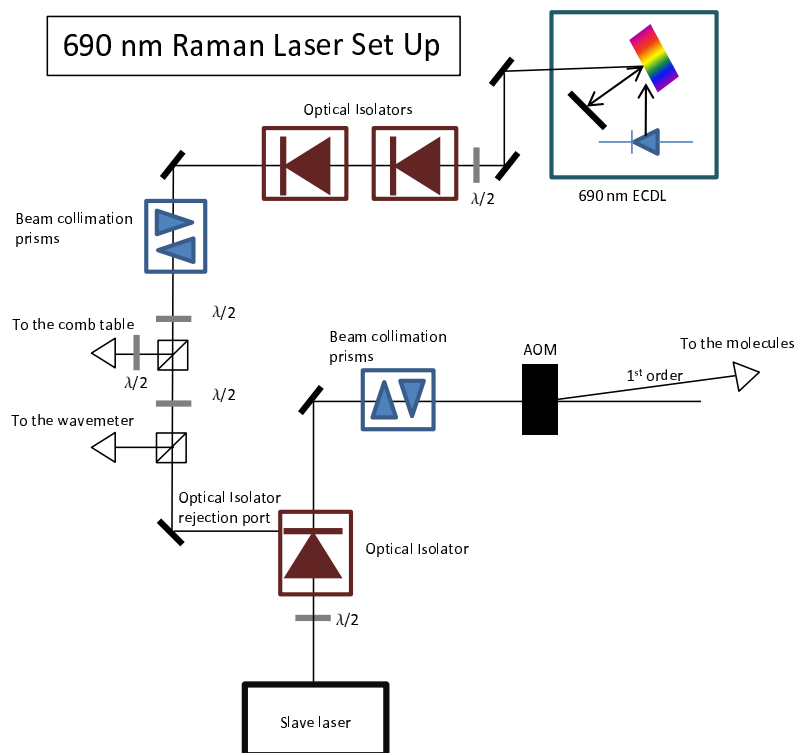


Figure 2.9: Raman laser system for 690 nm transition. This system has three outputs: one for a wavemeter, one for the frequency comb and one for the STIRAP transfer. The power of the laser is amplified by using another diode laser (slave laser) seeded with ≈ 1 mW of power from the master laser. The slave laser is locked via injection lock.

experiment, we start with about $6 \cdot 10^4$ Feshbach molecules. These molecules are then transferred to the rovibrational ground state. However, the ground-state molecules are dark to our imaging light. To image these molecules, we then reverse the STIRAP sequence and map the molecules back onto the Feshbach state, where we image them via direct absorption

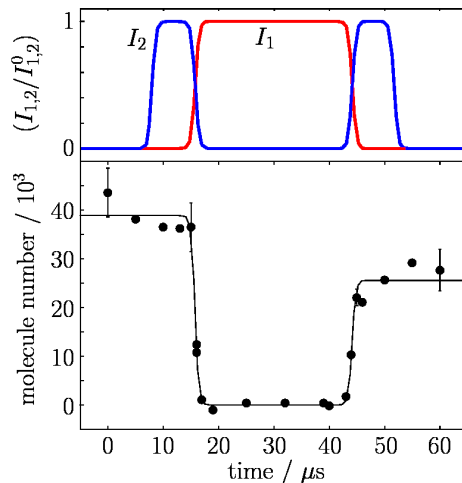


Figure 2.10: Timing diagram of the coherent two-photon transfer (STIRAP) from Feshbach molecules to the absolute rovibrational ground state $X^1\Sigma$ ($v = 0$). (a) STIRAP pulse sequence, where I_1 and I_2 are the intensities of laser 1 and laser 2. (b) Measured population in the initial Feshbach state during the STIRAP pulse sequence. Starting with $4 \cdot 10^4$ Feshbach molecules, the molecules are coherently transferred to the rovibrational ground state $X^1\Sigma$ ($v = 0$) by the first pulse sequence ($t = 15$ to $20\mu\text{s}$). The rovibrational ground state molecules are invisible to the detection light. Reversing the pulse sequence, $X^1\Sigma$ ($v = 0$) molecules are converted back to weakly bound Feshbach molecules ($t = 45$ to $t = 50\mu\text{s}$). This figure is reproduced from reference [48].

imaging. From fig. 2.10, we can extract an efficiency of the entire process of 80% round trip transfer. This suggests a a creation efficiency of ground state polar molecules of 90% [26]. We also demonstrated a scheme for direct absorption imaging of GSM [58].

Note that the transfer process from Feshbach molecules to ground-state polar molecules proceeds without introducing heat into the molecular cloud. This is illustrated in fig. 2.11 where we compare the expansion dynamics of Feshbach molecules to that of ground-state molecules. The expansion dynamics gives us precise information about the temperature of the molecular clouds. From the data, we extract for both ground-state molecules and Feshbach molecules a temperature of 400 nK. The two temperatures agree within the error

bars. This shows that the huge amount of binding energy of the ground state molecules is not released to the molecular ensemble during the transfer but instead carried away by the two light fields.

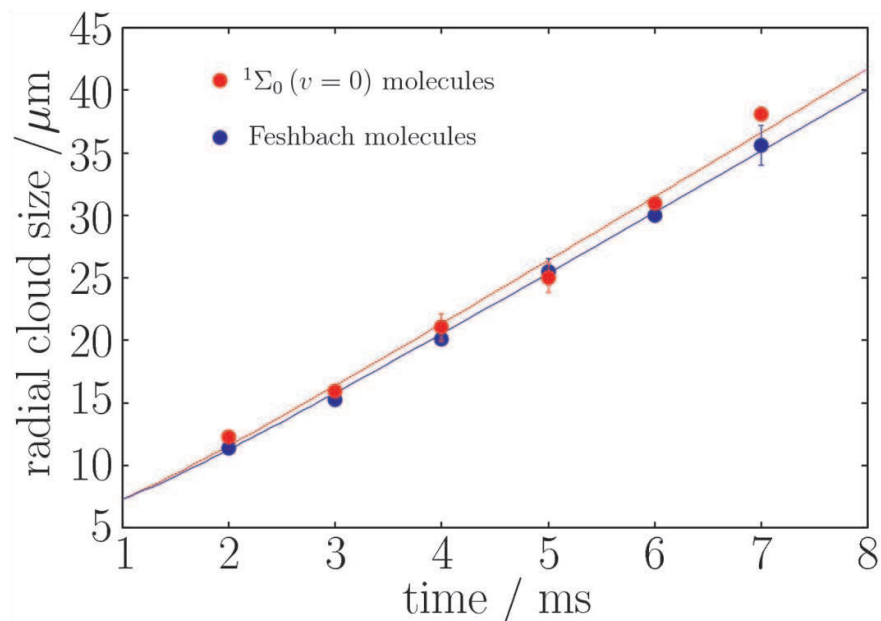


Figure 2.11: Comparison of the kinetic energy of the Feshbach molecules before STIRAP transfer (blue circles) and after a round-trip STIRAP process (red circles). The latter can be interpreted as an upper limit on the kinetic energy of the rovibrational ground state molecules. The temperature of both clouds is extracted by time of flight expansion analysis. We extract $T = 400(15)$ nK for the Feshbach molecules and $T = 430(20)$ nK for rovibrational ground-state molecules. The analysis shows that the transfer process does not cause any noticeable heating on the molecules. This figure is reproduced from reference [48].

2.2 Essential manipulation techniques for ground-state polar molecules

In the experiments presented in this thesis, two manipulation techniques of the ground state molecules are of large importance: accurate control over the dipole moment of the molecules and accurate control over the external confinement. These two experimental knobs allow us to demonstrate a large degree of control over the quantum dynamics of the collisional processes.

2.2.1 Electric dipole moment of the molecules

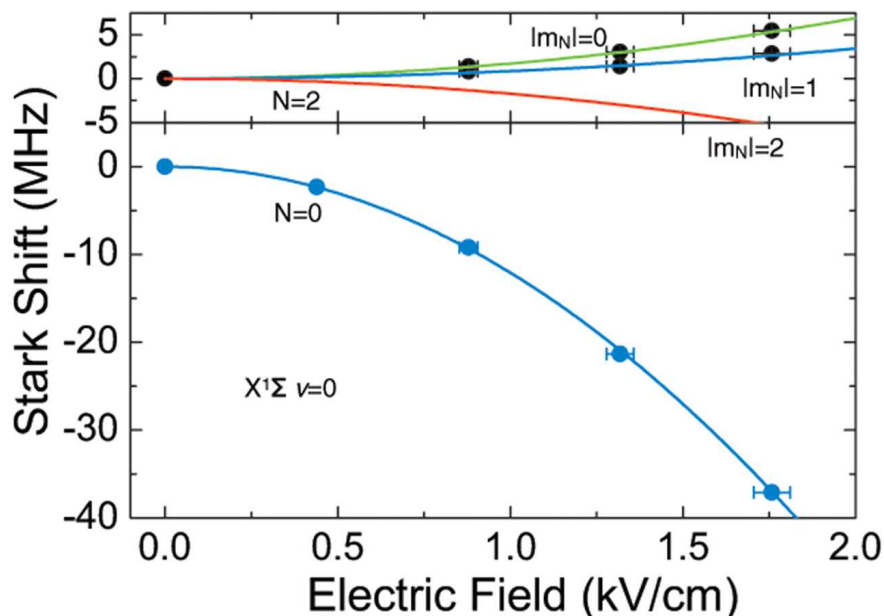


Figure 2.12: Stark spectroscopy of the singlet $v = 0$ molecules. The bottom panel shows the Stark shift of the rovibrational ground-state of the singlet potential ($v = 0, N = 0$ of $X^1\Sigma$), and the top panel shows the shift of the $v = 0, N = 2$ state. The systematic error in the applied electric field is 3% (horizontal error bars). The level difference between $N = 0$ and $N = 2$ is 6.6836(5) GHz, which yields a rotational constant B of 1.1139(1) GHz. Given the measured B , the fit of the Stark shift (line in lower panel) gives a permanent electric dipole moment of 0.566(17) D. The theory curves for $N = 2$ for different $|m_N\rangle$ projections (lines in upper panel) are calculated using the measured B and the dipole moment derived from the $N = 0$ fit. This figure is reproduced from reference [26].

One of the most interesting aspects of ultracold polar ^{40}K - ^{87}Rb molecules in the ground state is their electric dipole moment. Using two-photon Stark spectroscopy, we measured the dipole moment of the ground state $^{40}\text{K}^{87}\text{Rb}$ molecules to be 0.566 Debye [26], as shown in fig. 2.12. However, this dipole moment has to be induced by applying an external electric field. This electric field induces a dipole moment in the molecule by mixing different rotational states with opposite parity. Fig. 2.13 shows how the dipole moment of the $^{40}\text{K}^{87}\text{Rb}$ molecule develops as a function of the applied external electric field. The dipole moment of the molecules is zero at zero electric field, then initially increases linearly with

increasing electric field and finally saturates to a value of about 0.56 Debye.

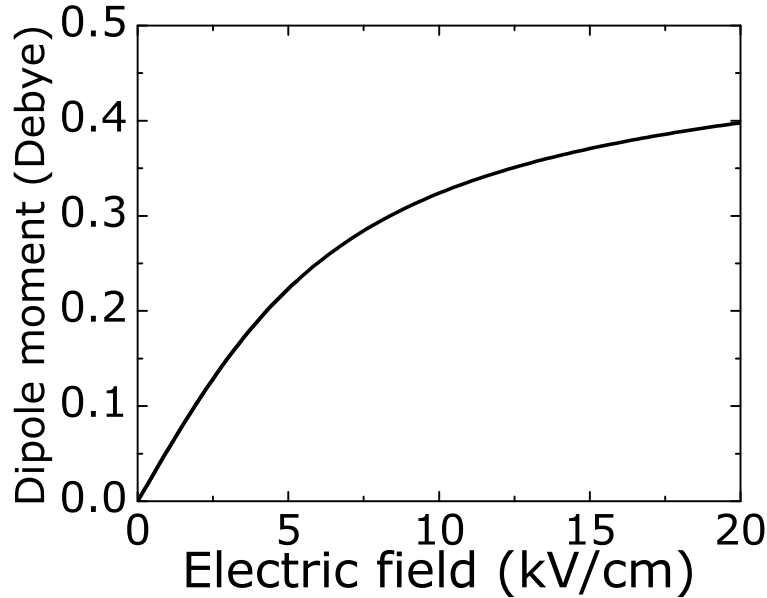


Figure 2.13: Calculated dipole moment versus applied DC electric field. In our experiment we can go to electric fields as high as 5.0 kV/cm.

In the experiment, we implement the external electric field by means of two electrodes located outside of the glass cell (“science chamber”) as shown in fig. 2.14. The plates are made from #CH-50IN-S209 transparent plates, coated with indium tin oxide from Delta Technologies. This material transmits 80-90% of the light in the wavelength range from 600 nm to 1100 nm and allows us to shine all necessary laser beams through the electrodes. The plates dimensions are 4 cm length, 2.37 cm width, and 0.09 cm thickness. The distance between the two plates is 1.35 cm. The thickness of the glass cell wall is 0.125 cm and it is made with a type of pirex glass with dielectric constant ≈ 4.8 . The electric field in the center of the glass cell is calculated from the geometry after taking into account the dielectric constants. For each 1 volt applied across the plates, the electric field in the center of the glass cell is:

$$\frac{1V}{1.35 \text{ cm}} \frac{1.35 \text{ cm}}{1.35 \text{ cm} - 2 \cdot 0.125 \text{ cm} + 2 \cdot (0.125/4.8) \text{ cm}} = 0.87 \frac{V}{\text{cm}}. \quad (2.3)$$

Since the electrode plates are outside of the vacuum chamber, dielectric breakdowns at relatively low applied voltages can happen. This limits the maximum voltage difference that can be applied across the plates to 5.6 kV and therefore limits the accessible dipole moment range to 0.20 Debye. However, within this range, we can tune the dipole moment of the molecules at will (from 0 to 0.20 Debye), therefore controlling collisional processes in the quantum regime (see chapter 5).

2.3 Tuning the geometry of the external confinement - 1D Optical Lattice

Due to the anisotropic nature of the dipole-dipole interactions, collisional properties of the molecules change drastically as a function of the geometry of the confinement (2D/3D) and the orientation of the dipole moment of the molecules with respect to the axis of tight confinement. This fact provides the motivation to implement versatile confinement geometries in our experiment. The crossed dipole trap mentioned above realizes a pancake geometry with an aspect ratio of 1:4. Although this geometry resembles somewhat a two-dimensional confinement geometry, this trap is providing a 3D geometry in terms of physics that can be studied in the confined system. This is the case since all energy scales of the confining geometry ($\hbar\omega_z$) are still much smaller than the kinetic energy in the system ($k_B T$).

However, we can realize a 2D geometry by making use of a 1D optical lattice. The 1D optical lattice will result in a stack of pancake-like trapping structures, where the energy scale of tight confinement ($\hbar\omega_z$) is much larger than the kinetic energy in the system. This restricts the molecules to a single quantum state in the tight confinement direction and therefore changes drastically the collisional properties of dipolar molecules as compared to a 3D system (see chapter 5).

In the experiment, we construct a one-dimensional lattice by establishing an optical

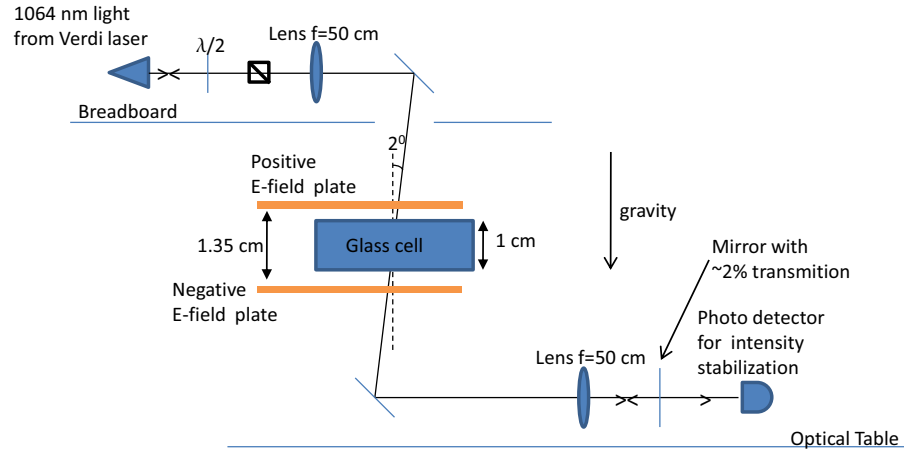


Figure 2.14: Schematic figure of the electric field plates and 1D optical lattice set up. The maximum output power of the fiber is 1.7 W. The polarization is set to be parallel to the optical table. The intensity of the optical lattice is stabilized via an AOM, which also shifts the frequency by +80 MHz.

standing wave. A schematic figure of the optical lattice's experimental set up is shown in fig. 2.14. The optical lattice potential will then divide the cloud in the optical dipole trap into a series of pancakes with tight confinement along the vertical \hat{z} axis (in the gravity direction). The optical lattice is realized by a single retroreflected laser beam. The beam waist of the optical lattice matches the beam waist of the dipole optical trap, in order to avoid heating as the intensity of the optical lattice is ramped up. The beam waist of the optical lattice is $250 \mu\text{m}$. For the optical lattice we use a single-mode Verdi-IR laser with

wavelength of 1064 nm, and power up to 25 W. We send light via a polarization-maintaining optical fiber with coupling efficiency of 40 to 50 %. At the output of the optical fiber, we get a maximum power of 1.7 W going to the molecules. The laser beam passes through the electric-field plates and the glass cell and then is reflected back, forming the optical lattice potential inside the cell. Due to losses in the electric field plates and the glass cell (the glass cell is not AR coated), the beam power after the retroreflection is 40 % lower than the initial power. The optical lattice beam is tilted from the vertical direction by an angle of 2 degrees to avoid back reflections inside of the glass cell impinging the molecular cloud and causing corrugations in the potential. The stabilization of the optical lattice depth is done by controlling the laser beam intensity. Approximately 2 % of the light leaks through the retroreflection mirror. This light is detected and sent to a servo that feeds back to an AOM that controls the amount of light going to the optical fiber.

Chapter 3

Dipolar $^{40}\text{K}^{87}\text{Rb}$ Molecules in 3D geometry

The preparation of a near quantum degenerate gas of all ground-state polar molecules opens tremendous opportunities for the study and control of molecular collisions in the limit of vanishing collisional energy. For chemically reactive molecules such as $^{40}\text{K}^{87}\text{Rb}$, it opens the unique opportunity to study chemical reaction dynamics in the completely unexplored limit where both the internal quantum states and external quantum states of motion are well defined. In this regime, collisions can be analyzed by simple quantum mechanical rules such as quantum statistics, single partial wave scattering, and quantum threshold laws.

In this chapter, I present the studies of ultracold chemical reactions in the quantum gas of polar molecules when molecules are confined in a 3D geometry as background material for my thesis work. These studies were already discussed in the thesis work of K.-K. Ni [21]. Starting with an optically trapped near-quantum-degenerate ($\frac{T}{T_F} \approx 1.4$) gas of polar $^{40}\text{K}^{87}\text{Rb}$ molecules prepared in their absolute ground state, we observe experimental evidence for exothermic atom-exchange chemical reactions. When these fermionic molecules are prepared in a single quantum state at a temperature of a few hundred nanokelvin, we observe p-wave dominated quantum threshold collisions arising from tunneling through an angular momentum barrier followed by a short-range chemical reaction with a probability near unity. When these molecules were prepared in two different internal states, the reaction rates were enhanced by a factor of 10 to 100 as a result of s-wave scattering, which does not have a centrifugal barrier. Inducing an electric dipole moment in the molecules results in

tuning of the chemical reaction rate over several orders of magnitudes. Finally, I present the thermodynamics of the molecular cloud under the influence of strong collisional loss revealing the anisotropic nature of the dipolar interaction. Throughout this chapter, I closely follow references [39, 40], which describe our work.

3.1 Bimolecular chemical reactions at ultracold temperature

Molecular quantum gases of $^{40}\text{K}^{87}\text{Rb}$ molecules offer the unprecedented opportunity to study chemical reactions in the limit of vanishing collisional energy. $^{40}\text{K}^{87}\text{Rb}$ molecules are not stable against atom exchange chemical reactions. Two $^{40}\text{K}^{87}\text{Rb}$ molecules collide and form with a high probability different chemical species, namely K_2 and Rb_2 [39]. This is because the chemical reactions $\text{KRb} + \text{KRb} \rightarrow \text{K}_2 + \text{Rb}_2$ is exothermic and moreover proceeds without chemical reaction barrier at short range [39].

However, chemical reactions have never been studied in the limit of vanishing collisional energy. Even basic questions such as how a chemical reaction proceeds at ultralow temperature and what quantum mechanical rules are responsible for molecular reactivity have never been addressed.

That chemical reactions could occur at ultralow temperatures seems at first glance counterintuitive. However, ultracold collisions, where particles scatter only in the partial wave with lowest angular momentum, are governed by quantum statistics and quantum threshold behaviors described by the Bethe-Wigner laws [59, 60]. In this regime, particles are represented by their de Broglie wavelength, which increases with reduced temperature. This wave nature of particles replaces our intuitive classical picture of collisions. The wave manifestation of tunneling through reaction or angular momentum barriers may play a dominant role in dynamics, and scattering resonances can have dramatic effects on reactions [61]. In addition, any barrierless chemical reactions will always take place when two reactants are sufficiently close together [62]. In this case, chemical reaction rates will be determined to a large extent by collisional properties at large intermolecular separations, and thus by

how the two molecules approach each other. Once their separation reaches a characteristic length scale ($10a_0$, where $a_0 = 0.53 \cdot 10^{-10}$ m), a chemical reaction happens with a near unity probability. Therefore, chemical reactions can be surprisingly efficient even at ultralow temperatures. Indeed, this model for barrierless reactions predicts loss rates that are universal in the sense that they do not depend on the details of the short-range interactions, but instead can be estimated using only knowledge of the long-range interactions [63].

3.2 The role of quantum statistics in determining the chemical reaction rate

For molecules prepared at a temperature of a few hundred nanokelvin, the collision rate is largely determined by the quantum statistics of the molecular ensemble. In the regime of vanishing collisional energy, collisions proceed in a single partial wave, because higher order angular momentum scattering channels are frozen out due to large centrifugal barriers. This means that depending on quantum statistics, molecules will collide in an s-wave $L = 0$ or p-wave $L = 1$ angular momentum scattering channel. In our experiments, we prepare fermionic $^{40}\text{K}^{87}\text{Rb}$ molecules. For spin-polarized molecules all prepared in the same internal quantum state, the p-wave collisional channel is then the lowest energy symmetry-allowed collision channel. The height of the centrifugal barrier for the p-wave ($L = 1$) KRb-KRb collision is $k_B \cdot 24 \mu\text{K}$. It is determined by the molecule-molecules long-range potential:

$$V_{LongRange}(R) = \frac{\hbar^2 L(L+1)}{2\mu R^2} - \frac{C_6}{R^6}, \quad (3.1)$$

where $L = 1$, μ is the reduced mass of the $^{40}\text{K}^{87}\text{Rb}$ and $C_6 = 16,130 E_h \cdot a_0^6$ (*a.u.*) [64], where $E_h = 4.36 \cdot 10^{-18}$ J. This barrier height is more than an order of magnitude larger than $k_B T$, where T is the translational temperature of the molecular gas. Thus, collisions of spin polarized molecules are expected to proceed predominantly via tunneling through the p-wave barrier. If two molecules make it through the barrier to short range, chemical reactions or hyperfine state-changing collisions can take place, leading to a loss of the entrance channel population. We note that even a single nuclear spin flip corresponds to a released quantity of

energy that is above the trap depth, and this would contribute to loss of trapped molecules. Preparing a 50:50 mixture of two different spin states allows molecules to collide in an s-wave collisional channel. Thus, there is no centrifugal energy barrier and chemical reactions will therefore proceed at a much higher rate.

3.3 The experimental system

To study chemical reactions of molecules in the quantum regime, we prepare a gaseous molecular sample at densities on the order of 10^{12} to 10^{13} cm^{-3} and temperatures of around 200 to 300 nK. The fermionic $^{40}\text{K}^{87}\text{Rb}$ molecules are prepared in a single hyperfine level of the rovibronic ground state ($N = 0, v = 0$ of $X^1\Sigma^+$) [26, 65] and in particular in the absolute lowest internal quantum state. At the ultralow temperature of a few hundred nK, even the tiny molecular hyperfine-state energy splitting of ≈ 760 kHz at $B = 545.9$ G [65], is much larger than the translational energy (300 nK corresponds to 6 kHz). The preparation of a well-defined hyperfine state is possible and is of essential importance for the experiments presented in this chapter. Complete control over the internal quantum state of the molecules (including hyperfine quantum degrees of freedom) permits direct observation of the role of quantum statistics in determining the molecular interactions and the chemical reaction rate.

Details on the precise and coherent manipulation of the molecular population in different hyperfine states of the rovibrational ground state $X^1\Sigma^+$ of $^{40}\text{K}^{87}\text{Rb}$ can be found in [65]. The $X^1\Sigma^+$ state has zero total electronic angular momentum, so that the hyperfine structure is basically the Zeeman effect of the nuclear spins $I^K = 4$ and $I^{Rb} = 3/2$ [63, 66] at the applied magnetic field. The hyperfine structure is depicted in fig. 3.1, where a total of 36 states are labeled by their projections of the nuclear spins of ^{87}Rb , m_I^{Rb} and ^{40}K , m_I^K onto the external magnetic field. For the study of chemical reactions, we produce molecules either in a single spin state $|m_I^K, m_I^{Rb}\rangle$, or in a mixture of two spin states. The hyperfine states used are an excited state $|-4, 1/2\rangle$ and the lowest-energy spin state $|-4, 3/2\rangle$. These are marked by the two ellipses in fig. 3.1. The $|-4, 1/2\rangle$ state is populated directly by the

two-photon Raman transfer starting from Feshbach molecules [26, 65]. The spin state of these molecules can be further manipulated coherently. For example, the entire $|-4, 1/2\rangle$ population can be transferred into the lowest hyperfine state, $|-4, 3/2\rangle$, using two successive microwave π -pulses through a rotationally excited $N = 1$ intermediate level as shown in fig. 3.2. Within the $N = 1$ manifold, coupling between rotation and the nuclear electric quadrupole moment of ^{87}Rb or ^{40}K atoms lead to mixing of different nuclear spin characters. Due to this mixing, it is possible to use the rotationally excited state as a bridge between different hyperfine states in the rotational ground state [65, 66]. We can probe molecules in any particular hyperfine state by reversing the entire transfer process and putting the population back into the initial weakly bound state. We use absorption imaging to measure the molecular gas number and temperature. Alternatively, we can also do direct image of ground state molecules by using a open optical transition [58].

3.4 Bimolecular chemical reactions at vanishing dipole moment

In first experiments, we studied the chemical reaction $\text{KRb} + \text{KRb} \rightarrow \text{K}_2 + \text{Rb}_2$ in the limit of vanishing electric field. In this limit, the $^{40}\text{K}^{87}\text{Rb}$ molecules do not have an electric dipole moment in the lab frame. The long-range interaction potential between two molecules is then entirely set by the competition between the attractive van-der-Waals interaction and the centrifugal barrier of the collisional process. Since the centrifugal barrier depends on L , the quantum statistics of the molecules has a important role for the long range interaction potential.

3.4.1 p-wave collisions

When the molecules are prepared in a single hyperfine state within the rotational and vibrational ground state, they are indistinguishable from each other. Since these molecules are fermions, the collision can only happen through odd angular momentum channels. In the limit of vanishing collisional energy, the dominating collisional channel is then the p-wave

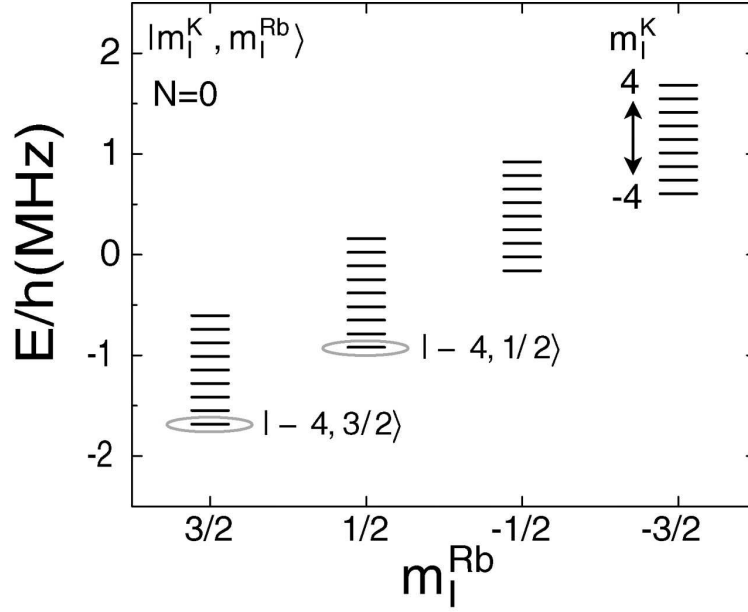


Figure 3.1: Hyperfine structure of rovibronic ground-state $^{40}\text{K}^{87}\text{Rb}$ molecules at a magnetic field of 545.9 G. Here we have 36 nuclear spin states by their spin projections, m_I^{Rb} and m_I^{K} . The energy spacing between hyperfine states is $h \cdot 130$ kHz for $|m_I^{\text{K}}| = 1$ and $h \cdot 760$ kHz for $|m_I^{\text{Rb}}| = 1$. By comparison, at a temperature of 300 nK, the molecules thermal energy is equivalent to $h \cdot 6$ kHz, which is more than an order of magnitude smaller than the spin flip energy. Molecules can be prepared in either a single state or in a mixture of The $|-4, 1/2\rangle$ and the lowest-energy state $|-4, 3/2\rangle$ (open ellipses). Figure reproduced from reference [39].

collisional channel and the competition between the van-der-Waals interaction and the finite centrifugal energy, which results in a p-wave collisional barrier given by eq. 3.1, with the angular momentum $L = 1$ for p-wave collisions. Here $C_6 = 16, 130$ *a.u.* [64], and the height of the centrifugal barrier is 24 μK .

As the collisional energy of molecules is in the sub μK regime, and much smaller than the height of the centrifugal barrier, chemical reactions can only proceed through quantum mechanical tunneling through the p-wave barrier. On the other hand, once molecules get within short range of each other, chemical reactions proceed with near-unity probability [41, 67]. We therefore expect the chemical reaction rate to be set by the tunneling rate of the molecules through the p-wave barrier.

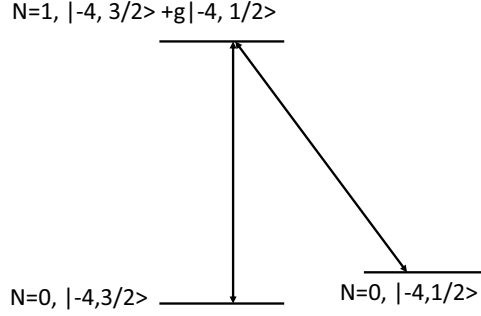


Figure 3.2: Transfer from the rovibrational ground state $|-4, 1/2\rangle$ to the absolute ground state $|-4, 3/2\rangle$ via coherent Rabi transfer. The intermediate state is in the rotational level $N = 1$ and it is a mixed state with $g \approx 5\%$.

Fig. 3.3A shows the decay of $^{40}\text{K}^{87}\text{Rb}$ molecules in a single quantum state $|-4, 1/2\rangle$ on a slow time scale of a few seconds. Analysis of the decay can be performed using a simple two-body collisional loss model where the density decay is given by:

$$\frac{dn(t)}{dt} = -\beta n^2. \quad (3.2)$$

Here, β is the two-body decay coefficient.

The quantum nature of the collisions can be observed in the temperature dependence of loss rates. The Bethe-Wigner threshold law predicts that the p-wave inelastic (reactive) collision rate is directly proportional to temperature ($\beta \propto T$) [59, 60]. To observe this behavior, we prepared spin-polarized molecules in the single hyperfine state $|-4, 1/2\rangle$ for several values of T ranging from 200 to 900 nK. The temperature of the molecular gas is controlled by changing the initial temperature of the ^{40}K and ^{87}Rb atoms during the evaporative cooling. The temperature is measured from the expansion energy of the molecular gas after releasing it from the optical trap. For each initial temperature, we look at the time-

dependent molecular loss and extract a two-body loss rate β (which is twice the collisional event rate) by fitting the decay of the molecular gas density n versus time t (fig. 3.3a) to

$$\frac{dn}{dt} = -\beta n^2 - \alpha n. \quad (3.3)$$

Here, the first term on the right takes into account the number loss and the measured β can be compared to theoretical predictions. The second term allows density change due to heating of the trapped gas during the measurement. Within a single measurement, we observe an increase in temperature that is at most 30%. In the analysis for each data set, we fit the measured temperature to a linear heating rate and obtain a constant slope c . In eq. 3.3, $\alpha = (3/2)[c/(T + ct)]$, where T is the initial temperature. At the lowest temperature that we can reach, 250 nK, the heating was (7 ± 1) nK s⁻¹ and $\beta = (3.3 \pm 0.7) \cdot 10^{-12}$ cm³ s⁻¹. The measured dependence of β versus T is summarized in fig. 3.3b (solid circles). Here, we fit the data to a power law $\beta(T) \propto T^L$ and find that $L = 1.1(\pm 0.2)$, which agrees with the predicted p-wave threshold law. This result demonstrates that indistinguishable ⁴⁰K⁸⁷Rb molecules at ultralow temperatures collide via tunneling through a p-wave barrier followed by an inelastic collision in the short range. A linear fit to the data ($L = 1$) yields a slope of the decay rate coefficient of $(1.2 \pm 0.3) \cdot 10^{-5}$ cm³ s⁻¹ K⁻¹.

We repeated this measurement for molecules in the lowest hyperfine state $|-4, 3/2\rangle$ (open triangles in fig. 3.3b). The data again show $\beta \propto T$ with a slope of $(1.1 \pm 0.3) \cdot 10^{-5}$ cm³ s⁻¹ K⁻¹, similar to that measured for molecules in the $|-4, 1/2\rangle$ state. However, in the case of $|-4, 3/2\rangle$ molecules, hyperfine state-changing collisions are no longer possible and the only possible loss channels are the chemical reactions discussed above. Thus, we find that the rate of chemical reactions is determined by the p-wave angular momentum barrier, and the chemical reaction barrier must be below the collision energy. This suggests that these reactions are barrierless and can thus occur freely at ultralow temperatures. Meanwhile, the fact that the same loss rate is observed for both $|-4, 1/2\rangle$ and $|-4, 3/2\rangle$ state molecules suggests that chemical reactions dominate the loss in these ground-state molecular collisions.

In order to understand the loss rates, two models are used: a quantum threshold model (QT) [41], and a model that uses the formalism of multichannel quantum defect theory (MQDT) [67]. In the QT model, the loss rate for collisions with energy equal to or above the height of the p-wave barrier is determined by the Langevin capture rate [68], which assumes that the probability for chemical reactions and/or hyperfine state-changing collisions is unity. For collision energies lower than the height of the p-wave barrier, in this model we assume that the loss follows the Bethe-Wigner threshold law [59, 60]. Using this assumption, we have an analytical expression for the p-wave loss rate coefficient of two indistinguishable molecules, which scales linearly with T [41]:

$$\beta = \frac{\pi}{4} \left(\frac{3^{17} \mu^3 C_6^3}{\hbar^{10}} \right) k_B T, \quad (3.4)$$

where μ is the reduced mass. Using a van der Waals dispersion coefficient of $C_6 = 16, 130 \text{ a.u.}$ for KRb-KRb with an uncertainty of $\pm 10\%$, the slope of the rate coefficient is predicted to be $1.5(\pm 0.1) \cdot 10^{-5} \text{ cm}^3 \text{ s}^{-1} \text{ K}^{-1}$, which agrees well with the experimental data.

In the MQDT model, the loss rate coefficient is calculated directly by the quantum tunneling rate through the p-wave barrier [69]. From this calculation $\beta = 0.8(\pm 0.1) \cdot 10^{-5} \text{ cm}^3 \text{ s}^{-1} \text{ K}^{-1}$, which agrees with the experiment within mutual uncertainties. This β can also be derived analytically from the properties of the long-range potential to give $\beta = (11.48\bar{a})^3 (k_B T/h)$, where $\bar{a} = 0.4778(2\mu C_6/\hbar^2)^{1/4} = 6.3 \text{ nm}$ is the characteristic length of the van der Waals potential [63]. This fully quantum calculation can be put in the same form as the QT model (eq. 3.4) and gives a β that is smaller by a factor of 0.528. With two models, the agreement with our molecule-molecule collisional loss measurements suggests that the chemical reaction rates are strongly influenced by the long-range interactions. This observation opens intriguing control possibilities because the long-range interaction can be controlled by selecting quantum states and tuning collision energies via applied electric and magnetic fields.

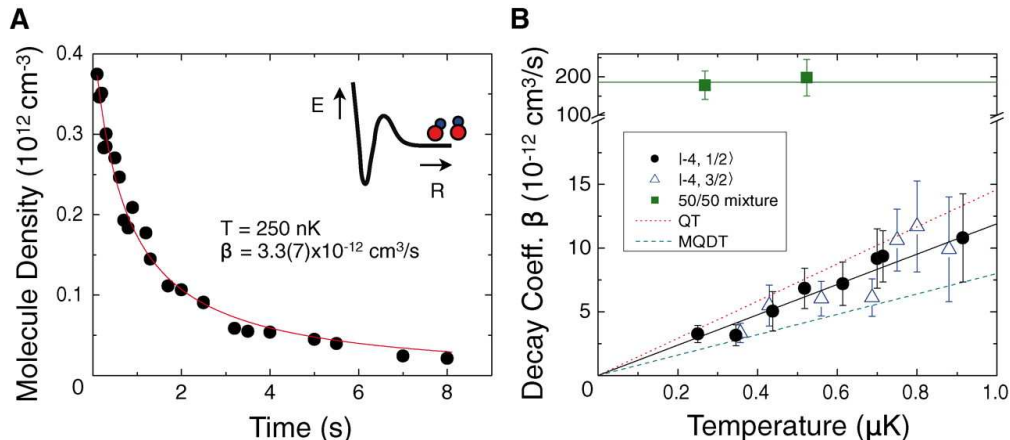


Figure 3.3: Inelastic collisions between spin-polarized (indistinguishable) or different spin-state (distinguishable) fermionic molecules in the rovibronic ground state of $^{40}\text{K}^{87}\text{Rb}$. (A) Data showing the time dependence of the molecule number density. Here the molecules are prepared in a single hyperfine state, $|-4, 1/2\rangle$, and the molecular density decays slowly with a rate coefficient of $3.3(\pm 0.7) \cdot 10^{12} \text{ cm}^3 \text{ s}^{-1}$ at $T = 250 \text{ nK}$. (B) Loss rate coefficient as function of the temperature. The loss rate increases linearly with temperature for spin-polarized molecules, which collide via p-wave [inset in (A)] at low temperature. Data were taken for molecules prepared in either $|-4, 1/2\rangle$ (solid circles) or the lowest-energy state $|-4, 3/2\rangle$ (open triangles). A linear fit (solid line) to the $|-4, 1/2\rangle$ data yields the temperature-dependent loss rate to be $1.2(\pm 0.3) \cdot 10^5 \text{ cm}^3 \text{ s}^{-1} \text{ K}^{-1}$. For the $|-4, 3/2\rangle$ case, where the collisional loss can only be due to chemically reactive scattering, the loss rate is similar. The dotted and dashed lines are the predictions from the QT and MQDT models, respectively. When the molecules are prepared in a mixture of the $|-4, 1/2\rangle$ and $|-4, 3/2\rangle$ states (solid squares), we observe a temperature-independent decay rate that is 10 to 100 times that for the spin-polarized case. Figure reproduced from reference [39].

3.4.2 s-wave collisions

Chemical reaction rates are very different if molecules are prepared in a mixture of different hyperfine states. In this case the molecules will interact via the s-wave collisional channel. The long range potential between two-colliding molecules is then dominated by the attractive van der Waals interaction, due to the vanishing centrifugal energy of the s-wave collisional channel. The collision can happen without any collisional barrier and are expected to proceed much faster at ultralow temperature than p-wave collisions studied in the previous section.

In order to confirm this expectation, we measure the inelastic collision rates for rovibronic ground-state molecules that were prepared in a roughly 50/50 incoherent mixture of the two hyperfine spin states $| -4, 3/2 \rangle$ and $| -4, 1/2 \rangle$. The time-dependent number density of trapped molecules was measured for both spin states. We measured the same loss rate for both states, consistent with loss due to collisions between distinguishable molecules in different spin states. The rate coefficient is determined to be $1.9 (\pm 0.4) \cdot 10^{-10} \text{ cm}^3\text{s}^{-1}$, independent of temperature (solid squares in fig. 3.3b). Comparing to the for p-wave collisions measurements between spin polarized molecules, the s-wave collision rate between molecules in different hyperfine states is higher by a factor of 10 to 100 for a similar temperature range.

3.5 Dipolar collisions with ultracold $^{40}\text{K}^{87}\text{Rb}$ in 3D geometry

Up to now, we have only studied collisions between $^{40}\text{K}^{87}\text{Rb}$ molecules in the limit of vanishing dipole moment. In the following, we will now study the unique properties of the dipole-dipole interaction as they manifest in collisions between two polar molecules. Precise control over the dipole moment of the molecules is given by an external electric field. The field mixes different rotational states with opposite parity within the vibrational ground state manifold and therefore induces an electric dipole moment in the rovibrational ground state.

3.5.1 Dipoles and chemical reactions

The dipolar interaction between molecules will strongly affect the chemical reaction rate between polar molecules. This is, because the dipolar interaction adds to the long-range potential between two colliding molecules, which is then given by:

$$V(R) = \frac{\hbar L(L+1)}{2\mu R^2} + \frac{C_6}{R^6} + \frac{(1-3\cos^2(\theta))C_3}{R^3}. \quad (3.5)$$

Here, C_3 is the relevant coefficient describing the dipole-dipole interaction between two molecules. Due to the anisotropic nature of the dipole-dipole interaction, this interaction can be either attractive or repulsive depending on the collisional process. This has im-

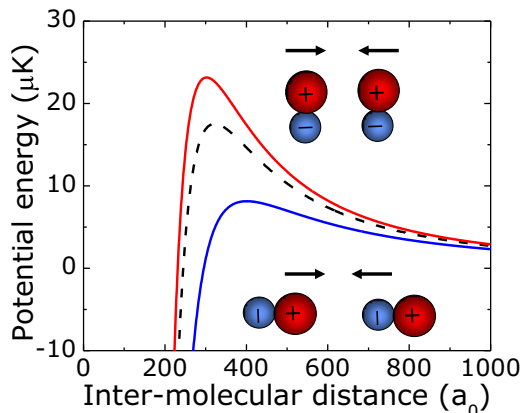


Figure 3.4: p-wave barrier for $^{40}\text{K}^{87}\text{Rb}$ dipolar collisions “head-to-tail” (solid curve in blue) and “side-by-side” (solid curve in red). The dashed line represents the p-wave in the absence of electric-field.

portant consequences on the chemical reaction rate for molecular ensembles, as illustrated in fig. 3.4. Preparing an ensemble of indistinguishable fermionic molecules, molecules will collide predominantly in the p-wave collisional channel which has a collisional barrier of $24\mu\text{K}$. In this case, the dipole-dipole interaction will either reduce or enhance the height of the collisional barrier, depending on whether collisions are attractive (“head-to-tail” collisions) or repulsive (“side-by-side collisions”). The dependence of the height of the collisional barrier as a function of the dipole moment of the molecules for both collisional channels is shown in fig. 3.6c. In the limit of small dipole moments relevant to our experiments, the collisional barrier will go down with the fourth power of the dipole moment for “head-to-tail” attractive collisions and will rise with the fourth power of the dipole moment for repulsive “side-by-side” collisions. We therefore expect the rate of attractive “head-to-tail”

collisions to increase dramatically with the dipole moment, whereas we expect at the same time repulsive “side-by-side” collisions to be strongly suppressed with increasing dipole moment. In the experiments performed in 3D, we expect the loss mechanism of the interactions “head-to-tail” to dominate our measurement.

3.5.2 The experiment

In order to study dipole-dipole interactions in collisions between molecules, we prepare a near quantum degenerate ensemble of $^{40}\text{K}^{87}\text{Rb}$ molecules in a single nuclear hyperfine state $|-4, 1/2\rangle$ within the rovibronic ground state. The gas is confined in a pancake-shaped optical dipolar trap. For this experiment, the harmonic trapping frequencies are $\omega_x = 2\pi \times 40$ Hz and $\omega_z = 2\pi \times 280$ Hz in the horizontal and vertical directions, respectively. The $^{40}\text{K}^{87}\text{Rb}$ molecules have a permanent electric dipole moment of 0.57 Debye. However, the effective molecular dipole moment in the laboratory frame is zero in the absence of an external electric field. When an external electric field is applied, the molecules begin to align with the field and have an induced dipole moment, d , that increases as shown in the inset of fig. 3.5b. In our set-up, the external electric field points up (in the \hat{z} direction), parallel to the tight axis of the optical dipole trap. Thus, the spatially anisotropic dipolar interactions will be predominantly repulsive for molecules colliding in the horizontal direction (“side-by-side”) and predominantly attractive for molecules approaching each other along the vertical direction (“head-to-tail”). However, the molecular confinement in this pancake shaped trap is 3D and hence neither of the collisional channel is suppressed.

3.5.3 Controlling chemical reactions by means of the dipole moment of the molecules

Using a single quantum state fermionic gas of rovibrational ground state polar molecules, we study the effect of electric dipolar interactions on collisions and find an unexpectedly large effect even for our relatively modest range of applied electric fields. We measure the molec-

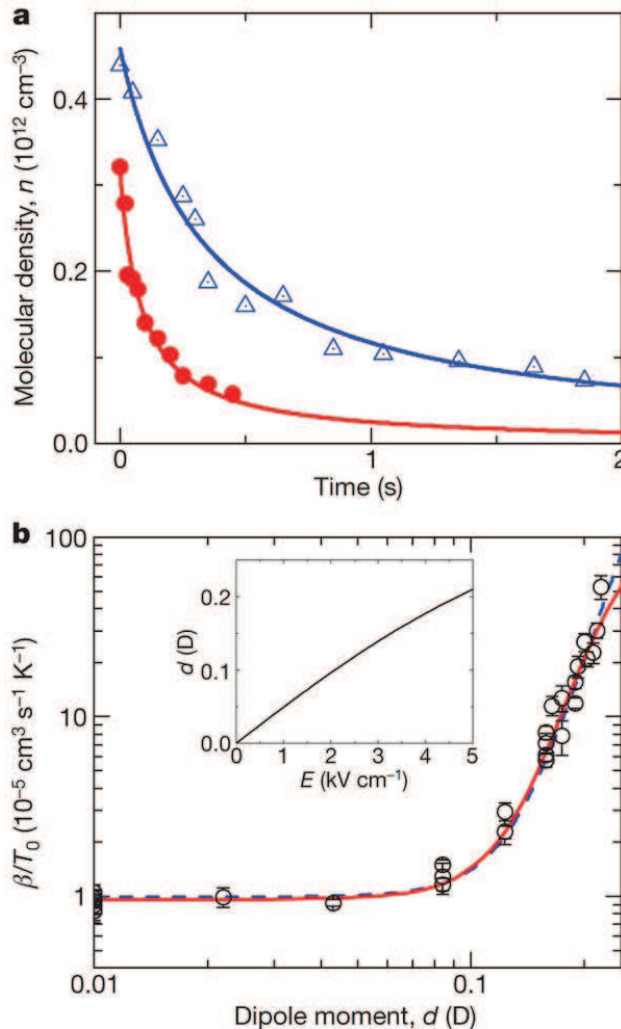


Figure 3.5: Two-body inelastic loss for fermionic polar molecules. (a), We extract the inelastic loss rate coefficient, β , from a fit (solid lines) to the measured time evolution of the trapped molecular gas density. Data are shown here for induced dipole moments of $d = 0.08$ D (open triangles) and $d = 0.19$ D (filled circles), and $T_0 = 300$ nK. (b), Data points show β/T_0 plotted as a function of d . The dashed line shows a fit to a simple model based on the quantum threshold behavior for tunneling through a dipolar-interaction-modified p-wave barrier. The solid line shows the result of a more complete quantum scattering calculation. Inset, the calculated dependence of d on the applied electric field, E . Figure reproduced from reference [40].

ular loss rate by monitoring the time evolution of the average number density of trapped molecules, n . We fit the data to the solution of eq. 3.3, as shown as solid lines in fig. 3.5a.

Fig. 3.5b shows the experimental data in a plot of β/T_0 as a function of d , where T_0 is

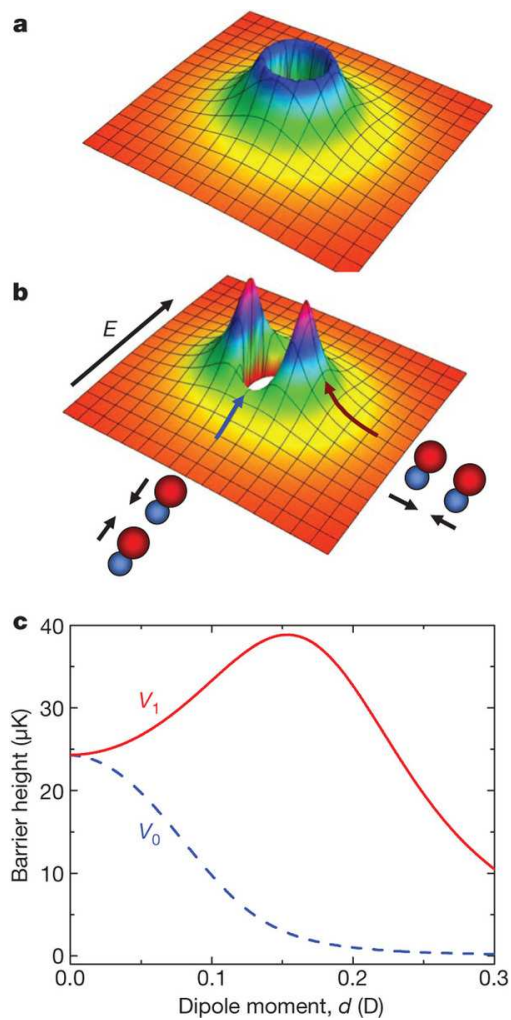


Figure 3.6: p-wave barrier for dipolar collisions between fermionic $^{40}\text{K}^{87}\text{Rb}$ molecules. (a), The effective intermolecular potential for fermionic molecules at zero electric field. At intermediate intermolecular separation, two colliding molecules are repelled by a centrifugal barrier for p-wave collisions. (b), For an applied electric field, the spatially anisotropic dipolar interactions reduce the barrier for “head-to-tail” collisions and increase the barrier for “side-by-side” collisions. (c), Height of the p-wave barrier as a function of dipole moment. Dipolar interactions lower the centrifugal barrier for $M = 0$ collisions (V_0) and raise the barrier for $M = \pm 1$ collisions (V_1). The lowering of the $M = \pm 1$ barrier at very large dipole moments is due to mixing with higher L partial waves ($L = 3, 5, 7, \dots$). Figure reproduced from reference [40].

the initial temperature of the molecules. We plot the ratio β/T_0 because the Wigner threshold law for p-wave scattering predicts that β is directly proportional to T , a temperature dependence verified at $d = 0$ in fig. 3.3. For the data in fig. 3.5, T_0 ranged from 250 nK

to 500 nK. In fig. 3.5b, we observe that dipolar interactions have a pronounced effect on the inelastic collision rate. At low electric field, where $d < 0.1\text{D}$, we observe no significant modification to the loss rate at zero electric field (which is plotted at $d = 0.01\text{D}$ due to the logarithmic scale). However, for higher electric fields, we observe a fast increasing loss rate, with an increase in β/T_0 of well over an order of magnitude by $d = 0.2\text{D}$. Fitting the data for $d > 0.1\text{D}$, we find that the inelastic loss rate coefficient has a power-law dependence on d : $\beta/T_0 \propto d^p$, where $p = 6.1 \pm 0.8$.

In order to understand the behavior for both low and large dipole moment regime, we assume that the collision rate follows the Wigner threshold law for p-wave inelastic collisions, that is, $\beta \propto T/V^{3/2}$. For dipole moments $d < 0.1$ Debye, the barrier height V is set by the competition between the attractive van-der-Waals interaction and the centrifugal energy of the collisional channel. Dipole-dipole interactions are negligible in this regime. However, when the dipole moment increases above 0.1 Debye, the barrier height for attractive “head-to-tail” collisions V_0 is significantly smaller than the barrier V_1 for repulsive “side-by-side” collisions and the loss will proceed predominantly through “head-to-tail” attractive collisions of the polar molecules. In this regime, V_0 scales as d^{-4} and the model predicts that β/T_0 will increase with a characteristic dependence on the sixth power of d for $d > 0.1\text{D}$ [41]. This prediction is in good agreement with our measured dependence of the loss rate on d for $d > 0.1\text{D}$ (fig. 3.5b).

To give a quantitative description of the inelastic collisional rate over our full range of experimentally accessible dipole moments, we include both contributions from both attractive “head-to-tail” collisions ($M = 0$) and repulsive “side-by-side” collisions ($M = 1$), where M is the quantum number that describes the projection of the relative orbital angular momentum (quantum number L) onto the electric field direction. We write the inelastic loss rate coefficient as $\beta = K_0 T_z + 2K_1 T_x$, the sum of two terms corresponding respectively to $M = 0$ and $M = \pm 1$ scattering, and we assume that $T_z = T_x = T$. The dipole moment

dependent coefficients, K_0 and K_1 , are obtained using

$$K = \gamma \frac{3\pi\hbar^2}{\sqrt{2\mu^3 V^{3/2}}} k_B, \quad (3.6)$$

where K and V respectively equal K_0 and V_0 or K_1 and V_1 , and μ is the reduced mass of the colliding molecules. The barrier heights, V_0 and V_1 , are taken to be the respective maximum energies of the long-range adiabatic potential, $V(R)$, calculated in a basis set of partial waves, $|L, M\rangle$, for $M = 0$ and $M = \pm 1$. The potential $V(R)$

$$V(R) = \frac{(1 - 3\cos^2(\theta))C_3}{R^3} - \frac{bC_6}{R^6} + \frac{\hbar^2 L(L+1)}{2\mu R^2}, \quad (3.7)$$

where the first term represents the dipolar interaction, the second term represents an attractive isotropic van der Waals interaction, and the last term is a repulsive centrifugal potential. b and γ are the only fit parameters, when fitting this model to the measurements of β/T_0 versus d .

We fit the prediction of the QT model to the experimental data using two fit parameters: a scaling factor, γ , that can be interpreted as the loss probability when the collision energy equals the height of the barrier; and another scaling factor, b , that multiplies the coefficient of the van der Waals interaction, C_6 . The final theoretical prediction (fig. 3.5b, dashed line) agrees well with the data (fig. 3.5b, open circles); from the fit we extract $\gamma = 0.35 \pm 0.08$ and $b = 2.4 \pm 0.9$. For comparison with the QT model, fig. 3.5b also shows (solid line) the result of a more complete quantum scattering calculation. This calculation uses a strong absorptive potential at short range but captures the long-range physics and uses C_6 as the single fit parameter. This fit also agrees well with the experimental data, and gives $C_6 = 21,000 \pm 7,000 \text{ a.u.}$, which is consistent with the calculated value of $C_6 = 16,130 \text{ a.u.}$ [64].

3.5.4 Thermodynamics of dipolar collisions

The increased inelastic loss rates with increasing dipole moment d is accompanied by a dramatic rise of the heating rate for the polar-molecule gas. In fig. 3.7, we plot the fractional

heating rate, \dot{T}/T_0 , normalized by the initial density n and temperature T_0 , as a function of d . The heating rate $\dot{T} = c$ is extracted using a linear fit to the temperature of the molecular cloud measured as a function of time over a period sufficiently long to allow T to increase by approximately 20-30%. We have developed a simple thermodynamic model for heating that is directly caused by the inelastic loss. We consider the energy lost from the gas when molecules are removed in inelastic collisions, and assume that the gas stays in thermal equilibrium. In this model, the heating arises solely from density-dependent loss of particles from the trap, where the particles removed by inelastic collisions have, on average, lower energies than typical particles in the gas. This is also called “anti-evaporation” mechanism [70]. One way to understand this anti-evaporation is to note that inelastic collisions preferentially remove particles from the center of the trap, where the number density is the highest and the particles have the lowest potential energy from the trap. In our model, we also include a competing, “cooling”, effect that comes from the fact that the p-wave inelastic collision rate increases linearly with the collision energy. Including these two competing effects, our model based on the analysis shows that the initial heating rate of the molecules is proportional to the inelastic loss rate β by a factor of $1/12$. When we plot $\frac{\beta}{T_0}/12$ in fig. 3.7 (solid line) we can see that our model explains the heating well, where we obtain $T_0^2 n = (\beta/T_0)/12$.

3.5.5 Anisotropy of heating

The anisotropy of the dipole-dipole interaction is shown directly in the energy distribution of molecules in the trap. The average energy per particle, which we measure from the expansion of the gas following a sudden release from the trap, can be different in the vertical and horizontal directions. In the following, we present measurements of the time evolution of the expansion energy in these two directions for different values of d . To probe the spatial anisotropy of dipolar collisions, we start by adding energy along one direction of the cylindrically symmetric trap using parametric heating. We modulate the power of both optical trapping beams at twice the relevant harmonic trapping frequency, for 50 ms (\hat{z}

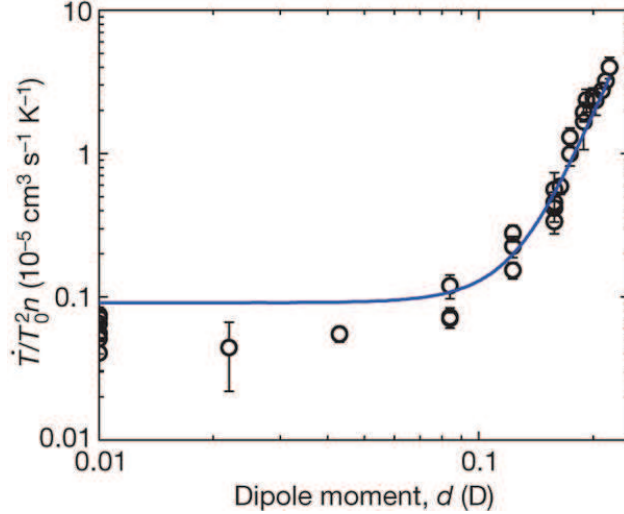


Figure 3.7: Normalized fractional heating rate, $\dot{T}/T_0^2 n$, versus the dipole moment. The heating rate is extracted from a linear fit to the initial temperature increase and is then normalized by the initial density and temperature of the ensemble. The solid line is the expected heating rate, given by $\dot{T}/T_0^2 n = (\beta/T_0)/12$. Typical experimental initial conditions are $n = 0.3 \cdot 10^{12} \text{ cm}^{-3}$ and $T_0 = 0.5 \mu\text{K}$, and the absolute heating rate ranges from $0.5 \mu\text{K s}^{-1}$ at zero electric field to $2 \mu\text{K s}^{-1}$ at our highest electric fields. Figure reproduced from reference [40].

direction) or 100 ms (\hat{x} and \hat{y} directions). Then we wait 100 ms before increase the electric field (in less than 1 ms) to the desired final value and measuring the time dependence of the vertical and horizontal “temperatures” of the cloud, respectively denoted T_z and T_x . These two quantities are associated with the measured expansion energies in the two directions. Note that this type of measurement is used in experiments on ultracold atoms, to measure the elastic collision cross-section [71].

In fig. 3.8 we show the experimental data from these rethermalization experiments for three different values of dipole moment, d , and under two initial conditions: $T_z > T_x$ (fig. 3.8a-c) and $T_z < T_x$ (fig. 3.8d-f). For $d = 0\text{D}$ (fig. 3.8a, d), T_z and T_x reaches equilibrium slowly, in approximately 4 s. Because $d = 0\text{D}$, there are no dipolar interactions and the data agrees with our expectation of very slow equilibration for spin-polarized fermions. This is the longest rethermalization time we observed in our trap, and therefore the data are

consistent with there being no elastic collisions and only technical imperfections such as a small cross-dimensional coupling in the trapping potential.

In an applied electric field case, the elastic collision cross-section due to long-range dipolar interactions is predicted to increase in proportion to d^4 [72]. For the case in which initially $T_z > T_x$ (fig. 3.8b, c), the data show that T_z and T_x approach each other in what seems on casual inspection to be cross-dimensional rethermalization. The time scale for this apparent rethermalization even decreases steeply as d increases, as might be expected. However, we note that in fig. 3.8c the temperatures cross each other, which is inconsistent with rethermalization driven by elastic collisions. Even more striking is the fact that the thermodynamic behavior of the gas is completely different when the gas initially has $T_z < T_x$. In this case, T_z and T_x do not equilibrate during the measurement time (fig. 3.8e, f).

To explain these observations we take into account the spatially anisotropic nature of inelastic dipole-dipole collisions and the fact that the molecular gas undergoes number loss. We have observed (fig. 3.7) that loss due to inelastic collisions heats the gas. This heating rate can be quantitatively understood by considering the effect of molecule loss on the average energy per particle. We can modify the model of heating and inelastic collisions described above to allow the average energy per particle, or “temperature”, to be different in the two trap directions. The model then predicts that the dominant “head-to-tail” collisions ($M = 0$) will lead to heating in the \hat{x} and \hat{y} directions but cooling in the \hat{z} direction. “Side-by-side” collisions ($M = \pm 1$), however, should contribute to heating in the \hat{z} direction but produce no temperature change in the \hat{x} and \hat{y} directions. Comparing this model with the experimental data, we fix the d -dependent β using the fit to our data in fig. 3.5 (solid line). This fixes both the time evolution of the molecule number as well as the heating rates in the two trap directions. Then we include a possible elastic collision effects in the model by adding a term that would exponentially drive the energy difference between the two directions to zero. In fig. 3.8 we also present a comparison between the results of the model (solid lines) and our experimental data. Although the model uses few free parameters (only the elastic

collision cross-section, σ_{el} , in addition to the initial values of n, T_x and T_z), it provides good agreement with the experimental data.

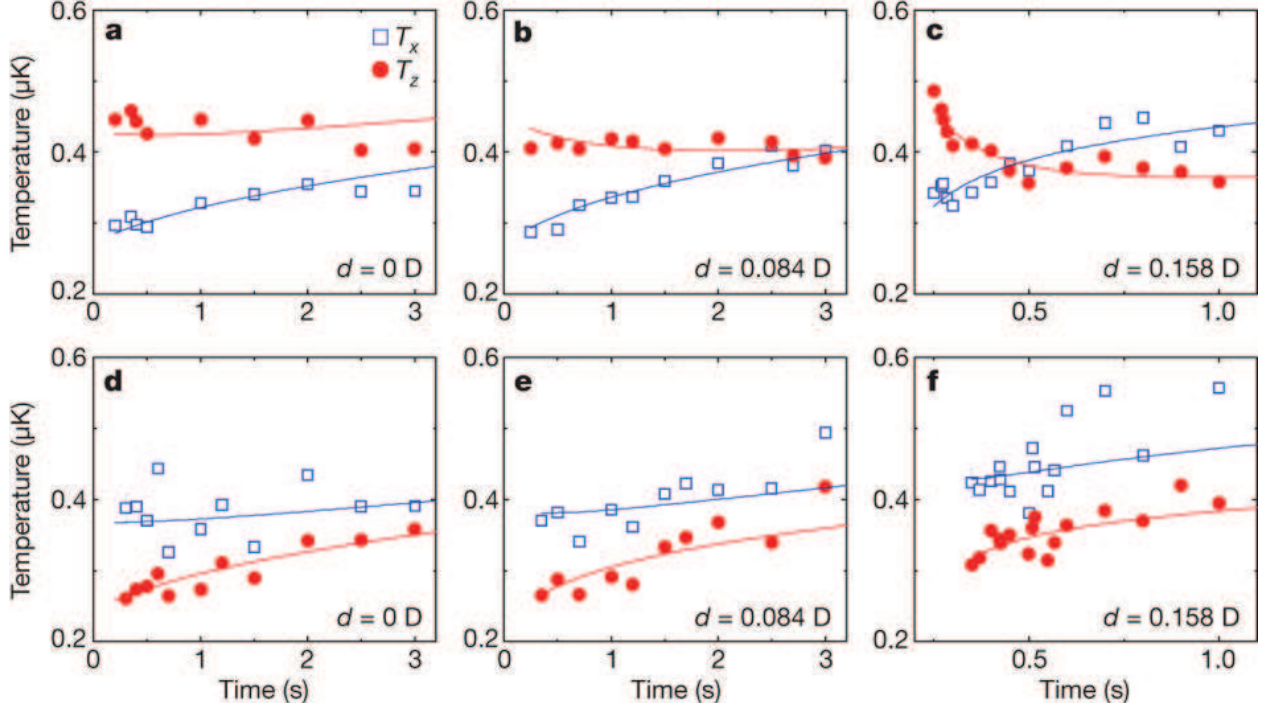


Figure 3.8: Cross-dimensional rethermalization in the polar molecule gas. Shown as a function of dipole moment, d , for $T_z > T_x$ (a-c) and $T_z < T_x$ (d-f). The experimental data shows difference between heating the gas in the vertical direction (a-c) and heating it in the horizontal directions (d-f). This provides evidence for the strong anisotropic characteristic of dipolar interactions. The electric field is applied along the \hat{z} direction. Figure reproduced from reference [40].

The differential equations used as model are shown as it follows. The solid lines in fig. 3.8 are a fit of the measured time evolution of n, T_z and T_x to the numerical solution of the following three differential equations [40]:

$$\frac{dn}{dt} = -(K_0 T_z + 2K_1 T_x) n^2 - \frac{n}{2T_z} \frac{dT_z}{dt} - \frac{n}{T_x} \frac{dT_x}{dt}, \quad (3.8)$$

$$\frac{dT_z}{dt} = \frac{n}{4} (-K_0 T_z + 2K_1 T_x) T_z - \frac{2\Gamma_{el}}{3} (T_z - T_x) + c_{bg}, \quad (3.9)$$

$$\frac{dT_x}{dt} = \frac{n}{4} K_0 T_z T_x + \frac{\Gamma_{el}}{3} (T_z - T_x) + c_{bg}. \quad (3.10)$$

Here we have allowed for a difference in the average energies per particle in the two trap directions, T_z and T_x . For the fits, we fix the d -dependent coefficients K_0 and K_1 using the previous fit to the inelastic loss rate data in fig. 3.5. In addition to heating due to inelastic loss, we include a measured background heating rate of $c_{bg} = 0.01 \mu\text{K s}^{-1}$. The elastic collision rate in eqs. 3.9 and 3.10 is given by $\Gamma_{el} = n\sigma_{el}v/N_{coll}$, where $v = \sqrt{8k_B(T_z + 2T_x)}/3\pi\mu$ and the constant N_{coll} is the mean number of collisions per particle required for rethermalization. We use $N_{coll} = 4.1$, which was computed for p-wave collisions [73]. However, we note that N_{coll} depends on the angular dependence of the scattering and may be different for dipolar elastic collisions.

Chapter 4

Polar Molecules in an 1D Optical Lattice: Going to 2D Geometry

The anisotropy of the dipolar interaction allows one to control scattering by controlling the orientation of the molecular dipole moment and the geometry of the external confinement. In this context, 2D geometries are of particular interest. Orienting the dipole moment of the molecules along the axis of tight confinement will result in a strong suppression of attractive “head-to-tail” collisions, if the confinement along that direction is sufficiently strong. This reduces inelastic scattering events in the molecular gas by a factor of 60 [74] and opens the path towards the study of long-lived ultracold polar molecular quantum gases and quantum degenerate molecular ensembles.

In our experiment, we realize a two-dimensional trapping geometry by means of a 1D optical lattice. This results in a stack of two-dimensional trapping geometries (pancakes) for the molecules. In this chapter, I will review the well-known concepts of optical dipole trapping and the realization of a 1D optical lattice. I will discuss how to describe particles in a periodic potential in terms of Bloch bands or Wannier functions. I will then introduce basic experimental techniques such as loading of molecular gases into the optical lattice and characterization techniques such as measurement of the momentum and quasimomentum distributions of the molecules in the optical lattice. Finally, I will discuss how to prepare ground-state polar molecules in the 1D optical lattice and how we achieve population control in selected vibrational levels of the optical lattice.

4.1 Atoms in an one-dimensional optical lattice

4.1.1 Optical dipole traps for neutral atoms and molecules

Atoms placed in an inhomogeneous light field will experience a force. This force relies on the interaction of the induced AC electric dipole of an atom with a far-detuned monochromatic laser field. The electric field \mathbf{E} of the laser will in general induce a dipole moment $\mathbf{d} = \alpha(\omega)\mathbf{E}$ in the atom, where $\alpha(\omega)$ is the complex a.c. polarizability and ω is the laser frequency.

The real part of the polarizability will then determine the so called dipole force of the inhomogeneous light field on the atom, given by [75, 76]:

$$F_{dip} = \mathbf{d} \cdot \nabla \mathbf{E}(\mathbf{r}) = \Re[\alpha(\omega)] \mathbf{E}(\mathbf{r}) \nabla \mathbf{E}(\mathbf{r}), \quad (4.1)$$

This force is associated with a corresponding dipole potential V_{dip} given by:

$$V_{dip} = \frac{1}{2\epsilon_0 c} \Re[\alpha(\omega)] I(\mathbf{r}). \quad (4.2)$$

where $I(\mathbf{r})$ is the intensity of the far-detuned light at the position \mathbf{r} of the atom.

The complex atomic polarizability is given by [75]

$$\alpha(\omega) = 6\pi\epsilon_0 c^3 \frac{\Gamma/\omega_0^2}{\omega_0^2 - \omega^2 - i(\omega^3/\omega_0^2)\Gamma}, \quad (4.3)$$

where Γ is the width of the relevant atomic transition, c is the light velocity, ϵ_0 is the permittivity constant in the vacuum, ω_0 is the resonant frequency of the atomic transition, and ω is the frequency of the light. By inserting eq. 4.3 in eq. 4.2 for the dipole potential we obtain:

$$V_{dip} = \frac{3\pi c^2}{2\omega_0^3} \left(\frac{\Gamma}{\omega - \omega_0} + \frac{\Gamma}{\omega + \omega_0} \right) I(\mathbf{r}), \quad (4.4)$$

This expression can be simplified by applying the the rotating wave approximation in the limit of large detuning:

$$V_{dip} = \frac{3\pi c^2}{2\omega_0^3} \left(\frac{\Gamma}{\Delta} \right) I(\mathbf{r}), \quad (4.5)$$

where $\Delta \equiv \omega - \omega_0$ is the detuning.

Eq. 4.5 explains the basic physics of dipole trapping in a far-detuned laser field. The potential scales as $I(r)/\Delta$. The potential depth therefore increases linearly with the intensity of the light field and decreases linearly with increasing detuning of the light field. Whether the potential is attractive or repulsive depends on the detuning of the light field relative to the relevant atomic transitions. For *red detuned* light, $\Delta < 0$, the dipole potential is attractive, and for *blue detuned* light, $\Delta > 0$, the potential is repulsive.

The simplest configuration for the realization of a confining potential by means of dipole potentials is therefore a single Gaussian laser beam with a frequency red-detuned from the relevant atomic transitions and focused down to a spot size of typically about 10-100 μm . The atoms will then be confined in the focus of this dipole trap with a strong confinement perpendicular to the axis of propagation of the laser light and a relatively weak confinement along the axis of propagation.

According to eq. 4.5, the depth of the confining potential is entirely set by the intensity of the light field and the detuning of the light frequency relative to the atomic transitions. At first sight, it might therefore seem favorable to operate dipole traps at small detunings to achieve a maximal depth at low intensity. However, atoms interacting with light fields will also scatter photon. Photon scattering results in heating of the atomic clouds. The photon scattering rate is determined by the imaginary part of the polarizability:

$$\Gamma_{sc} = \frac{1}{\hbar\epsilon_0 c} \Im[\alpha(\omega)] I(\mathbf{r}), \quad (4.6)$$

This expression can be simplified in a similar formalism as applied above to

$$\Gamma_{sc} = \frac{3\pi c^2}{2\hbar\omega_0^3} \left(\frac{\Gamma}{\Delta} \right)^2 I(\mathbf{r}). \quad (4.7)$$

As can be seen in eq. 4.7, the scattering rate scales $\propto I(r)/\Delta^2$. In particular, the photon scattering rate decreases much faster with increasing detuning (with the square of the detuning) as compared the potential depth (decreasing linearly with detuning). It is therefore favorable to operate optical dipole traps as far detuned as practically possible to avoid photon scattering processes that lead to heating of the confined atomic ensemble.

For more details please refer to reference [75] by R. Grimm *et al.*

4.1.2 One-dimensional optical lattice

A one-dimensional (1D) periodic lattice potential can be created by retro-reflecting a monochromatic laser beam and therefore super-imposing two counter-propagating light fields with a fixed phase relation with each other. This configuration will result in the formation of a standing wave with alternating intensity maxima and intensity minima. Neighboring intensity maxima/minima will be separated by $\lambda/2$, where λ is the optical wavelength for the lattice beam.

In the experiment, the optical lattice will be formed by two counter-propagating Gaussian laser beams with a typical waist of a few hundred μm . The resulting optical potential is then given by

$$V(r, z) = V_0 e^{-2\frac{r^2}{w^2(z)}} \cos^2(kz), \quad (4.8)$$

where $V_0 \equiv \frac{8P\alpha}{\pi w^2(z)}$, P is the laser power, $w(z) = w_0 \sqrt{1 + (z/z_R)^2}$ is the beam waist at z , w_0 is the beam waist at the focus, $k = 2\pi/\lambda$ is the wave number, λ is the wavelength of the laser light, α is the polarizability, and $z_R = \pi w_0^2/\lambda$ is the Rayleigh length.

For red detuned laser light, the atoms will be trapped in the anti-nodes of the standing wave (optical lattice), as shown in fig. 4.1. The one-dimensional optical lattice results in a trapping potential consisting of a stack of pancake-like traps. The confinement perpendicular to the plane of the pancake is much tighter than the confinement in the plane of the pancake

with trapping frequencies given by:

$$\omega_r = \sqrt{\frac{1}{m} \left(\frac{\partial^2 V(r, z)}{\partial r^2} \right)_{r, z=0}} = \sqrt{\frac{4E_{rec}}{mw_0^2}} \sqrt{\frac{V_0}{E_{rec}}}, \quad (4.9)$$

and

$$\omega_z = \sqrt{\frac{1}{m} \left(\frac{\partial^2 V(r, z)}{\partial z^2} \right)_{r, z=0}} = \frac{2E_{rec}}{\hbar} \sqrt{\frac{V_0}{E_{rec}}}, \quad (4.10)$$

respectively. Here, $E_{rec} = \frac{\hbar^2 k^2}{2m}$ is the recoil energy associated with the lattice photon. Atoms in a single pancake are trapped in 2D-geometry if the optical lattice potential is sufficiently deep.

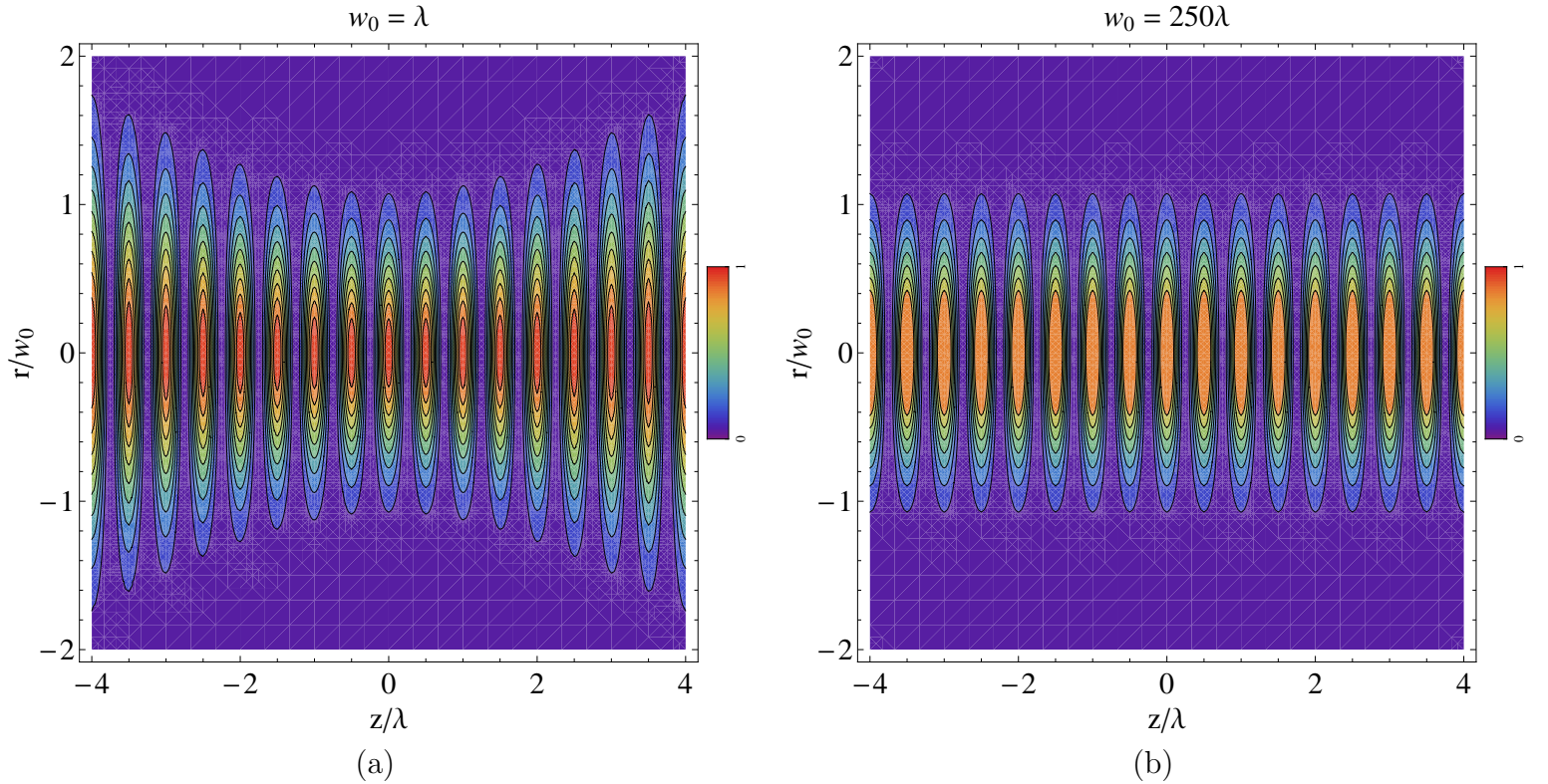


Figure 4.1: Illustrative contour plot of one-dimensional optical lattice potential. (a) Normalized potential in false color for $w_0 = \lambda$. (b) Potential for $w_0 = 250\lambda$. The point with maximum density are the anti-nodes where, for a red-detuned optical lattice, the particles will be trapped. In our case, the lattice beam waist is $w_0 \approx 250\mu m$.

4.1.3 Experimental realization of a 1D optical lattice

In the experiment, we realize a 1D optical lattice by retroreflecting a Gaussian laser beam with a beam waist of $250 \mu\text{m}$. The optical lattice is operated red-detuned to all atomic and molecular transitions in the ^{40}K , ^{87}Rb and $^{40}\text{K}^{87}\text{Rb}$ system, with wavelength of 1064 nm. The one-dimensional optical lattice is overlapped with the crossed beam optical dipole trap described in chapter 2. The optical lattice beam propagates along the tight axis of the pancake shaped optical dipole trap and therefore, cuts a single loose pancake into a stack of about 30 tightly confining pancakes.

Using the optical lattice, it is possible to trap atoms and molecules in a two-dimensional trapping geometry. Here we define 2D trapping by the criterion $\hbar\omega_z \gg k_B T$. In this regime, the motion of particles will be restricted to a single quantum state along the axis of tight confinement.

As an illustrative example, the trapping frequencies for ^{87}Rb in the radial and axial direction respectively are shown as a function of optical lattice depth in fig. 4.2. As can be seen in the diagram, the confinement along the axial direction - that means the confinement in a single pancake - is much tighter than the confinement in the radial direction. In particular, it is possible to enter a regime of 2D confinement where $\hbar\omega_z \gg k_B T$. Note that 2 kHz trap frequency correspond to an equivalent temperature via $T = \hbar\nu/k_B T$ of about 100 nK. At a temperature of around 100 nK, the regime of 2D confinement for ^{87}Rb sets in at a lattice depths around $1 E_{rec}$. A very similar criterion can be derived for $^{40}\text{K}^{87}\text{Rb}$ molecules. This is the regime that is of particular interest for the control and study of dipolar collisions. It is in this regime that scattering properties between fermionic polar molecules can be significantly altered as compared to a three-dimensional geometry (see chapter 5).

By increasing the optical lattice depth, it is possible to continuously tune the trapping geometry of particles confined in the optical lattice from 3D ($\hbar\omega_z \ll k_B T$) to a 2D configuration ($\hbar\omega_z \gg k_B T$) and, therefore control molecular scattering processes by means of

external confinement.

4.1.4 Quantum mechanical description of a particle confined in a periodic potential: Bloch bands

The quantum mechanical picture of a particle moving in a periodic potential is a well known problem. The description of atomic motion is captured by the formalism of Bloch wavefunctions and Bloch bands [77]. The periodic potential in this case is provided by the interference pattern of light. A single particle of mass m moving in this periodic potential $V(z) = V_0 \cos^2(kz)$ is described by the time-independent Schrödinger equation:

$$\left(-\frac{1}{2m} p^2 + V_0 \cos^2(kz) \right) \Psi_{q,n}(z) = E_{q,n} \Psi_{q,n}(z), \quad (4.11)$$

where n is the quantum number relative to the internal state of the optical lattice. The eigenfunctions of this Schrödinger equation are called Bloch waves. These Bloch functions can be written as the product of the plane waves $e^{iqz/\hbar}$ with quasimomentum q times an

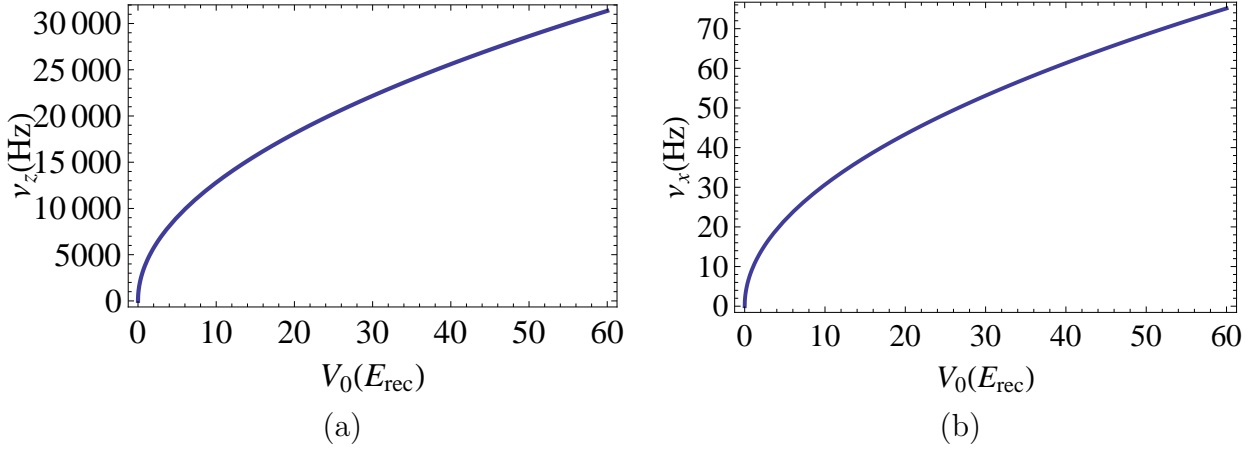


Figure 4.2: Optical lattice's trap frequencies versus the trap depth for ^{87}Rb . These two plots show the axial frequency ν_z compared to the radial frequency ν_r . The confinement in the axial direction is much tighter than the radial direction. The optical lattice parameters are: $\lambda = 1064 \text{ nm}$, and the beam waist is $250 \mu\text{m}$.

envelope function $u_{q,n}(z)$ with the periodicity of the confining potential:

$$\Psi_{q,n}(z) = e^{iqz/\hbar} u_{q,n}(z). \quad (4.12)$$

These wavefunctions are delocalized over the whole lattice structure.

Due to the periodicity, we can expand both the external potential and the wavefunctions in terms of a Fourier sum:

$$V(z) = \sum_j V_j e^{i2jkz}, \quad (4.13)$$

and

$$u_{q,n}(z) = \sum_l c_l^{(q,n)} e^{i2lkz}. \quad (4.14)$$

Substituting eq. 4.13 and eq. 4.14 into eq. 4.11 and after some algebraic manipulations, the Schrödinger equation can be written in a matrix form given by [77]:

$$\left\{ \left[\left(2l + \frac{q}{\hbar k} \right)^2 E_{rec} - \frac{V_0}{2} \right] \delta_{l,l'} - \frac{V_0}{4} \delta_{l,l' \pm 1} \right\} c_l^{(q,n)} = E_{q,n} c_l^{(q,n)}, \quad (4.15)$$

where $-\hbar k \leq q \leq \hbar k$, limited to the first Brillouin zone. $E_{q,n}$ represents the eigenenergies of the n^{th} Bloch band for a given q . The eigenstates $c^{(q,n)}$ are the Bloch wavefunctions.

Note that we have introduced an additional quantum number, the band index n . The quasimomentum q is unique only up the addition of integer multiples of the reciprocal lattice vector k . It is therefore convenient to restrict the quasimomenta to the first Brillouin zone given by $-\hbar k < q < \hbar k$. This means that a multiple number of eigenfunctions and eigenstates exists for a given quasimomentum q . These eigenstates are denoted by the band index n .

Fig. 4.3 shows the energy spectrum of particles confined in optical lattices for various lattice depths. In the limit of vanishing optical lattice potential, the quasimomentum q is equal to the free particle momentum and the energy spectrum is given by the free particle energy dispersion $E_q = \hbar^2 q^2 / 2m$. The band structure in this case appears due to the artificial

mapping of quasimomenta onto the first Brillouin zone. With increasing lattice depth, an energy gap appears between the different energy bands. This gap increases with increasing lattice depth whereas the width of the Bloch bands becomes smaller. Finally, the Bloch bands converge to harmonic oscillator states in a single lattice well in the limit of very deep optical lattices.

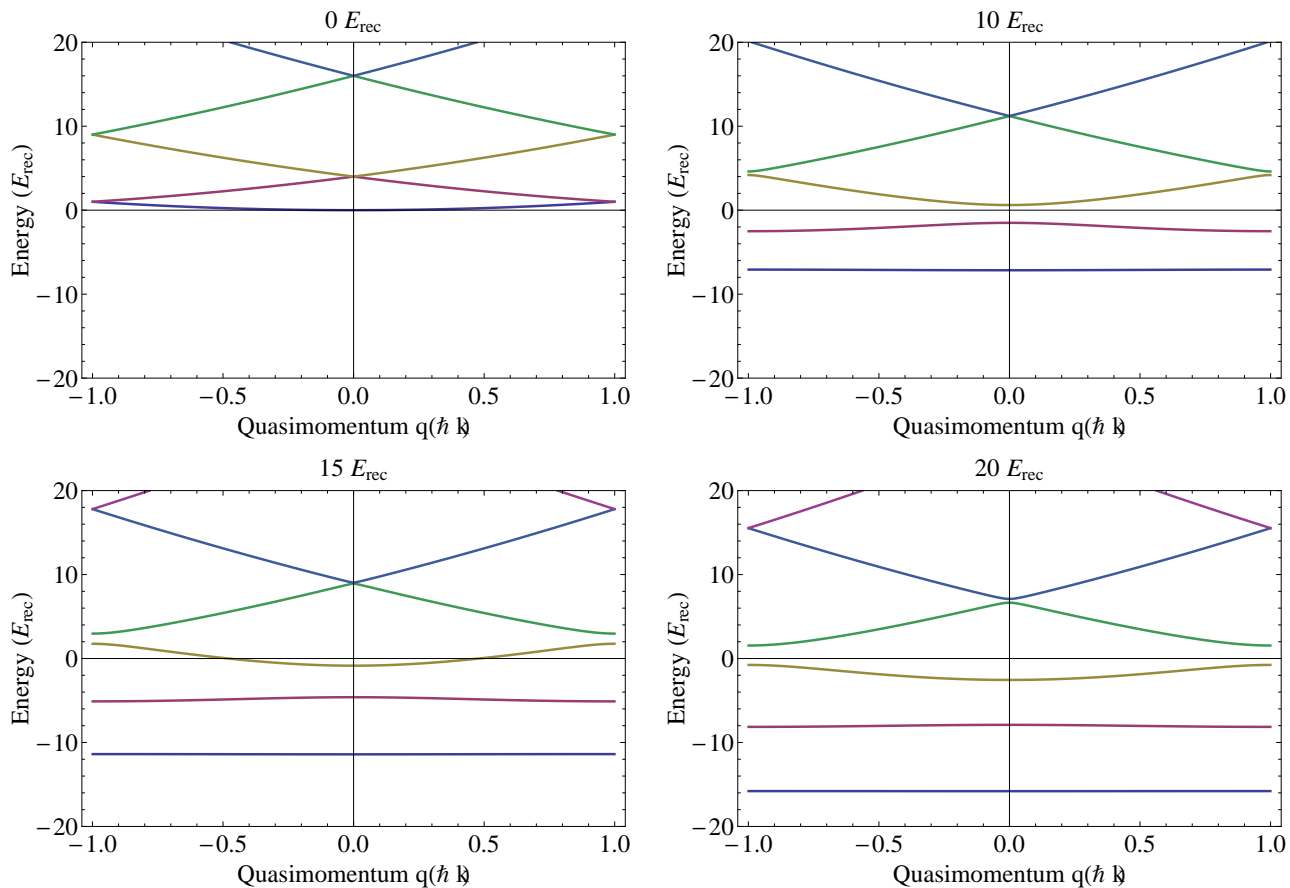


Figure 4.3: Bloch bands in the one-dimensional optical lattice. Energy versus quasimomentum in the first Brillouin zone for different lattice depths. The lattice depths are 0, 10, 15, and 20 E_{rec} . As the lattice height increases, the separation between the Bloch bands also increases and the energy levels flattens out.

This is illustrated in fig. 4.4, where we show behavior of the first four energy levels versus the lattice depth at quasimomentum $q = 0$. Above $30E_{rec}$, energy levels flatten out and the gap between energy levels converges towards the energy splitting between harmonic

oscillator states in a harmonic trapping potential $\hbar\omega_z$. The eigenstates for deep lattices is given by localized wavefunctions called Wannier functions.

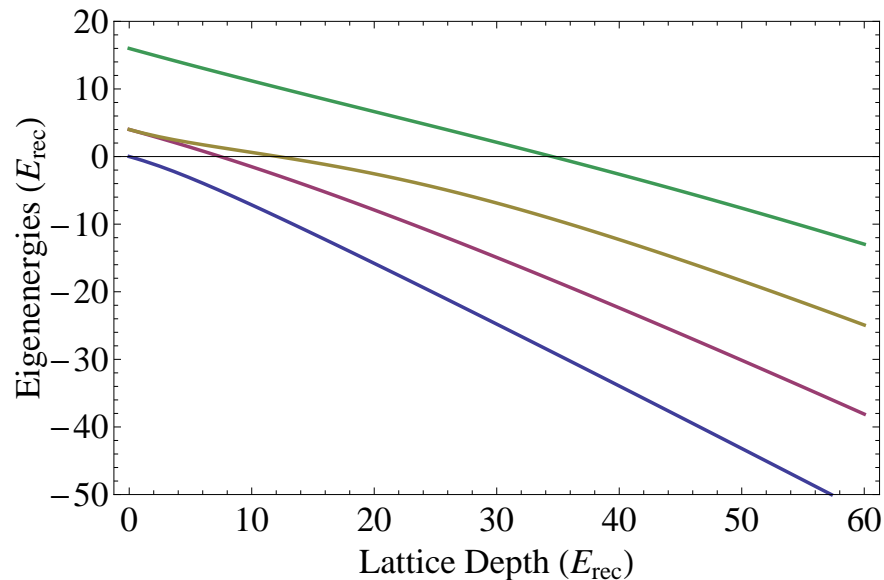


Figure 4.4: First four energy levels versus the lattice depth with quasimomentum $q = 0$, for an atom in an optical lattice. For lattice depths above $30E_{rec}$, the spacing between the energy levels approaches $\hbar\omega_z$ like a harmonic oscillator energy.

4.1.4.1 Wannier functions

Bloch wavefunctions are the common quantum mechanical description of particles moving in a periodic potential. However, these wavefunctions are delocalized over the lattice. Sometimes it is more convenient to approach the description of particles in the periodic potential by means of localized wavefunctions, with interactions of particles on a single lattice site and tunneling of particles from one lattice well to the next. In this case, it is appropriate to think of the optical lattice as an infinite chain of harmonic oscillator wells coupled to each other through tunneling processes. The wavefunctions used in this formalism are called Wannier functions and they approach harmonic oscillator states in the limit of very deep optical lattices. A good review is provided in Ana Maria Rey's Ph.D. thesis [78].

The Wannier functions are the Fourier transform of the Bloch functions and therefore defined as:

$$w_n(z - z_i) = \frac{1}{\sqrt{A}} \sum_q e^{-iqz_i/\hbar} \Psi_{q,n}(z). \quad (4.16)$$

where A is a normalization constant and $\Psi_{n,q}(z)$ is the Bloch function eq. 4.12.

To calculate the probability of a particle tunneling from site i to a neighboring site j , we need to know the tunneling energy for 1D optical lattice. This energy is given by [77]

$$J_z = \int w_1(z - z_i) \left(-\frac{\hbar^2}{2m} \frac{\partial^2}{\partial z^2} + V_0 \cos^2(kz) \right) w_1(z - z_j). \quad (4.17)$$

The tunneling matrix element J , which describes the tunnel coupling between lattice sites, is directly related to the width of the first Bloch band [77]:

$$J = \frac{(\max(E_{q,0}) - \min(E_{q,0}))}{4}. \quad (4.18)$$

The tunneling energy corresponds typically to a timescale for particles tunnel from one lattice site to the next. The time scale is given by $t = \hbar/J$.

In fig. 4.5, we show the tunneling time for ^{40}K and ^{87}Rb atoms versus the optical lattice depth. The tunneling times for ^{40}K atoms and ^{87}Rb atoms are significantly different. ^{40}K atoms are lighter than ^{87}Rb atoms and in the same lattice depth therefore have a higher E_{rec} and a higher probability to tunnel from one lattice site to the next than ^{87}Rb . At a lattice depth of $19 E_{rec}^K$ for ^{40}K and $42 E_{rec}^{Rb}$ for ^{87}Rb , the tunneling time for ^{40}K is 300 ms and for ^{87}Rb is 1 s. Note that, these two lattice depths are different when they are expressed in terms of the recoil energies of ^{40}K and ^{87}Rb , which are different because of the difference in mass of each atom (given that they are in the same optical lattice, and they also have similar polarizabilities).

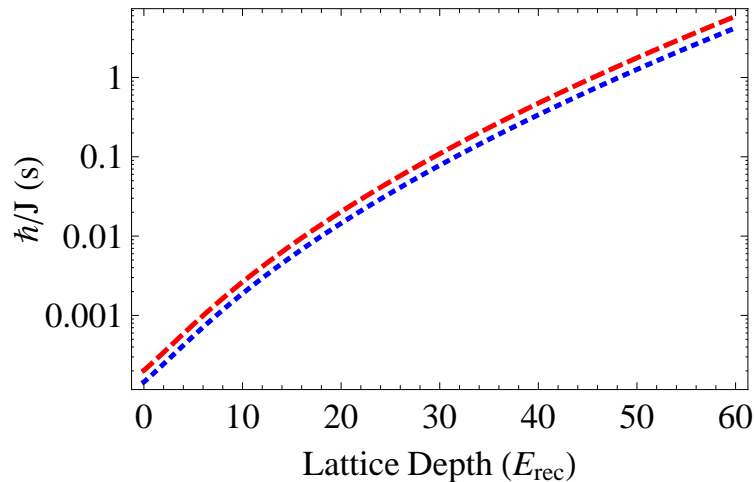


Figure 4.5: Semi-log plot of tunneling time in an 1D optical lattice versus lattice depth. Dotted blue line is for ^{40}K and red dashed line is for ^{87}Rb . For our typical conditions, the tunneling time for ^{40}K is 300 ms (for $19 E_{rec}^K$) and for ^{87}Rb is 1 s (for $42 E_{rec}^{Rb}$).

4.2 Characterizing the optical lattice

Experimental studies of atoms or molecules in the optical lattice rely on an accurate knowledge of the depth of the optical lattice and corresponding trapping frequencies of atoms or molecules in a single well of the optical lattice. In the following, we will introduce two experimental techniques for the characterization of the depth of the optical lattice. The first relies on parametric heating of atoms or molecules in the optical lattice - therefore providing a direct measurement of the trapping frequencies and the energy splitting between bands in the limit of strong confinement. The second technique relies on Kapitza-Dirac scattering of atoms off a periodic potential.

4.2.1 Measuring the trapping frequencies by parametric heating

One very common method for the calibration of the optical lattice depth is to parametrically heat the ensemble in the optical lattice. For parametric heating the system, is driven periodically at twice the trapping frequency of the particles confined in the potential, for ex-

ample, by modulating the lattice beam intensity. This will deposit energy in the system and in particular drive transitions from e.g. the lowest harmonic oscillator state to the second excited harmonic oscillator state ($n = 2$). In the band picture of the optical lattice, this is equivalent to driving transitions from the first to the third band of the optical lattice and therefore allows to study the energy difference between these two bands. Due to the finite width of the involved bands, calibration of the optical lattice depth via parametric heating has to be performed either with an atomic cloud occupying only the lowest quasimomentum of the optical lattice ($q = 0$) or in the limit of a very deep optical lattice where the width of the involved bands tends to zero. As an illustrative example of the intrinsic uncertainty for this measurement, let us consider an optical lattice of $40 E_{rec}$. The energy difference between the first and the third band is then $> 20 E_{rec}$ with a width of each band of $< 0.3 E_{rec}$, corresponding to a relative uncertainty of < 0.015 .

In order to know the trap frequency of the optical lattice in the vertical direction for the molecules, we perform the calibration procedure with ^{40}K - ^{87}Rb Feshbach molecules. A typical calibration procedure for the optical lattice using parametric heating is performed in the following way: a sample of Feshbach molecules, ^{40}K - ^{87}Rb , is prepared in the optical dipole trap. The lattice is then adiabatically ramped up in 150 ms to a lattice depth of $100 E_{rec}$. The optical lattice is then modulated with a relative amplitude of approximately 20-30 % for about 300 μs . This time scale corresponds to approximately 10 cloud oscillations. Fig. 4.6 shows a typical resonance feature for parametric heating of atoms in the optical lattice. As a function of the frequency of the drive, we observe the width of the cloud, σ , after 5 ms time of flight, and therefore the temperature ($T \propto \sigma^2$) of the cloud to vary by about a factor of four in the vicinity of the resonance! e. The resonance feature has typically a gaussian rms width of 5 kHz and a resonance frequency of 44(5) kHz. A more systematic study of the dependence of the trap frequency, ν_z , versus the amplitude of the drive would be necessary to determine the trap frequency with a smaller error. In chapter 5 we also use the parametric heating idea to excite molecules to higher bands in a controlled way.

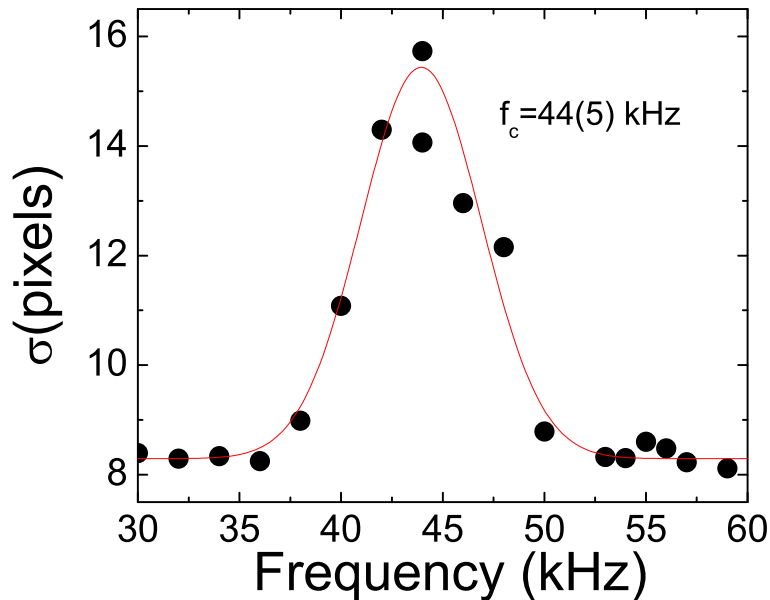


Figure 4.6: Trap frequency measurement for Feshbach molecules ^{40}K - ^{87}Rb via parametric heating. σ is the molecular cloud width in the \hat{z} direction. The center frequency is 44 kHz, which indicates that the axial frequency of the optical lattice is 22 kHz. The ramp procedure for this measurement is similar to the one described in chapter 5 in fig. 5.2 except with a sudden turn off of the end of the ramp.

4.2.2 Kapitza-Dirac Scattering

Kapitza-Dirac scattering is the diffraction of matter waves off an off-resonance light field. The diffraction results in a coherent mixing of momentum modes [79]. Starting from a BEC of e.g. ^{87}Rb atoms, the atoms occupy a single collective state with momentum near $q = 0$, where the momentum spread is much smaller than $|\hbar k|$. The dynamics of the matter wave diffracting off a standing light wave can then be nicely observed. While interacting with a standing wave interference pattern of light the atoms will constantly absorb and immediately reemit photons. This changes the atomic momentum along the standing wave axis by either zero or two-photon momenta. The momentum distribution of atoms after the interaction with the standing light field can then be probed by projecting the atomic

quasimomentum onto free space momentum in time of flight expansion.

As a particular case of Kapitza-Dirac scattering, we operate in the Raman-Nath regime where the atom motion during the interaction with the light field can be neglected. The population of the diffracted states then only depends on the area of the applied pulse [79], i.e., $\omega\tau \ll 1$, where τ is the pulse duration and ω is the harmonic oscillator frequency. In our experiment, τ is on the order of tens of μs and $\omega = 2\pi \times 28 \text{ kHz}$.

In our experiment, we use Kapitza-Dirac scattering of a ^{87}Rb BEC for an accurate determination of the depth of the optical lattice. The number of atoms, P_n , in the n^{th} diffraction order observed in momentum space as a function of interaction time τ is given by a Bessel function of the first kind J_n [79]:

$$P_n = J_n^2\left(\frac{V_0\tau}{2\hbar}\right). \quad (4.19)$$

where, V_0 is the lattice depth. The dynamics of the atomic population during the pulse in different diffraction orders then gives accurate information on the optical lattice depth.

Fig. 4.7 shows the experimental procedure for measuring the depth of an optical lattice by means of matter wave diffraction. First, a BEC is prepared in an optical dipole trap. The optical dipole trap is then suddenly turned off and at the same time the optical lattice is flashed on for a variable amount of time τ - typically on the order of tens of μs . Fig. 4.8 shows the dynamics of the diffraction pattern of a ^{87}Rb BEC matter-waves versus the hold time in the lattice. From these images we extract the fractional amplitudes of different $\hbar k$ momentum diffraction order and fit the data to a numerical solution of eq. 4.11 following reference [79]. Here, only the trap depth is a free parameter. In the particular example, we extract a depth of $42 E_{\text{rec}}$.

The discrepancy for the optical lattice's trap frequency determined via parametric heating and via Kapitza-Dirac scattering is 15%, where the first is smaller than the second. For Kapitza-Dirac scattering with ^{87}Rb , we know the frequency of the optical lattice for ^{87}Rb

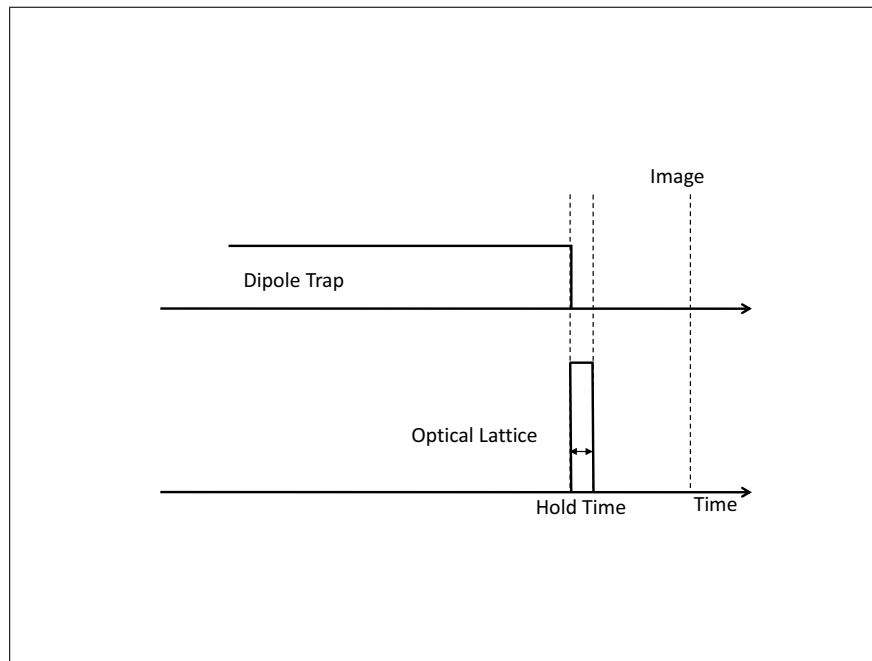


Figure 4.7: Ramp procedure to measure trap depth of the optical lattice. The depth measurement is done with a ^{87}Rb BEC. The optical lattice is diabatically pulsed on and briefly switched off in order to excite ^{87}Rb atoms to higher bands. The hold time is varied on the order of tens of microseconds. The time of flight is 5 ms, and the lattice height is $42 E_{rec}$.

atoms. Then we obtain the optical lattice frequency for $^{40}\text{K}^{87}\text{Rb}$ by doing a mass scaling between ^{87}Rb and $^{40}\text{K}^{87}\text{Rb}$. For the parametric heating we have a direct measurement of the trap frequency for $^{40}\text{K}^{87}\text{Rb}$. This is the reason why we trust it more than the Kapitza-Dirac scattering to determine the optical lattice trap frequency.

4.3 Loading atoms into the optical lattice

The loading of ultracold atoms or molecules into the optical lattice has to ensure a controlled transformation of a harmonic optical dipole potential into a periodic potential. In particular, it is important that atomic or molecular motional states in the initial harmonic oscillator potential are adiabatically transferred into motional states of the final periodic potential.

An illustrative example is given by the loading of a Bose-Einstein condensate into an

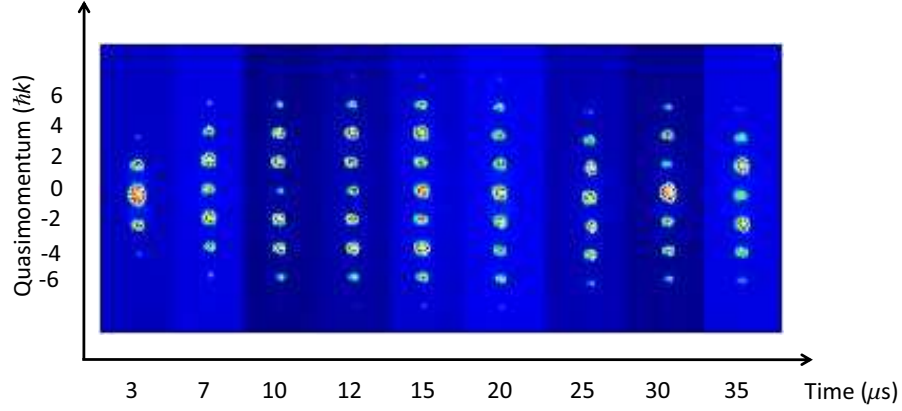


Figure 4.8: ^{87}Rb BEC matter-wave diffraction into discrete momentum components.

optical lattice. Starting from a Bose-Einstein condensate in the lowest harmonic oscillator state in the harmonic optical dipole potential, the loading procedure should ensure that the atoms in the condensate remain in the lowest possible energy state. In the case of the optical lattice, this lowest energy state is given by the Bloch state with quasimomentum $q = 0$. The previous Kapitza-Dirac scattering discussed in section 4.2 provides an example when the transfer is not adiabatic.

The adiabaticity condition with respect to band population for loading atoms with quasimomentum q in the lowest Bloch state, $|0, q\rangle$ is given by [80]:

$$\left| \left\langle 1, q \left| \frac{\partial H}{\partial t} \right| 0, q \right\rangle \right| \ll \Delta E^2(q, t)/\hbar, \quad (4.20)$$

where $|1, q\rangle$ is the first excited Bloch state, and ΔE is the energy difference between $|0, q\rangle$ and $|1, q\rangle$.

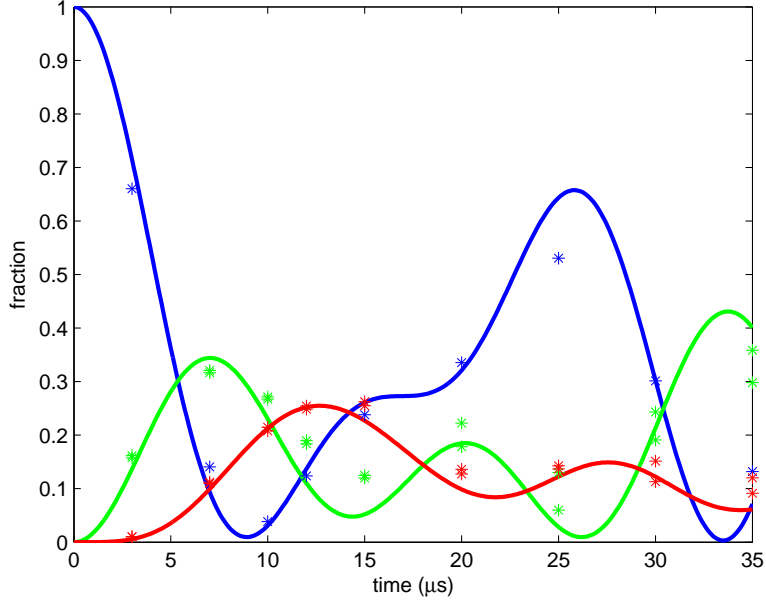


Figure 4.9: Extracted relative population of momentum components versus pulse duration. The lines show a fit to eq. 4.19. The optical lattice depth as a free parameter, and the extracted one from the data is $42 E_{rec}$. The optical lattice parameters are $\lambda = 1064$ nm, beam waist of $250 \mu\text{m}$, and laser power of 1 W. The three curves show the $0\hbar k$ (solid blue), $\pm 2\hbar k$ (solid green), and $\pm 4\hbar k$ (solid red) momentum components.

For a ^{87}Rb bosonic condensate, where the atoms all accumulate in the $q = 0$ state at zero lattice depth, the splitting between the two lowest bands at $q = 0$ is $\Delta E = 4E_{rec}$ for lattice height $V_0 = 0$. If $q = 0$, eq. 4.20 reduces to [81]:

$$\frac{1}{E_{rec}} \frac{d}{dt} V_0 \ll 32\sqrt{2} \frac{E_{rec}}{\hbar}. \quad (4.21)$$

A linear ramp of the optical lattice should occur with rate no higher than $\frac{4E_{rec}}{100\mu\text{s}}$ to ensure adiabatic loading.

Fig. 4.10 shows the energy difference ΔE versus lattice depth V_0 for three different quasimomenta. With increasing quasi momentum, the energy gap decreases for small optical lattice depth. The loading of a fermionic gas occupying a continuous quasimomentum distribution up to a characteristic energy scale given by the Fermi energy then poses a much

more stringent criterion for the timescales for adiabatic loading than a BEC.

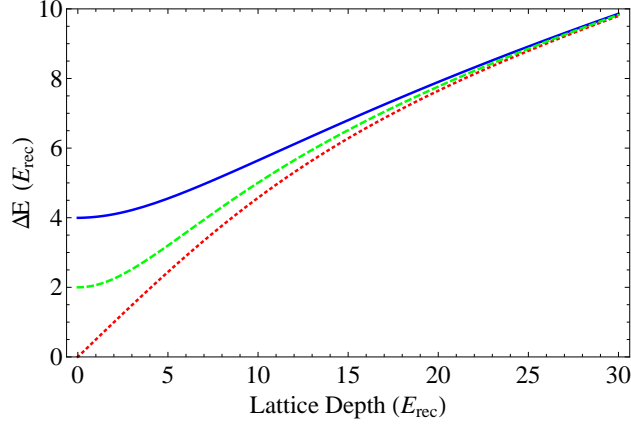


Figure 4.10: Energy gap between lowest and first excited Bloch bands for different quasimomenta. Solid blue line is for $q = 0$, dashed green line is for $q = 0.5 \hbar k$, and red dotted line is for $q = \hbar k$.

4.3.1 Loading atoms in the optical lattice

In this section, I present the experimental procedure for loading the optical lattice with ^{40}K and ^{87}Rb atoms. In order to load the atoms in the lattice and avoid heating them, the adiabaticity criterion, eq. 4.20, has to be satisfied. For ^{40}K and ^{87}Rb atoms, the ramp rate has to be lower than $\frac{4E_{rec}}{100\mu s}$. We exponentially ramp up the lattice in 150 ms as shown in fig. 4.11. The dipole trap is ramped down adiabatically within the same time scale. Note that we choose 150 ms as ramping time arbitrarily, just to be safe with respect to the adiabaticity criterion.

Note that the lifetime of atoms in the optical lattice is much longer than the timescales associated with adiabaticity. For ^{87}Rb , we observe a lifetime of 5(1) s and for ^{40}K is the lifetime 8(1) s, as shown in fig. 4.12 (a) and (c).

We have also measured the heating rates of atoms in the optical lattice and find them to be comparable to heating observed in our dipole trapping potentials [21]. For ^{87}Rb , we observe a heating rate of 6.1(5) nK/s and for ^{40}K 5(1) nK/s, as shown in fig. 4.12 (b) and

(d).

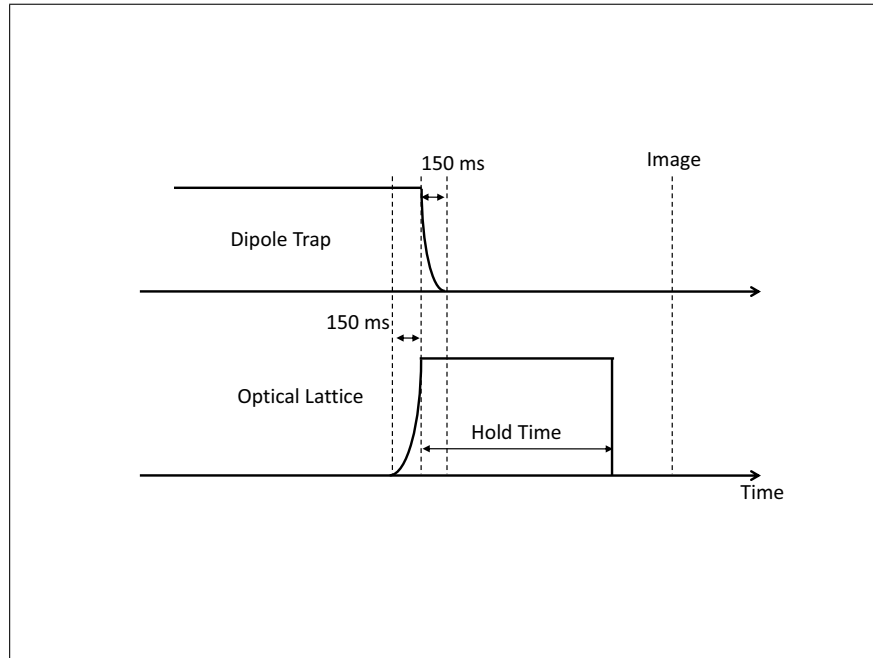


Figure 4.11: Ramping procedure to adiabatically load ^{40}K and ^{87}Rb in the optical lattice. The optical lattice depth for ^{87}Rb is $42 E_{rec}^{Rb}$ and for ^{40}K is $19 E_{rec}^K$.

4.4 Probing the quasimomentum distribution of atoms in optical lattices.

For our experiments it is very important to know the distribution of atoms and molecules over different quasimomentum states and Bloch bands in the optical lattice. This distribution can be probed by adiabatically ramping down the optical lattice potential with respect to the band separation $\tau \gg \omega_z^{-1}$. For the experiment described in this section, $\tau =$

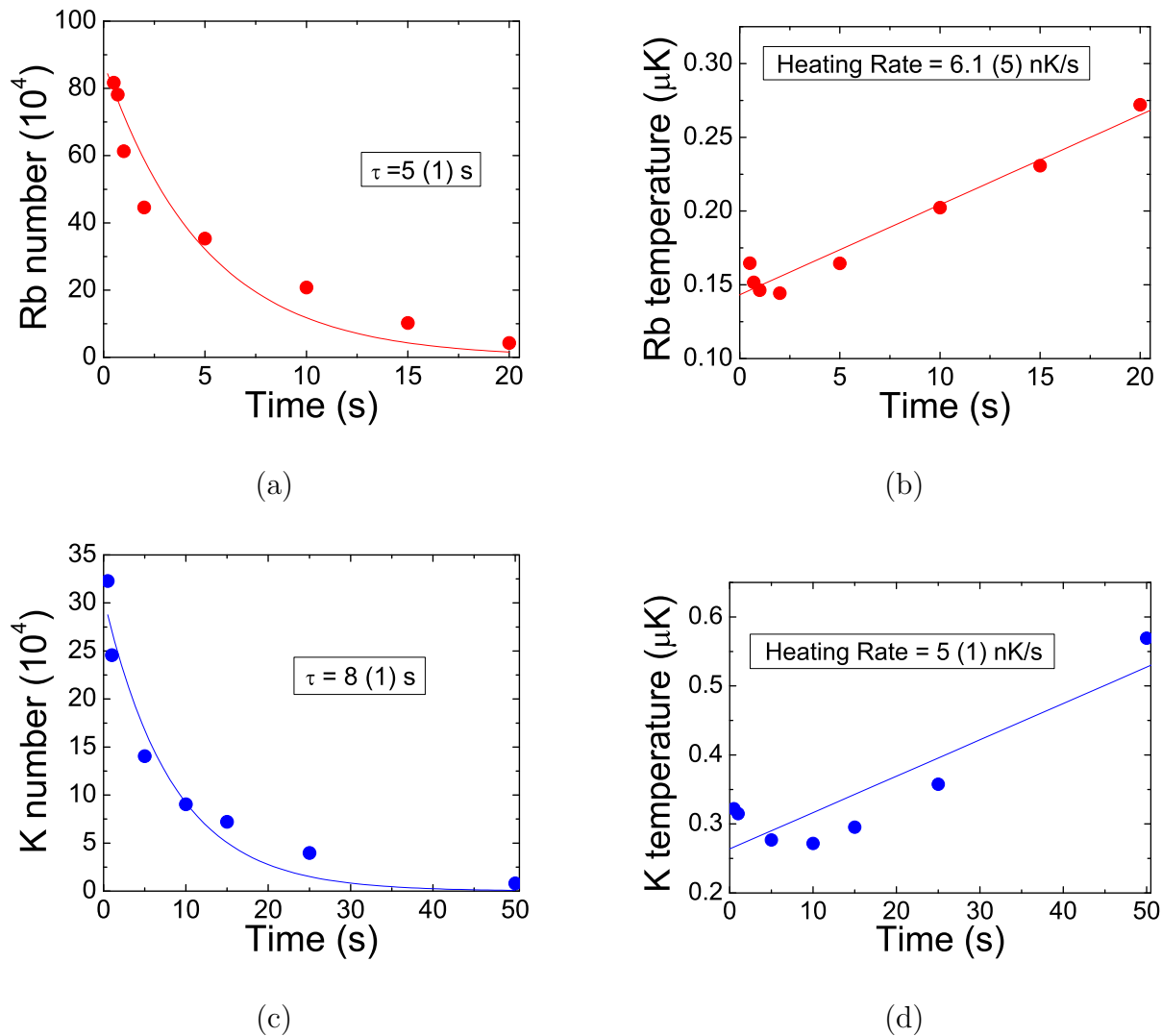


Figure 4.12: Lifetime of ^{87}Rb and ^{40}K atoms and respective heating rates in the optical lattice.

500 μs and $\omega_z^{-1} \approx 4 \mu\text{s}$, for lattice depth of 17.7 E_{rec} . Note that, we choose 500 μs to ramp our lattice down, because if we go slower the atoms will free fall due to the gravity. This procedure results in an adiabatic conversion of quasimomentum into free-space momentum. The resulting free-space momentum distribution can then be probed in time of flight absorption imaging.

Fermionic atoms always occupy a continuous distribution of quasimomenta. This is in contrast to a BEC where all atoms accumulate in the zero quasimomentum state. Depending on the quasimomentum distribution of the fermionic atoms, the lowest Bloch band can then be partially or entirely populated. Increasing the atom number or the temperature of the fermionic cloud can result in a population of fermions in several Bloch bands.

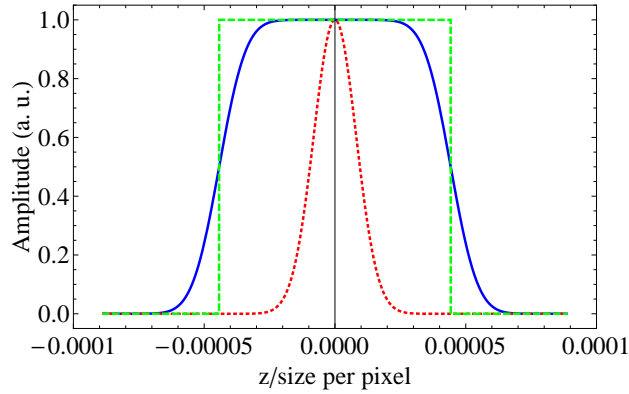


Figure 4.13: Calculated functions for the distribution in quasimomentum space at the first Brillouin zone in the optical lattice. Red dotted curve is a gaussian function, green dashed curve is a Heaviside function, and solid blue line is the convolved curve that is used to fit the atomic cloud along the lattice axis.

By converting the quasimomentum distribution into a free-space momentum distribution adiabatically, we can then accurately determine the fraction of atoms/molecules in different bands. This is performed by fitting the atomic momentum distribution after time of flight absorption to a “wedding cake”-like structure [82, 83]. Here, the edges of the wedding cake occur at integer multiples of $\hbar k$ and correspond to the edges of the n^{th} Brillouin zone. However, due to limitations in our image resolution, we are not able to resolve the sharp

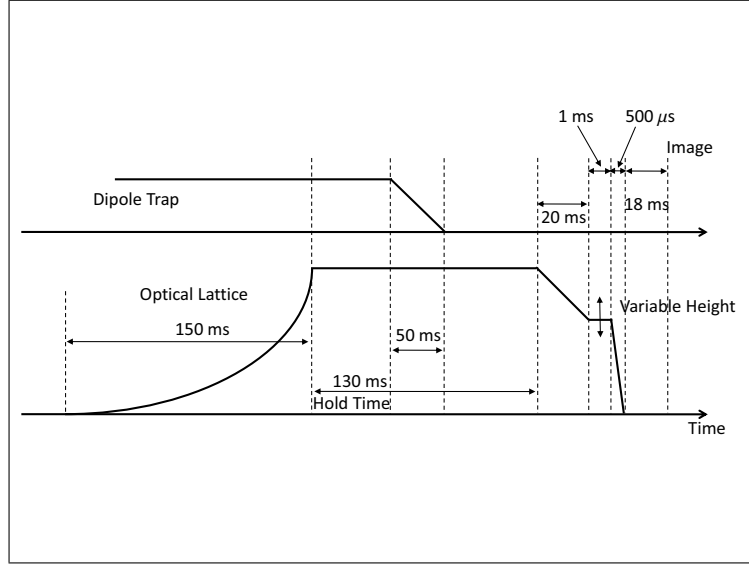


Figure 4.14: Band mapping with filtering of ^{40}K in higher bands. The optical lattice is adiabatically ramped up exponentially in 150 ms to $17.7 E_{rec}$. At the beginning the optical lattice and the optical trap are combined to hold the atoms against the gravity. The filtering is done for two different lattice heights: $3.2 E_{rec}$, and $14.5 E_{rec}$.

edges in the momentum distribution. To model this, we convolute a single step function (Heaviside function) with a Gaussian function accounting for the finite imaging resolution:

$$\int_{-\infty}^{\infty} \left[\Theta \left(\frac{\Delta + 2x}{2\sigma} \right) - \Theta \left(\frac{\Delta - 2x}{2\sigma} \right) \right] e^{-\frac{(x-z)^2}{2\sigma^2}} dx = \sigma \sqrt{\frac{\pi}{2}} \left[\text{Erf} \left(\frac{\Delta + 2z}{2\sqrt{2}\sigma} \right) + \text{Erf} \left(\frac{\Delta - 2z}{2\sqrt{2}\sigma} \right) \right], \quad (4.22)$$

where x is a variable which is integrated, z is a variable representing the vertical coordinate at \hat{z} direction, Erf is the error function, σ is the rms width of the gaussian model of our image resolution, and Δ is the size of the expanded cloud corresponding to the first Brillouin zone, $2\hbar k$. Since both z and σ are conveniently measured in units of pixels, we convert Δ to units of pixels as well:

$$\Delta = \frac{2\hbar k}{m_K} \frac{T_{TOF}}{2 \times 5.4 \mu\text{m}/\text{pixel}}, \quad (4.23)$$

where $T_{TOF} = 18$ ms is the time of flight, m_K is the atomic mass of ^{40}K , σ is the image resolution in pixels, and $5.4 \mu\text{m}/\text{pixel}$ is the conversion from micrometers to pixels at the image. The factor of 2 multiplying the $5.4 \mu\text{m}/\text{pixel}$ is because of the binning of the image was 2. Fig. 4.13 shows the Heaviside (dashed green), the Gaussian (dotted red) and the resulting convoluted (solid blue) functions.

We multiply the result of eq. 4.22 by $A/2$ where A is an amplitude scaling factor, and also by shifting the center of the function by z_c . We replace the amplitude because we want to extract the relative atom (molecule) population in the lattice levels. We then fit the data with three free parameters: the amplitude A , the image resolution σ , and the center z_c (z_c is also in units of camera pixels). The fitting function for atomic distribution in the first Brillouin zone is given by:

$$f(z) = A/2 \left[\text{Erf} \left(\frac{\Delta + 2(z - z_c)}{2\sqrt{2}\sigma} \right) + \text{Erf} \left(\frac{\Delta - 2(z - z_c)}{2\sqrt{2}\sigma} \right) \right], \quad (4.24)$$

and the fitting function for a distribution in both first and second Brillouin zones is given by:

$$\begin{aligned} f(z) = & A/2 \left[\text{Erf} \left(\frac{\Delta + 2(z - z_c)}{2\sqrt{2}\sigma} \right) + \text{Erf} \left(\frac{\Delta - 2(z - z_c)}{2\sqrt{2}\sigma} \right) \right] \\ & + B/2 \left[\text{Erf} \left(\frac{-\Delta + 2(z - z_c)}{2\sqrt{2}\sigma} \right) + \text{Erf} \left(\frac{-\Delta - 2(z - z_c)}{2\sqrt{2}\sigma} \right) \right] \\ & + B/2 \left[\text{Erf} \left(\frac{2\Delta + 2(z - z_c)}{2\sqrt{2}\sigma} \right) + \text{Erf} \left(\frac{2\Delta - 2(z - z_c)}{2\sqrt{2}\sigma} \right) \right]. \end{aligned} \quad (4.25)$$

where B is the amplitude of the distribution in the second Brillouin zone.

Fig. 4.15 shows two illustrative examples how we extract the band population using the procedure described above. In fig. 4.15(a), all ^{40}K atoms have been loaded into the lowest Bloch band only and we therefore observe a single sharp momentum distribution in the vertical direction with the largest momentum given by $\hbar k$. Fig. 4.15(b) shows the corresponding radially integrated momentum distribution of ^{40}K atoms in the first Brillouin

zone. Although the edges of the momentum distribution are blurred due to the finite imaging resolution, it can clearly be seen that all atoms occupy momentum states within the first Brillouin zone.

Heating the atomic ^{40}K ensembles to temperatures in the 400 nK range, atoms will not only occupy the first but also the second Brillouin zone. This is shown in fig. 4.15(c) and (d). Now, atoms also occupy quasimomenta $-2\hbar k < q < 2\hbar k$ and we can extract the fraction of atoms in higher bands by fitting eq. 4.25 to the wedding cake structure and comparing the two areas underneath the fitting curve. From this, we determine the fraction of ^{40}K atoms in the second Brillouin zone to be approximately 28%.

It is known that collisions between atoms in higher bands and atoms in the lowest band induce very fast collisional loss in the sample, due to a two-body decay process [84]. To circumvent this issue and ensure the preparation of atoms in the lowest Bloch band only, we introduce a filtering procedure during the optical lattice loading. The filtering will result in fast tunneling of atoms in higher optical bands out of the optical lattice. Atoms in the lowest Bloch band will stay in the lattice. Our ramping procedure is shown in fig. 4.14, where the optical lattice is adiabatically ramped up in 150 ms to the height of $17.7 E_{rec}$. The atoms are held in the lattice for 130 ms and the dipole trap is adiabatically ramped down in 50 ms. The filtering is accomplished by ramping down the lattice in 20 ms holding it for 1 ms and then ramped down in $500 \mu\text{s}$ to $0 E_{rec}$, for the band mapping. In fig. 4.15a and b, I show the ^{40}K atoms all in the first Brillouin zone due to the filtering procedure. In order to filter atoms in the second band, the optical lattice height was reduced to $3.2 E_{rec}$. In fig. 4.15c and d, I show the ^{40}K atoms in the first and second Brillouin zones. The optical lattice height was reduced to $14.5 E_{rec}$. The filtering procedure was not used for molecules in the optical lattice.

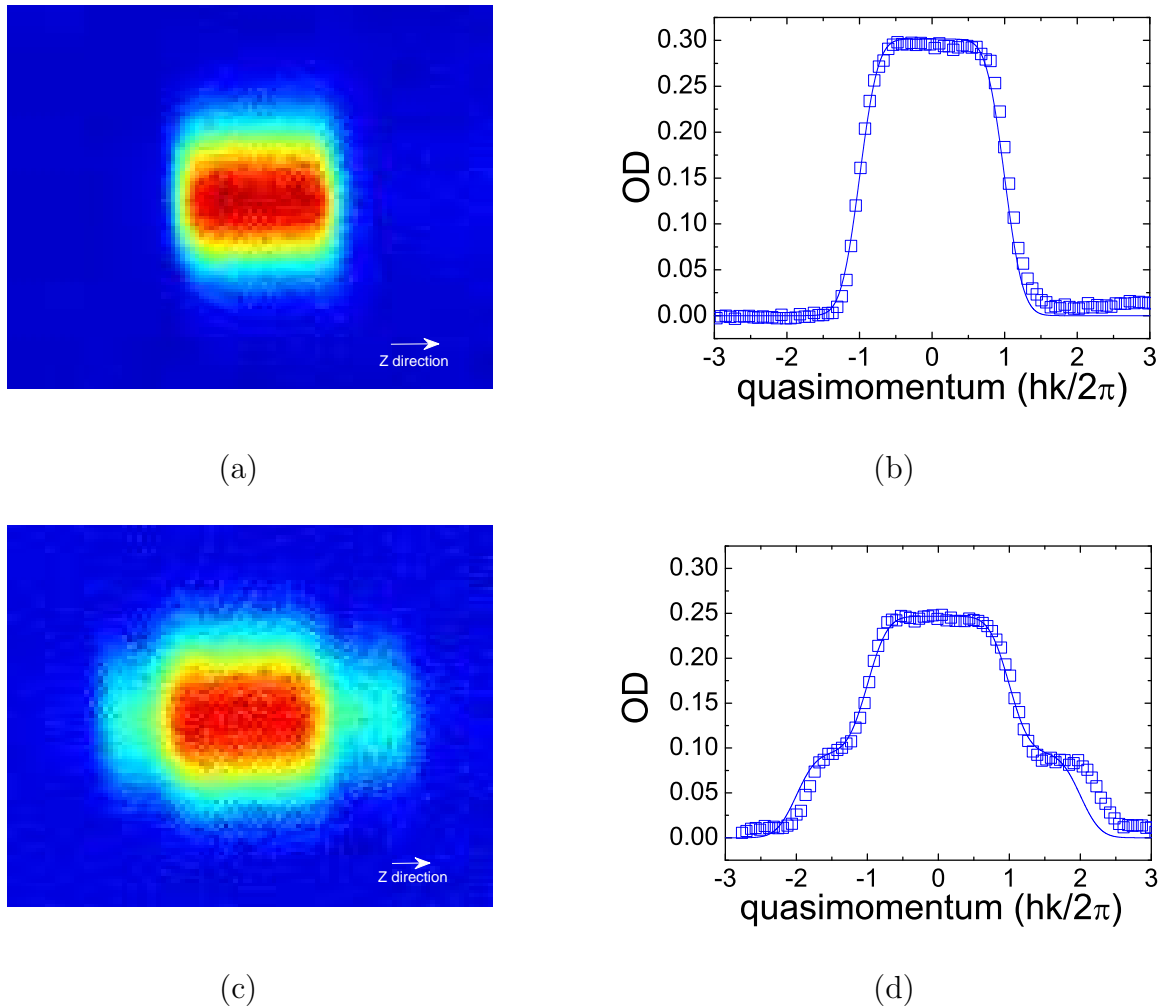


Figure 4.15: Band mapping for the filtering procedure with ^{40}K atoms. (a), and (c) are the atomic cloud images taken with time of flight of 18 ms. The initial temperature of the atoms in (a) is 350 nK and in (b) is 400 nK. The vertical profiles are shown in (b) and (d). In (b) all atoms are in the first Brillouin zone, while in (d) about 28% of the atoms are in the second Brillouin zone. However, a significantly difference in population of bands is observed in the two cases due to a different optical lattice heights ($3.2 E_{rec}$, and $14.5 E_{rec}$) applied for the filtering procedure(see fig. 4.14).

4.5 $^{40}\text{K}^{87}\text{Rb}$ molecules in the optical lattice

This thesis describes the control of collisional processes between polar molecules by means of control over the dipole moment and the confinement of the polar molecules in versatile geometries - in particular in a 2D geometry. As mentioned previously, tuning of the

trapping geometry from 3D to 2D is achieved in the experiment by gradually increasing the depth of an optical lattice and transferring molecules from a dipole trap to a 1D lattice.

In this section, we will describe how we prepare molecules in the lowest band of the optical lattice and how we control the population in different bands. Polar molecules are formed in the lattice following the ideas already outlined in chapter 2 and earlier sections of chapter 4. In the first step, we load atoms from the optical dipole trap into the optical lattice as described above. The optical lattice is ramped up adiabatically in 150 ms following an exponential ramp, then the dipole trap is ramped down within 150 ms. In the next step, we prepare Feshbach molecules in the optical lattice by ramping an external magnetic field through a Fano-Feshbach resonance. We subsequently transfer the Feshbach molecules to the rotational and vibrational ground state using STIRAP.

After preparing molecules in the optical lattice, we measure their heating rate. The result is shown in fig. 4.17. We observe a heating rate of 105(12) nK/s. The origin of this heating, which is an order of magnitude larger than what we measure for atoms is unknown. We speculate that extra heating might be induced by imperfections in the potential, formation of molecules in higher bands, anti-evaporation induced by number loss or non-adiabatic heating due to a sudden change of the external trapping potential.

For our experiments, we need a maximum number of molecules in the lowest band of the optical lattice. In order to optimize this number, we have experimentally compared different procedures for forming molecules in the optical lattice. The first procedure is to prepare molecules in the optical dipole trap first and then in a subsequent step load these molecules into the optical lattice as shown in fig. 4.18. To evaluate this procedure, we measured the number of molecules in the optical lattice versus the lattice depth. However, we observed a very fast loss after loading the molecules into the lattice. Presumably, this loss of molecules was due to a large fraction of the molecules accumulating in other than the lowest band of the optical lattice and fast s-wave two-body losses [84].

In the second experiment, we load atoms in the optical lattice and then convert atoms

into ground state molecules. The experimental sequence is shown in fig. 4.18. Fig. 4.19 (black open circles) shows the number of molecules prepared in the lowest band of the optical lattice versus the lattice depth at which the molecules are formed. As can be seen from fig. 4.19, the molecule number seems to be almost independent of the optical lattice depth. In the third measurement, we formed ground state molecules at different optical lattice heights and then finished to ramp the optical lattice up in 7 ms to a fixed final lattice height of $120 E_{rec}$ as shown in fig. 4.20. The measurement is shown in fig. 4.19 (red open squares). We implemented this procedure to maximize the number of molecules in the lowest band of the optical lattice. The number of molecules created in both cases are very similar to one another. We decided to prepare molecules by forming them in the optical lattice when its intensity is fully ramped up.

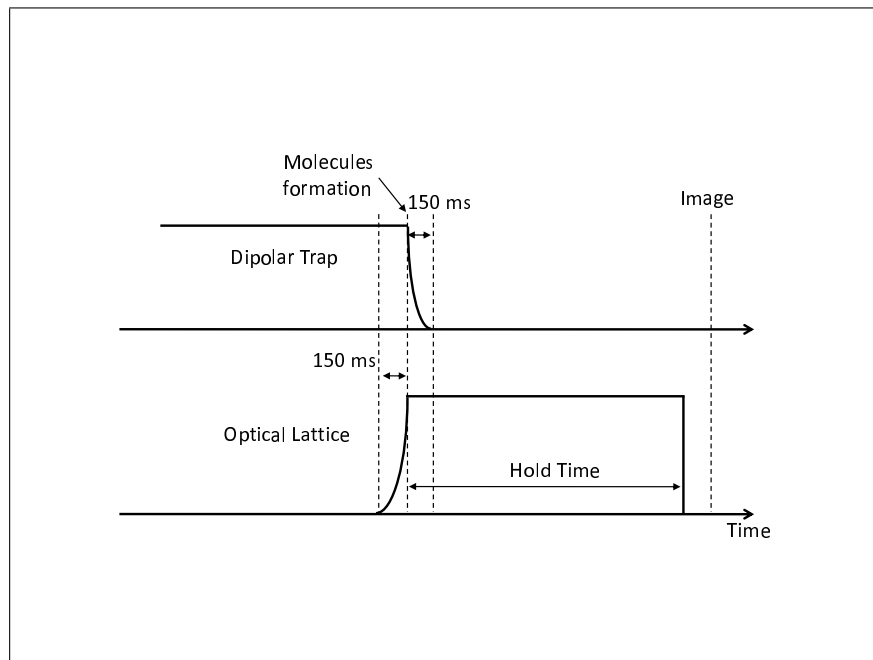


Figure 4.16: Ramping procedure for formation of ground state $^{40}\text{K}^{87}\text{Rb}$ molecules in the optical lattice. The final lattice depth is $60 E_{rec}^{KRb}$.

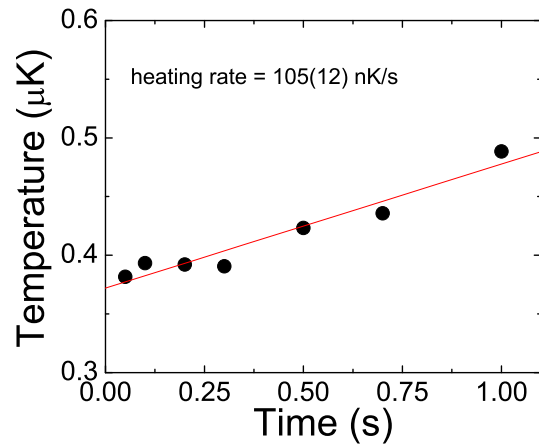


Figure 4.17: Heating rate for $^{40}\text{K}^{87}\text{Rb}$ in the optical lattice. The optical lattice depth is $60 E_{rec}^{KRb}$ depth.

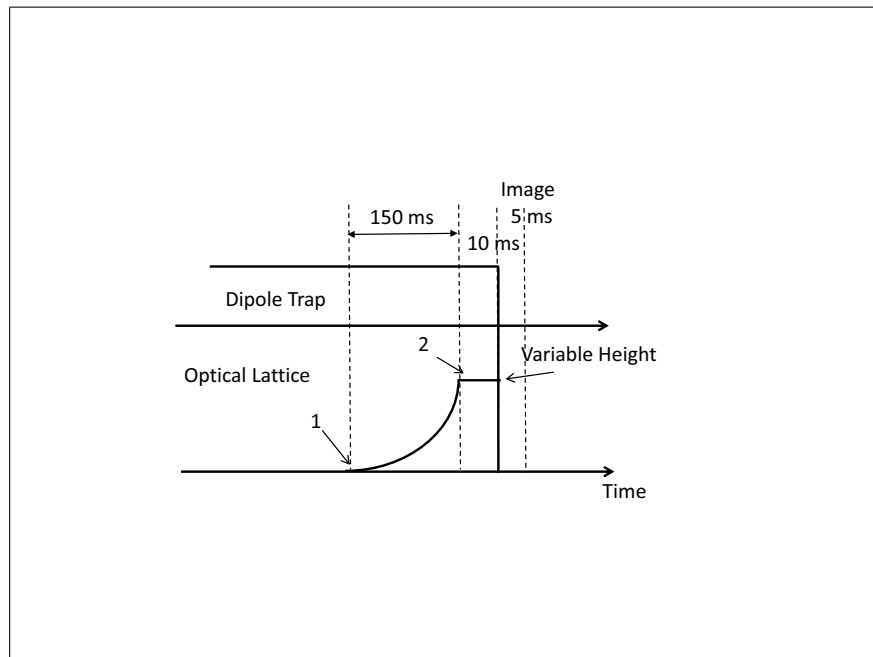


Figure 4.18: Ramp procedure for forming/loading ground state molecules in the optical lattice. The number 1 indicates where the ground state molecules are formed. Then the molecules are loaded in the optical lattice. The number 2 indicates where the ground state molecules are formed. In this case the molecules are formed in the fully ramped up optical lattice. The arrow with the note “Variable Height” means that the final value of the lattice is changed. The maximum height (depth) value that the lattice can go is $120 E_{rec}^{KRb}$.

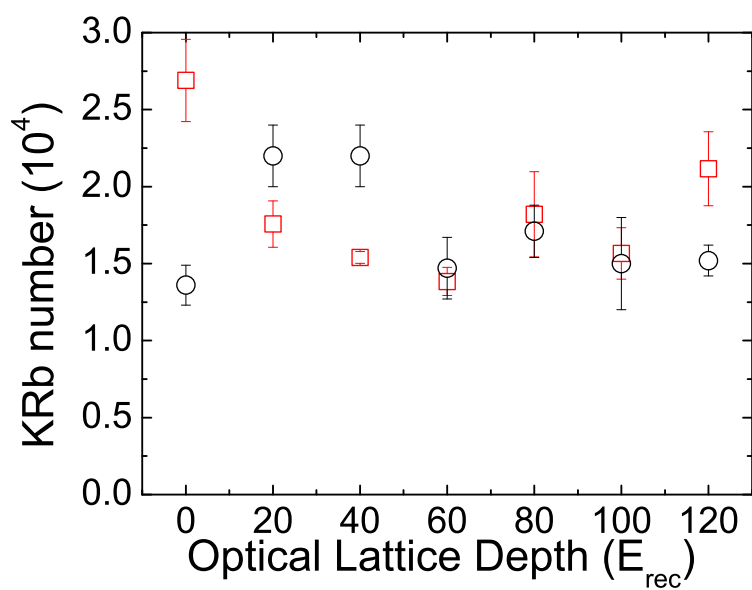


Figure 4.19: Measurement of the number of ground state molecules versus the optical lattice depth. The black open circles show the molecule number when the molecules are formed in the fully ramped-up optical lattice. The red open squares show the molecule number when the molecules are formed in the partially ramped up optical lattice.

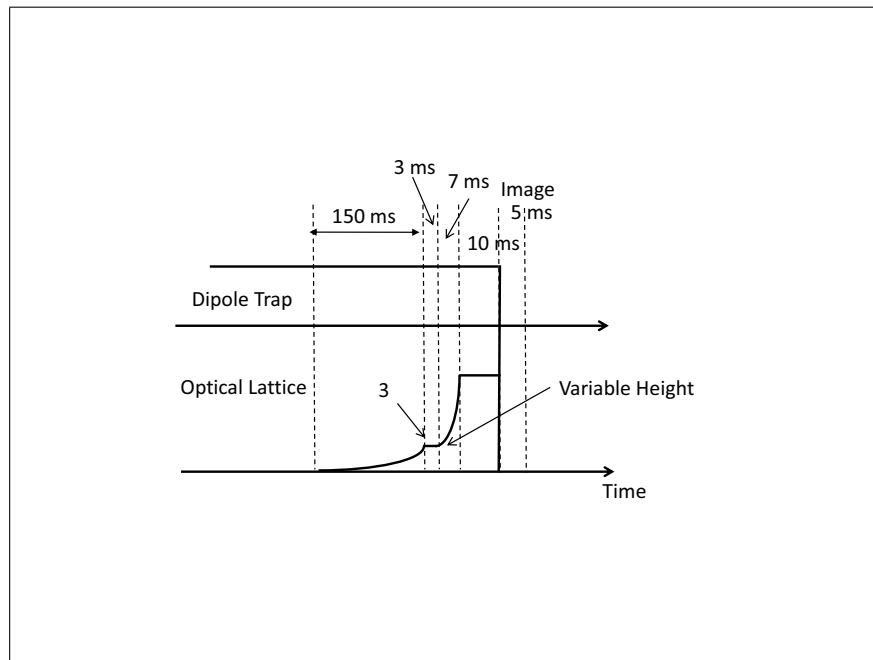


Figure 4.20: Ramp procedure for forming/loading ground state molecules in the optical lattice. The number 3 indicates where the ground state molecules are formed. The molecules are formed in a partially ramped up optical lattice. The arrow with the note “Variable Height” means that the partial value of the lattice is changed. The final height (depth) value of the lattice is $120 E_{rec}^{KRb}$.

Chapter 5

Suppression of Inelastic Collisions in 2D geometry

As we have shown in chapter 3, atom-exchange chemical reactions dominate the collisional dynamics in the ultracold molecular gas when the gas is confined in three dimensions (3D). The inelastic rate increases with increasing dipole moment and leads to a very fast loss of molecules from the gas and strong heating [40]. The inelastic loss processes dominate over elastic collisional processes, thereby preventing evaporative cooling of the molecular sample into quantum degeneracy. However, the chemical reactions are dominated by “head-to-tail” collisions between polar molecules where the attractive interactions between the dipoles significantly reduces the height of the p-wave collisional barrier. “Side-by-side” collisions should however be suppressed with increasing dipole moment. In this chapter, I report the suppression of inelastic “head-to-tail” collisions in the molecular sample by confining the molecules in a 2D geometry. This suppression of inelastic collisions by about 2 orders of magnitudes as compared to that in a 3D geometry promises to open the way towards evaporative cooling of polar molecules into quantum degeneracy.

In the following, I will discuss how attractive “head-to-tail” collisions can be controlled and suppressed by means of 2D spatial confinement. I will define the concept of stereodynamics and explain how the quantum statistics and the quasi-two-dimensional confinement come together to exclude certain collisional decay channels. I will then discuss our experiments with polar molecules in a 2D geometry. I will explore collisions between polar molecules in distinguishable and indistinguishable quantum states of motion and in particular discuss

the suppression of chemical reactions for $^{40}\text{K}^{87}\text{Rb}$ molecules confined in the optical lattice. Throughout this chapter, I closely follow reference [74], which describe our work.

5.1 Chemical Reaction Rates and Stereodynamics

Chemical reaction rates often depend strongly on stereodynamics, namely the orientation and translational movement of molecules in three-dimensional space [85, 86, 87]. An ultracold molecular gas, with a temperature below $1\ \mu\text{K}$, provides an unusual regime for chemistry, where polar molecules can be oriented using an external electric field and where, moreover, the motion of two colliding molecules is strictly quantized. As explained in chapter 3, atom-exchange reactions were observed in a trapped ultracold gas of $^{40}\text{K}^{87}\text{Rb}$ molecules [39]. In an external electric field, these exothermic and barrierless bimolecular reactions, $\text{KRb} + \text{KRb} \rightarrow \text{K}_2 + \text{Rb}_2$, occur at a rate that rises steeply with increasing dipole moment to the power of six [40]. The quantum stereodynamics of the ultracold collisions can be used to suppress the chemical reaction rate by nearly two orders of magnitude [74]. We use an optical lattice to confine fermionic polar molecules in a quasi-two-dimensional, pancake-like geometry, with the dipoles oriented along the tight confinement direction [33, 88], perpendicular to each pancake. With the combination of sufficiently tight confinement and Fermi statistics of the molecules, two polar molecules can approach each other only in a “side-by-side” collision, where the chemical reaction rate is suppressed by the repulsive dipole-dipole interaction. The suppression of the reaction rate requires quantum-state control of both the internal and external degrees of freedom of the molecules.

Two colliding polar molecules interact via long-range dipole-dipole forces well before they reach the shorter distance scales where chemical forces become relevant. Therefore, the spatial anisotropy of the dipolar interaction can play an essential role in the stereochemistry of bimolecular reactions of polar molecules. In general, one expects the attraction between oriented dipoles in a “head-to-tail” collision to be favorable for chemical reactions, while the repulsion between two oriented polar molecules in a “side-by-side” collision presents an

obstacle for reactions. Up to now, however, large center-of-mass collision energies have precluded the direct control of chemical reactions via dipolar interactions. In a cold collision regime, where tens of scattering partial waves contribute, one can begin to exert modifications of intermolecular dynamics through the dipolar effect [89]. An ultracold gas, however, provides an optimum environment in which to investigate dipolar effects [40, 90, 91]. Here, the $^{40}\text{K}^{87}\text{Rb}$ molecules are prepared in identical internal quantum states, with the dipoles oriented using an external electric field, and the molecular gas confined in external potentials created using light. In the limit of vanishing collision energies, the stereodynamics is described by only a few quantized collision channels, and, moreover, for indistinguishable molecules, the states of translational motion are coupled to internal molecular states due to the fact that the quantum statistics of the molecules (fermions or bosons) dictates a particular symmetry of the total wavefunction with respect to exchange of two molecules. In this quantum regime, we have an opportunity to suppress or enhance reaction rates by understanding and precisely controlling the stereodynamics of colliding polar molecules.

5.2 Collisions between Polar Molecules in Quasi-2D Geometry

The spatial geometry of the confining potential can influence collisions in a trapped gas of polar molecules. In particular, a two-dimensional (2D) trap geometry, with the dipoles oriented parallel to the tight confinement direction \hat{z} , is well-matched to the spatial anisotropy of the dipole-dipole interaction [92, 42, 43]. We can realize such a geometry using a one-dimensional optical lattice (see fig. 5.1 A), where the trapped molecules are divided among several isolated layers. In each of these layers, the lattice potential provides tight harmonic confinement in \hat{z} such that only the lowest few quantized motional states in \hat{z} are occupied. Consequently, within each isolated layer, colliding molecules approach each other in 2D. However, the range of the van der Waals interaction (and, for that matter, the range of dipolar interactions at our largest external electric field) is still smaller than the spatial extent of the cloud in the direction of tight confinement, a_{ho} , and, therefore, at short intermolecular

distances a collision still must be treated in three dimensions (3D).

We now consider the quantized collision channels that define the stereodynamics in this quasi-2D geometry. For intermolecular separations that are much larger than a_{ho} , the relative motion of the two molecules is described by a quantized angular momentum, $\hbar M$, around the \hat{z} axis, as well as by a quantized relative motion along \hat{z} . As discussed above, the stereodynamics of ultracold collisions of indistinguishable molecules is strongly influenced by the fact that the two-molecule wavefunction must obey an overall symmetry with respect to the exchange of the identical molecules. Following the formalism from reference [93], as molecules are identical, a overall wavefunction Ψ is constructed in a way that the molecular permutation operator P gives:

$$P\Psi = \epsilon_P\Psi, \quad (5.1)$$

where $\epsilon_P = 1$ for bosonic molecules and $\epsilon_P = -1$ for fermionic molecules. The overall wavefunction Ψ , has an internal wavefunction $|\alpha_1\alpha_2, \eta\rangle$, where α_1 and α_2 represent the electronic, vibrational, rotational and nuclear spin degrees of freedom of molecules 1 and 2, and the external wavefunction representing the confinement in one dimension, i.e., the confinement in the plane perpendicular to the \hat{z} direction, due to the optical lattice. The symmetrized states of the external wavefunction are given by:

$$|n_1n_2, \gamma\rangle = \frac{1}{\sqrt{2(1 + \delta_{n_1, n_2})}} [|n_1n_2\rangle + \gamma |n_2n_1\rangle], \quad (5.2)$$

where n_1 and n_2 are the harmonic oscillator states for molecules 1 and 2. For molecules in identical harmonic oscillator states $n_1 = n_2$, $\gamma = 1$, $\delta_{n_1, n_2} = 1$; for molecules in different states $n_1 \neq n_2$, $\delta_{n_1, n_2} = 0$, and $P|n_1n_2, \gamma\rangle = \gamma|n_1n_2, \gamma\rangle$. An essential aspect of relative motion in the plane perpendicular to the \hat{z} direction is the exchange symmetry of this part of the two-molecule wavefunction, which we identify with a quantum number γ . For the symmetric case, $\gamma = 1$ and for the antisymmetric case, $\gamma = -1$. For two molecules in the same \hat{z} harmonic oscillator state, $\gamma = 1$; while both $\gamma = 1$ and $\gamma = -1$ are possible for two molecules in different harmonic oscillator states. For the internal wavefunction, the

symmetrized states are given by:

$$|\alpha_1\alpha_2, \eta\rangle = \frac{1}{\sqrt{2(1 + \delta_{\alpha_1, \alpha_2})}} [|\alpha_1\alpha_2\rangle + \eta |\alpha_2\alpha_1\rangle], \quad (5.3)$$

where for molecules in the same internal states $\alpha_1 = \alpha_2$, $\delta_{\alpha_1, \alpha_2} = 1$, for molecules in different internal states $\alpha_1 \neq \alpha_2$, $\delta_{\alpha_1, \alpha_2} = 0$. Similarly, we use a quantum number η to keep track of the exchange symmetry of the part of the wavefunction that describes the internal states of the two molecules. For two molecules in the same internal quantum state, $\eta = 1$, while $\eta = \pm 1$ for molecules in different internal states.

In 2D, these three quantum numbers (M, γ, η) are sufficient to describe the quantum stereodynamics. However, because the interactions at short range must be described in 3D, the quantum number corresponding to the 3D angular momentum, L , as well as M , becomes relevant. With collisional channels described by quantum numbers η, L, γ , and M , the fermionic symmetry can be concisely stated in the following relations [93]:

$$\eta(-1)^L = -1, \quad \text{Short range, 3D} \quad (5.4)$$

$$\eta\gamma(-1)^M = -1. \quad \text{Long range, 2D} \quad (5.5)$$

For ultracold collisions where long range interactions play decisive roles, the chemical reaction rate will be dominated by the allowed collision channel with the lowest centrifugal barrier. Combining this fact with the relations above, we identify three collision channels relevant to the stereodynamics, and we label these $|1\rangle$, $|2\rangle$, and $|3\rangle$, in order of increasing centrifugal barrier heights. The dipole-dipole interaction mixes states with different L . However, for convenience, we will refer to the lowest energy adiabatic channel, which does not have a centrifugal barrier, as $L = 0$. Similarly, we will use $L = 1$ to denote the odd- L adiabatic channel with the lowest centrifugal barrier. Collision channel $|1\rangle$ has $\eta = -1$, $L = 0$, $\gamma = 1$, and $M = 0$, and corresponds to spatially isotropic collisions. Collision channel $|2\rangle$ has $\eta = 1$, $L = 1$, $\gamma = -1$, and $M = 0$, and is the quantum analog of “head-to-tail” collisions. Collision channel $|3\rangle$ has $\eta = 1$, $L = 1$, $\gamma = 1$, and $M = \pm 1$, and is the quantum analog of

“side-by-side” collisions. Fig. 5.1 B shows schematically the adiabatic potentials for these three lowest energy collision channels. Channels $|1\rangle$ and $|2\rangle$ become increasingly favorable for chemical reactions as the dipole-dipole interaction strength is increased, for example by increasing the external electric field \vec{E} . In contrast, channel $|3\rangle$ has a centrifugal barrier whose height increases for higher dipole moment, within the $|\vec{E}|$ range considered in this work. This barrier hence continues to prevent molecules from reaching short range.

Fig. 5.1 C shows how these different collision channels can be accessed through control of the internal molecular states and the \hat{z} motional states. In fig. 5.1 C, molecules in different internal states are shown in different colors and the harmonic oscillator states in \hat{z} are labeled by v . In case (1), for two molecules in different internal molecular states and in any combination of v levels, channel $|1\rangle$ is allowed when $\eta = -1$, resulting in no centrifugal barrier. In case (2), when the molecules are prepared in identical internal molecular states but in different v levels, the lowest energy collision channel is $|2\rangle$ (“head-to-tail”), which is allowed when $\gamma = -1$. In case (3), where the molecules are prepared in the same internal state and the same v level, the two lower energy collision channels are no longer allowed, and reactions can only proceed through channel $|3\rangle$ (“side-by-side”). This case is the least favorable for chemical reactions.

5.3 Band Mapping of Molecules

We create a trapped, ultracold gas of $^{40}\text{K}^{87}\text{Rb}$ molecules, in their lowest energy rovibrational level and in a single hyperfine state. To confine the molecules, we start with a crossed-beam optical dipole trap, with a harmonic trapping frequency of 180 Hz along the vertical direction (\hat{z}) and 25 Hz in the transverse directions. We ramp up the optical lattice along \hat{z} in 150 ms as shown in fig. 5.2. Both dipolar trap and optical lattice beams are linearly polarized and their polarizations are mutually orthogonal. The structure of the optical lattice is like a “stack of pancakes”. Each pancake (layer) of the optical lattice is tightly confining in \hat{z} with a harmonic trapping frequency of $\nu_z = 23$ kHz for the molecules;

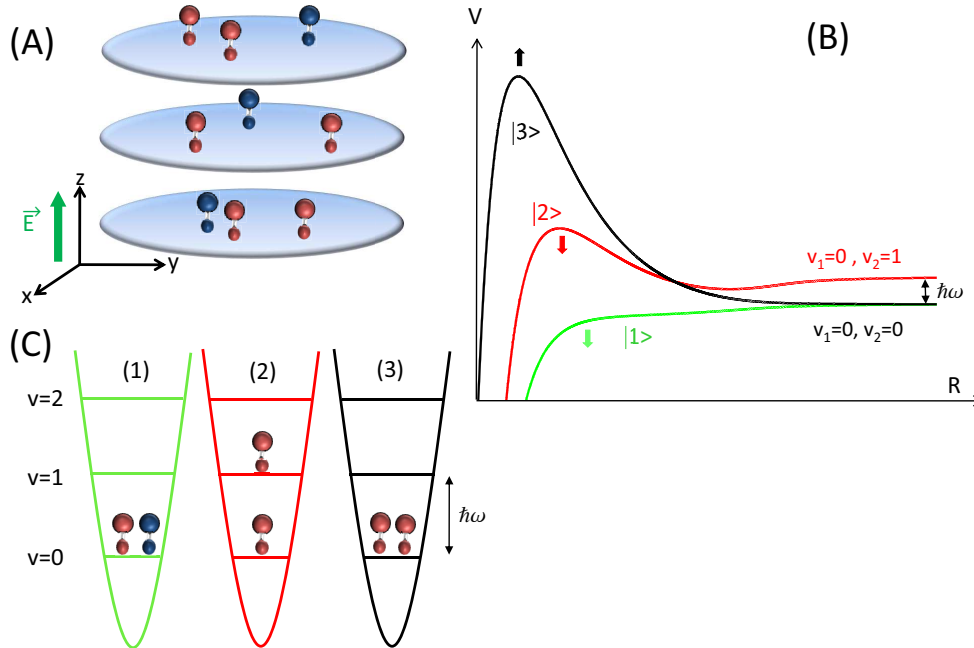


Figure 5.1: Quantized stereodynamics of ultracold chemical reactions in quasi-2D. (A) A quasi-2D geometry for collisions is realized for polar molecules confined in a one-dimensional optical lattice. An external electric field is applied along the tight confinement axis. (B) The lowest three adiabatic potentials for collisions are shown schematically as a function of the intermolecular separation, R . These three channels are ordered with increasing magnitude of the centrifugal barrier. The arrows indicate the change in the potential for an increasing external electric field, and hence a growing induced dipole moment. (C) Three different cases are shown schematically for each of the three lowest collision channels. The lowest energy collision channel occurs when two molecules are prepared in different internal states (indicated here by the colors of the molecules). The second channel is realized when two identical molecules are prepared in different vibrational levels v for their \hat{z} motions. The third case has a much reduced loss rate as a consequence of an increased centrifugal barrier when the two identical molecules are prepared in the same vibrational level along \hat{z} . Figure reproduced from reference [74].

while in the transverse directions, the combined trap has a harmonic trapping frequency of 36 Hz. The tunneling rate between lattice layers is negligible and, therefore, each layer realizes an isolated trap for the molecules. We begin with 34,000 ground-state molecules confined in roughly 23 layers, with the center layer having 2200 molecules and a peak density of $3.4 \times 10^7 \text{ cm}^{-2}$. The temperature of the molecular gas, T , in the combined dipole trap and optical

lattice can be varied between 500 nK and 800 nK by changing the initial atom gas conditions. To completely freeze out motion of the molecules along \hat{z} requires that $k_B T \ll h\nu_z$, where k_B is Boltzmann's constant. For a gas at $T = 800$ nK in our lattice, $\frac{k_B T}{h\nu_z} = 0.72$, and we expect 25% of the molecules will occupy higher v levels.

In order to control the bimolecular reactions in the ultracold gas, we need to control both the internal state and the harmonic oscillator level v of the molecules. We form the molecules in a single internal quantum state. The occupation of lattice levels v can be controlled by changing the temperature T . We can also prepare a non-thermal distribution of molecules using parametric heating. The parametric heating is done by modulating the lattice intensity at twice ν_z in a 300 μs time window as shown in fig. 5.2. As result, a fraction of molecules initially in the $v = 0$ level are excited to the $v = 2$ level.

The population in each lattice level is determined by using an adiabatic band-mapping technique [94, 82]. As shown in fig. 5.2, the lattice potential is ramped down slowly, molecules in different vibrational levels of the lattice are mapped onto Brillouin zones, with corresponding quasi momenta of $\pm k\hbar$, $\pm 2k\hbar$, etc. The measured molecule momentum distribution following this ramp is shown in fig. 5.3 A for a $T = 800$ nK molecular gas. The measured fraction in $v = 0$ matches well with the expected thermal distribution. The thermal distribution is calculated using the Boltzmann distribution:

$$f(v, T) = \frac{\exp(-\frac{0.5h\nu_z}{k_B T})}{\sum_v \exp(-\frac{(v+0.5)h\nu_z}{k_B T})}, \quad (5.6)$$

where v is the vibrational level number. In contrast, Fig. 5.3 B shows the measured non-equilibrium occupation of lattice vibrational levels following parametric heating.

As discussed in chapter 4, the density distribution of the molecules in the vertical direction can be recovered from the image by fitting with the result of a convolution between a Gaussian function and a Heaviside function. It is given by:

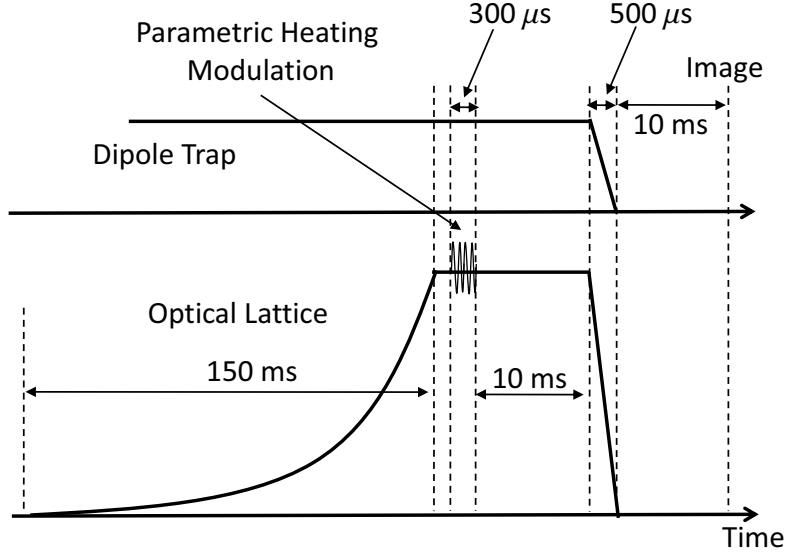


Figure 5.2: Ramp procedure for transferring atoms from the dipole trap to an optical lattice as well as for band mapping for molecules. Molecules are formed after an 150 ms adiabatic ramp. A non-thermal distribution is created by using parametric heating by pulsing a sinusoidal wave with $300 \mu\text{s}$. The band mapping is done by linearly ramping down in $500 \mu\text{s}$. To image the molecules, we reverse our coherent transfer process to bring the molecules back to a weakly bound state where we can detect the molecules with time-of-flight absorption imaging [26].

$$\begin{aligned}
 f(x) = & A/2 \left[\text{Erf} \left(\frac{\Delta + 2(z - z_c)}{2\sqrt{2}\sigma} \right) + \text{Erf} \left(\frac{\Delta - 2(z - z_c)}{2\sqrt{2}\sigma} \right) \right] + \\
 & B/2 \left[\text{Erf} \left(\frac{-\Delta + 2(z - z_c)}{2\sqrt{2}\sigma} \right) + \text{Erf} \left(\frac{-\Delta - 2(z - z_c)}{2\sqrt{2}\sigma} \right) \right] + \\
 & B/2 \left[\text{Erf} \left(\frac{2\Delta + 2(z - z_c)}{2\sqrt{2}\sigma} \right) + \text{Erf} \left(\frac{2\Delta - 2(z - z_c)}{2\sqrt{2}\sigma} \right) \right] + \\
 & C/2 \left[\text{Erf} \left(\frac{3\Delta + 2(z - z_c)}{2\sqrt{2}\sigma} \right) + \text{Erf} \left(\frac{-2\Delta - 2(z - z_c)}{2\sqrt{2}\sigma} \right) \right] + \\
 & C/2 \left[\text{Erf} \left(\frac{-2\Delta + 2(z - z_c)}{2\sqrt{2}\sigma} \right) + \text{Erf} \left(\frac{3\Delta - 2(z - z_c)}{2\sqrt{2}\sigma} \right) \right], \quad (5.7)
 \end{aligned}$$

where A , B , and C , are the amplitudes of the 1st, 2nd, and 3rd Brillouin zones, d is the center of the distribution, σ is the image resolution, and x is the variable of the function. Δ is the size of the distribution in the Brillouin zone, $\pm\hbar k$. $\Delta = \frac{2\hbar k}{m} \frac{T_{tof}}{5.44\mu\text{m}/\text{pix}}$, where T_{tof} is the time of flight, m is the mass of $^{40}\text{K}^{87}\text{Rb}$, and $5.44 \mu\text{m}$ is the corresponding value in micrometers per pixel at the image. A , B , and C , are given in units of OD (optical density). Since the image coordinates are given in pixels, the fit gives, z_c , z , Δ , and σ are all given in pixel units. Then, the axial coordinate is converted to quasimomentum units $\hbar k$. The free parameters of the fitting function are A , B , C , z_c , and σ .

The relative population in each vibrational level of the optical lattice is given by the area of the distribution in a momentum zone divided by the total area of the distribution. Since these zones have the same width along the quasimomentum axis, we can use only the amplitudes to calculate the relative population on each band. The relative molecules population in the optical lattice are given by:

$$\frac{n_0}{n_{tot}} = \frac{A}{A + B + C}, \quad (5.8)$$

$$\frac{n_1}{n_{tot}} = \frac{B}{A + B + C}, \quad (5.9)$$

$$\frac{n_2}{n_{tot}} = \frac{C}{A + B + C}, \quad (5.10)$$

where, n_0 , n_1 , and n_2 are the initial populations in the three first bands, and n_{tot} is the total initial population.

The traces in fig. 5.3 were obtained by averaging the images in the transverse direction within one rms width of the Gaussian distribution. We fit the traces with eq. 5.7. The uncertainty in the relative population is 3%, and is dominated by systematic errors arising from the variation of the imaging resolution within the range of 1 to 2 pixels.

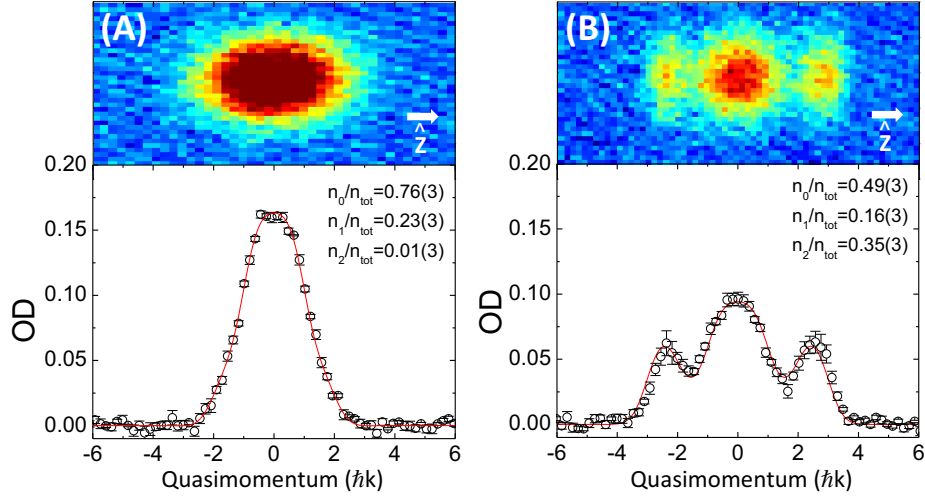


Figure 5.3: Relative population of molecules in the lattice vibrational levels. We measure the relative population in each lattice vibrational level using a band-mapping technique. The results are shown for (A) a thermal distribution of molecules and (B) a non-thermal distribution created by parametric heating in \hat{z} . The two images use the same color scale for the optical depth (OD). The images are an average of 5 shots and 7 shots for (A) and (B), respectively, taken after 10 ms of free expansion. Below each image we show a trace along \hat{z} that corresponds to the OD averaged over the transverse direction. A fit (red line) to the trace, which takes into account both the size of the Brillouin zones and our imaging resolution, is used to extract the relative populations, n_v/n_{tot} , in each lattice level v . The horizontal axis corresponds to momentum in \hat{z} and is marked in units of the lattice momentum $\hbar k$, where k is the lattice wavevector. Figure reproduced from reference [74].

5.4 Suppression of Inelastic Collisions in the Optical Lattice

We measure the chemical reaction rate by monitoring the loss of trapped molecules as a function of time. We follow the ramp procedure shown in fig. 5.4. The molecules are imaged after being released and freely expanding from the combined dipolar trap and optical lattice. From the images, we obtain the total number of molecules and the radial cloud size. Since we do not resolve the individual layers of the optical lattice, we obtain

an average 2D density per layer. The average 2D density is obtained by dividing the total number of molecules, N , by an effective area, $4\pi\alpha\sigma_r^2$, where σ_r is the rms cloud size in the transverse direction and N/α is a number-weighted average over the occupied lattice layers. We calculate $\alpha(t=0) = 23$ assuming an initial discrete Gaussian distribution in \hat{z} with an rms width that we measure after transferring the molecules back to the optical dipole trap. However, α increases at longer times because of the density dependence of the loss. For our analysis, we use a time-averaged value $\alpha = 30$ that was determined by comparing an analysis based on a uniform layer density to a numerical simulation of the loss in each layer. The uncertainties for the loss rate coefficients are dominated by statistical uncertainties in the fits to $n_{\text{tot}}(t)$.

In fig. 5.5 A, we show the average 2D density as a function of time. For these data, the molecules are all prepared in the same internal state and $|\vec{E}|$ is 4 kV/cm, which gives an induced molecular dipole moment of 0.158 Debye (D), where $1\text{D} = 3.336 \times 10^{-30}$ C·m. The two data sets in fig. 5.5 A correspond to an unperturbed $T = 800$ nK gas (black squares) and a parametrically heated gas (red circles). For the case where parametric heating was used to increase population in $v > 0$ levels, the data show a faster initial loss of molecules. This suggests that the initial loss is predominately due to interlevel collisions as described in case (2) of fig. 5.1 C, while intralevel collisions (case (3) of fig. 5.1 C) give a slower loss of molecules at longer times.

We fit the data using a simple model, which assumes two loss rate constants: one for interlevel collisions, $\beta_{|2\rangle}$, and a second one for intralevel collisions, $\beta_{|3\rangle}$ (with the subscripts referring to the adiabatic channels labeled in fig. 5.1 B). Here,

$$\begin{aligned}\frac{dn_0}{dt} &= -\beta_{|3\rangle}n_0^2 - \beta_{|2\rangle}n_0n_1 - \beta_{|2\rangle}n_0n_2, \\ \frac{dn_1}{dt} &= -\beta_{|2\rangle}n_0n_1 - \beta_{|3\rangle}n_1^2 - \beta_{|2\rangle}n_1n_2, \\ \frac{dn_2}{dt} &= -\beta_{|2\rangle}n_0n_2 - \beta_{|2\rangle}n_1n_2 - \beta_{|3\rangle}n_2^2,\end{aligned}\tag{5.11}$$

where n_v is the 2D density of molecules in a particular lattice vibrational level v . To fit the

measured time dependence of the total 2D density, $n_{\text{tot}}(t)$, we use $n_{\text{tot}}(t) = n_0(t) + n_1(t) + n_2(t)$. We input the measured initial populations n_v/n_{tot} (see fig. 5.3) at $t = 0$, and we fit the data to the numerical solution of eq. 5.11. We obtain $\beta_{|3\rangle}$ and $\beta_{|2\rangle}$ from a simultaneous fit to the two measured $n_{\text{tot}}(t)$ curves shown in fig. 5.5 A.

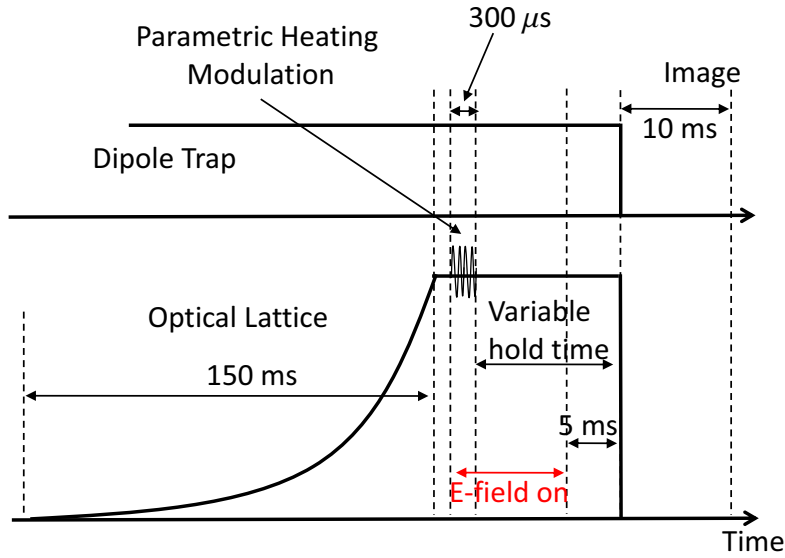


Figure 5.4: Ramp procedure for measurement of chemical reaction rates. The $^{40}\text{K}^{87}\text{Rb}$ molecules are produced when the optical lattice is fully formed at $\approx 100 E_{\text{rec}}$, after 150 ms ramp time. The molecules can be excited to higher vibrational levels of the optical lattice via parametric heating. The parametric heating is done via a sinusoidal modulation of the lattice intensity for $300 \mu\text{s}$. The electric field is turned on together with the parametric heating and it is turned off 5 ms before we switch off the dipolar trap and the optical lattice. The molecules are held in the combined dipolar trap and the optical lattice for a variable time. After the molecules are released from the trap, the image is taken after 10 ms time of flight.

By repeating this procedure for different values of $|\vec{E}|$, we measure the chemical reac-

tion rate constants, $\beta_{|3\rangle}$ and $\beta_{|2\rangle}$, as a function of the induced dipole moment. In fig. 5.5 B, we show the intralevel (black squares) and interlevel (red circles) chemical rate constants as a function of the dipole moment. Also shown as green triangles in fig. 5.5 B are the results of two measurements for a 50/50 mixture of molecules in two different rotational states (case (1) of fig. 5.1 C) $|0, 0, -4, 1/2\rangle$ and $|1, 1, -4, 1/2\rangle$. The 50/50 mixture is created by using a $\pi/2$ microwave pulse when the molecules are in the ground state. The notation used here is $|N, m_N, m_I^K, m_I^{Rb}\rangle$, where N is the rotational quantum number, m_N is the projection of the rotational quantum number on the applied electric field direction, and $m_I^{Rb/K}$ is the nuclear spin quantum number as in reference [65]. Here, we fit the loss of molecules in the ground rotational state to the solution of $\frac{dn_{\text{tot}}}{dt} = -\beta_{|1\rangle}n_{\text{tot}}^2$ to extract a single loss rate constant.

For comparison with these measurements, Goulven Qummer and John Bohn perform quantum scattering calculations using a time-independent quantum formalism based on spherical coordinates with cylindrical asymptotic matching to describe the molecular collisions in quasi-2D [93]. We use an absorbing potential at short distance to represent chemical reactions [42, 67]. This technique showed excellent agreement with previous experimental data for $^{40}\text{K}^{87}\text{Rb}$ bimolecular reactions in 3D [39, 40]. We computed the loss rate coefficients β_{v_1, v_2} for molecules in different initial lattice vibrational states v_1, v_2 , at a collision energy of 800 nK. When the induced dipole moment is still small (0 - 0.2 D), the measured temperature is a good approximation for the mean collision energy. The loss rates of the different processes can be separated into fast loss rates ($\beta_{0,1}, \beta_{0,2}, \beta_{1,2} \approx \beta_{|2\rangle}$) and slow loss rates ($\beta_{0,0}, \beta_{1,1}, \beta_{2,2} \approx \beta_{|3\rangle}$). The black theoretical curve in fig. 5.5 B corresponds to an average of the slow rates weighted by the initial populations n_0, n_1, n_2 :

$$\beta_{black} = \beta_{0,0} - (\beta_{0,0} - \beta_{1,1})\zeta_1^2, \quad (5.12)$$

where $\zeta_1 = n_1/n_{\text{tot}}$ is the percentage of the initial relative population in the lattice vibrational state $v = 1$. The red curve corresponds to the same average but for the fast rates. The green

curve corresponds to the loss rate of molecules in different internal states.

$$\beta_{red} = \frac{\beta_{0,1}\zeta_0\zeta_1 + \beta_{0,2}\zeta_0\zeta_2 + \beta_{1,2}\zeta_1\zeta_2}{\eta_0\zeta_1 + \zeta_0\zeta_2 + \zeta_1\zeta_2}. \quad (5.13)$$

The three measured reaction rate constants shown in fig. 5.5 B are consistent with the quantum scattering calculations for the collision channels shown in matching colors in fig. 5.1 B and fig. 5.1 C. Molecules in different rotational states (green triangles in fig. 5.5 B) have the highest rate for chemical reactions, consistent with the fact that they can collide in channel $|1\rangle$, which corresponds to spatially isotropic collisions with no centrifugal barrier. On the other hand, molecules prepared in the same internal molecular state (red circles and black squares in fig. 5.5 B) have suppressed reaction rates because the lowest energy collision channel ($|1\rangle$) is no longer allowed. Instead, identical molecules in different lattice levels (red circles in fig. 5.5 B) react predominantly through collisions in channel $|2\rangle$, or “head-to-tail”, while identical molecules in the same lattice level (black squares in fig. 5.5 B) react through collisions in channel $|3\rangle$, or “side-by-side”. The importance of stereodynamics on the reaction rate for polar molecules is manifest in the very different dipole-moment dependence of the reactions rates in these two collision channels. In particular, for the case where the molecules are prepared both in the same internal quantum state and in the same v level, the reaction rate is suppressed even as the dipole moment is increased.

Fig. 5.6 shows how the initial loss rate in a gas of identical molecules depends on the fractional occupation of the lowest lattice level, n_0/n_{tot} . As n_0/n_{tot} increases, the calculated initial loss rate constant for a molecular gas in thermal equilibrium (solid black line) changes from close to $\beta_{|2\rangle}$ (the red line indicating the measured value at 0.174 D from fig. 5.5 B) to $\beta_{|3\rangle}$ (open point at $n_0/n_{tot} = 1$). In thermal equilibrium, the fractional occupation of the lowest vibrational level is given by the Boltzmann distribution. For the solid black line in fig. 5.6, the fractional molecular population $f(v, T)$ in a vibrational level v at temperature T is obtained from a Boltzmann distribution, and the effective $\beta_{initial}$ is then calculated as

$$\beta_{initial} = \beta_{|3\rangle} \sum_v f(v, T)^2 + \beta_{|2\rangle} \sum_{v_1 \neq v_2} f(v_1, T)f(v_2, T). \quad (5.14)$$

On the top axis of fig. 5.6, we give the corresponding values of the scaled temperature $\frac{k_B T}{h\nu_z}$. The solid triangles in fig. 5.6 correspond to the measured initial loss rate at different temperatures (500 nK and 800 nK), while the open symbol at $n_0/n_{\text{tot}} \approx 0.5$ corresponds to the initial loss rate for the parametrically heated, non-thermal molecular gas.

We directly compare the suppressed chemical reaction rate in quasi-2D to the 3D case in the inset to fig. 5.6. Here, we compare data for a 3D geometry from reference [40] against the suppressed loss rate constant measured in quasi-2D. For the comparison, the 2D loss rate is scaled to 3D using $\beta_{3D} = \sqrt{\pi} a_{ho} \beta_{2D}$ [95, 96, 43], where a_{ho} is the harmonic oscillator length in \hat{z} , $a_{ho} = \sqrt{\frac{\hbar}{m\omega_z}}$. For a dipole moment d greater than 0.1 D, the 3D loss rate constant increases dramatically as d^6 [40, 41], whereas the scaled loss rate constant for the quasi-2D case remains close to the value at zero electric field. At a dipole moment of 0.174 D, the measured suppression in quasi-2D is a factor of 60.

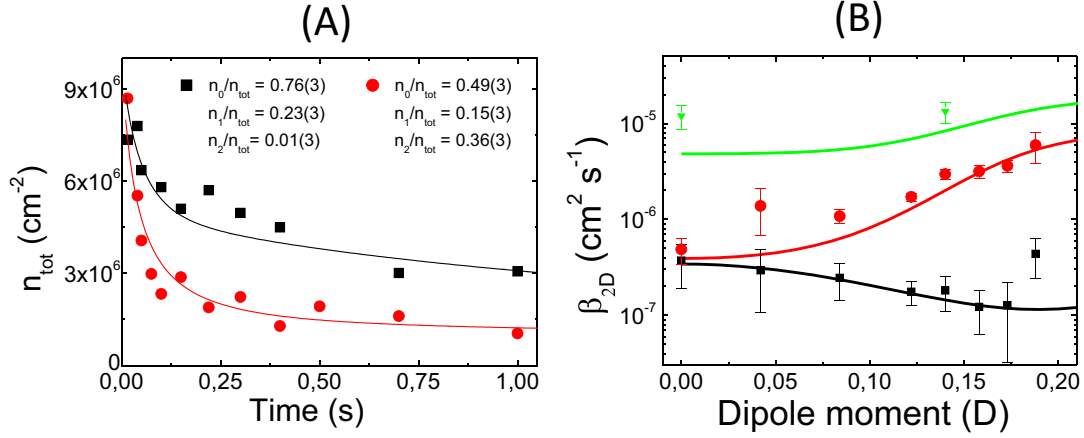


Figure 5.5: Measurements of 2D loss rates and comparison with theory. (A) A fit (solid lines) to the measured loss curves, with (red circles) and without (black squares) 0.3 ms of parametric heating in \hat{z} , is used to extract the loss rate constants $\beta_{\{3\}}$ and $\beta_{\{2\}}$. (B) The extracted loss rate constants for collisions of molecules in the same lattice vibrational level (black squares) and from different lattice vibrational levels (red circles) are plotted for several dipole moments. Measured loss rate constants for molecules prepared in different internal states are shown as green triangles. For comparison with each of these three measurements, we include a quantum scattering calculation for $\nu_z = 23$ kHz, $T = 800$ nK (solid lines). The potentials corresponding to the dominant loss channel for the three cases are shown in matching colors in fig. 5.1 B. Figure reproduced from reference [74].

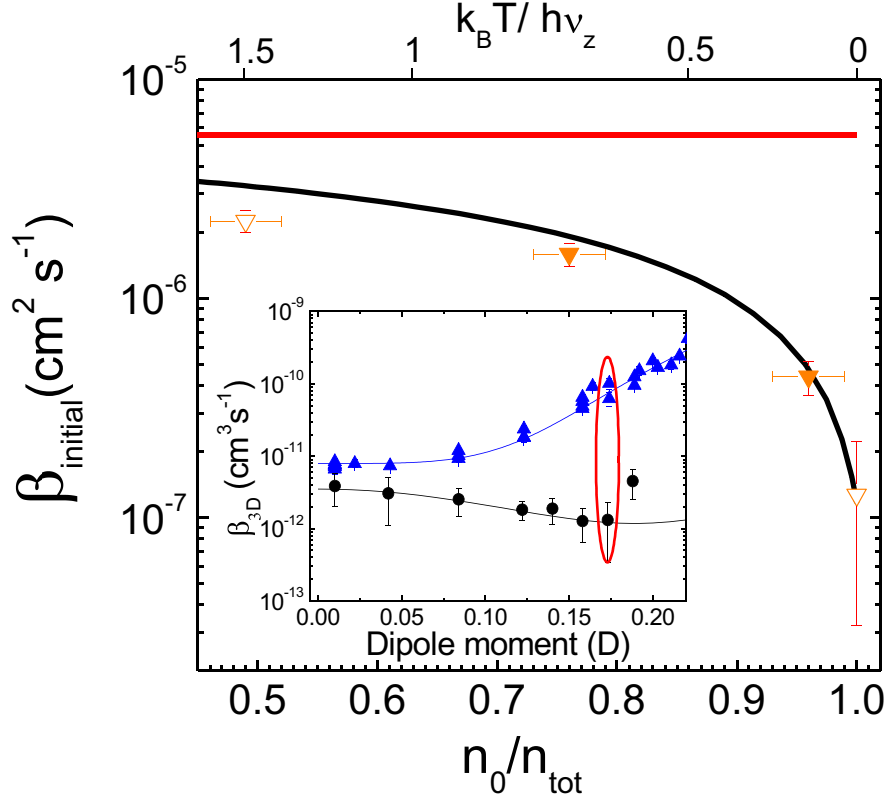


Figure 5.6: Loss rates from 3D to 2D. The effective initial loss rate, β_{initial} , for polar molecules confined in a 2D geometry depends on the fractional population (n_0/n_{tot}) in the lowest harmonic oscillator level in \hat{z} , which for a gas in thermal equilibrium depends on the ratio $\frac{k_B T}{h\nu_z}$. The measured initial loss rates for a dipole moment of 0.174 D are displayed for two different thermal distributions (solid triangles), a non-thermal sample created by parametric heating (the top open triangle), and an extracted pure $\beta_{|3\rangle}$ when the entire population is residing in the lattice ground vibrational level (the bottom open triangle). The experimental results agree well with a simple model (black curve) described in this section. The top line indicates the value of $\beta_{|2\rangle}$ as measured in fig. 5.5 B. (Inset) The intralevel loss rate for identical fermionic $^{40}\text{K}^{87}\text{Rb}$ molecules in 2D (black circles) is compared with the loss rate in 3D (blue triangles). The 3D data for $T = 300$ nK are borrowed from reference [40]. The 2D data were taken at $T = 800$ nK and are converted to 3D rates by multiplication with $\sqrt{\pi}a_{ho}$, where a_{ho} is the harmonic oscillator length in \hat{z} . Figure reproduced from reference [74].

Chapter 6

Conclusion and Future Work

6.1 Conclusion

In this thesis I have presented experimental advances of a dense, ultracold, and near quantum degenerate polar gas of $^{40}\text{K}^{87}\text{Rb}$. For dipolar molecules in a 3D geometry, the chemical reaction loss was seen scale with the dipole moment to the power of six [40], due to attractive dipole-dipole interactions via “head-to-tail” collisions. The main result demonstrated in this thesis is that the inelastic collisions can be suppressed when the molecules are confined in a quasi-2D geometry in a one-dimensional optical lattice. Compared to dipole-dipole collisions in 3D geometry, collisions in quasi-2D geometry under appropriate state preparations can suppress the inelastic loss by about two orders of magnitude [74]. We control the population in the optical lattice of the motional states, which makes it possible to observe collisions with single components of the p-partial wave.

6.2 Future work

For future work with these $^{40}\text{K}^{87}\text{Rb}$ molecules there are many possibilities for new exciting experiments:

- Anisotropic rethermalization: observe rethermalization of the molecular cloud between the two transverse directions (\hat{x} and \hat{y}) in this 2D geometry.
- Measurement of the elastic cross section of molecules: when the molecular cloud

rethermalizes. We can directly measure the rate of rethermalization as a function of the dipole moment. This will let us determine the elastic cross section for dipolar collisions as proposed by Bohn *et al.* [72].

- Realization of quantum degenerate polar gas of $^{40}\text{K}^{87}\text{Rb}$: With the first two steps accomplished, it is possible to reach quantum degenerate regime for a gas of polar molecules via evaporative cooling.
- Detection of chemical reaction products: so far, we only detect molecular loss. However, the vacuum chamber could be designed with an ion detector to enable detection of ultracold chemical reactions products.
- Detecting novel quantum phases in the geometry of stacked 2D traps [33, 34, 35, 97, 88, 98].

Bibliography

- [1] K.-K. Ni, S. Ospelkaus, D. Wang, G. Quéméner, B. Neyenhuis, M. H. G. de Miranda, J. L. Bohn, J. Ye, and D. S. Jin, Dipolar collisions of polar molecules in the quantum regime, *Nature* **464**, 1324 (2010).
- [2] K.-K. Ni, S. Ospelkaus, M. H. G. de Miranda, A. Pe'er, B. Neyenhuis, J. J. Zirbel, S. Kotochigova, P. S. Julienne, D. S. Jin, and J. Ye, A High Phase-Space-Density Gas of Polar Molecules, *Science* **322**, 231 (2008).
- [3] K. W. Holman, Distribution of an Ultrastable Frequency Reference Using Optical Frequency Combs, Ph.D. thesis, University of Colorado at Boulder, 2005.
- [4] S. Ospelkaus, K.-K. Ni, M. H. G. de Miranda, B. Neyenhuis, D. Wang, S. Kotochigova, P. S. Julienne, D. S. Jin, and J. Ye, Ultracold polar molecules near quantum degeneracy, *Faraday Discussions* **142**, 351 (2008).
- [5] S. Ospelkaus, K.-K. Ni, D. Wang, M. H. G. de Miranda, B. Neyenhuis, G. Quéméner, P. S. Julienne, J. L. Bohn, D. S. Jin, and J. Ye, Quantum-State Controlled Ultracold Chemistry, *Science* **327**, 853 (2010).
- [6] M. H. G. de Miranda, A. Chotia, B. Neyenhuis, D. Wang, G. Quéméner, S. Ospelkaus, J. L. Bohn, J. Ye, and D. S. Jin, Controlling the quantum stereodynamics of ultracold bimolecular reactions, (submitted. (2010)).
- [7] C. N. Cohen-Tannoudji, Nobel Lecture: Manipulating atoms with photons, *Rev. Mod. Phys.* **70**, 707 (1998).
- [8] S. Chu, Nobel Lecture: The manipulation of neutral particles, *Rev. Mod. Phys.* **70**, 685 (1998).
- [9] W. D. Phillips, Nobel Lecture: Laser cooling and trapping of neutral atoms, *Rev. Mod. Phys.* **70**, 721 (1998).
- [10] M. H. Anderson, J. R. Ensher, M. R. Matthews, C. E. Wieman, and E. A. Cornell, Observation of Bose-Einstein Condensation in a Dilute Atomic Vapor, *Science* **269**, 198 (1995).

- [11] W. Ketterle, Nobel lecture: When atoms behave as waves: Bose-Einstein condensation and the atom laser, *Rev. Mod. Phys.* **74**, 1131 (2002).
- [12] E. A. Cornell and C. E. Wieman, Nobel Lecture: Bose-Einstein condensation in a dilute gas, the first 70 years and some recent experiments, *Rev. Mod. Phys.* **74**, 875 (2002).
- [13] K. B. Davis, M. O. Mewes, M. R. Andrews, N. J. van Druten, D. S. Durfee, D. M. Kurn, and W. Ketterle, Bose-Einstein Condensation in a Gas of Sodium Atoms, *Phys. Rev. Lett.* **75**, 3969 (1995).
- [14] B. DeMarco and D. S. Jin, Onset of Fermi Degeneracy in a Trapped Atomic Gas, *Science* **285**, 1703 (1999).
- [15] S. Inouye, M. R. Andrews, J. Stenger, H.-J. Miesner, D. M. Stamper-Kurn, and W. Ketterle, Observation of Feshbach resonances in a Bose-Einstein condensate, *Nature* **392**, 151 (1998).
- [16] C. A. Regal, M. Greiner, and D. S. Jin, Observation of Resonance Condensation of Fermionic Atom Pairs, *Phys. Rev. Lett.* **92**, 040403 (2004).
- [17] M. W. Zwierlein, C. A. Stan, C. H. Schunck, S. M. F. Raupach, A. J. Kerman, and W. Ketterle, Condensation of Pairs of Fermionic Atoms near a Feshbach Resonance, *Phys. Rev. Lett.* **92**, 120403 (2004).
- [18] M. Bartenstein, A. Altmeyer, S. Riedl, S. Jochim, C. Chin, J. H. Denschlag, and R. Grimm, Collective Excitations of a Degenerate Gas at the BEC-BCS Crossover, *Phys. Rev. Lett.* **92**, 203201 (2004).
- [19] E. A. Donley, N. R. Claussen, S. T. Thompson, and C. E. Wieman, Atom-molecule coherence in a Bose-Einstein condensate, *Nature* **417**, 529 (2002).
- [20] C. Chin, A. J. Kerman, V. Vuletić, and S. Chu, Sensitive Detection of Cold Cesium Molecules Formed on Feshbach Resonances, *Phys. Rev. Lett.* **90**, 033201 (2003).
- [21] S. Y. T. van de Meerakker, P. H. M. Smeets, N. Vanhaecke, R. T. Jongma, and G. Meijer, Deceleration and Electrostatic Trapping of OH Radicals, *Phys. Rev. Lett.* **94**, 023004 (2005).
- [22] M. T. Hummon, W. C. Campbell, H.-I. Lu, E. Tsikata, Y. Wang, and J. M. Doyle, Magnetic trapping of atomic nitrogen (N^{14}) and cotrapping of NH ($X\Sigma - 3$), *Phys. Rev. A* **78**, 050702 (2008).
- [23] B. C. Sawyer, B. K. Stuhl, D. Wang, M. Yeo, and J. Ye, Molecular Beam Collisions with a Magnetically Trapped Target, *Phys. Rev. Lett.* **101**, 203203 (2008).
- [24] J. M. Sage, S. Sainis, T. Bergeman, and D. DeMille, Optical Production of Ultracold Polar Molecules, *Phys. Rev. Lett.* **94**, 203001 (2005).

- [25] K. Bergmann, H. Theuer, and B. W. Shore, Coherent population transfer among quantum states of atoms and molecules, *Rev. Mod. Phys.* **70**, 1003 (1998).
- [26] A. Pe'er, E. A. Shapiro, M. C. Stowe, M. Shapiro, and J. Ye, Precise Control of Molecular Dynamics with a Femtosecond Frequency Comb, *Phys. Rev. Lett.* **98**, 113004 (2007).
- [27] K.-K. Ni, A Quantum Gas of Polar Molecules, Ph.D. thesis, University of Colorado at Boulder, 2009.
- [28] T. Köhler, K. Góral, and P. S. Julienne, Production of cold molecules via magnetically tunable Feshbach resonances, *Rev. Mod. Phys.* **78**, 1311 (2006).
- [29] S. Ospelkaus, A. Peér, K.-K. Ni, J. J. Zirbel, B. Neyenhuis, S. Kotochigova, P. S. Julienne, J. Ye, and D. S. Jin, Efficient state transfer in an ultracold dense gas of heteronuclear molecules, *Nat Phys* **4**, 622 (2008).
- [30] J. G. Danzl, E. Haller, M. Gustavsson, M. J. Mark, R. Hart, N. Bouloufa, O. Dulieu, H. Ritsch, and H.-C. Nagerl, Quantum Gas of Deeply Bound Ground State Molecules, *Science* **321**, 1062 (2008).
- [31] F. Lang, K. Winkler, C. Strauss, R. Grimm, and J. H. Denschlag, Ultracold Triplet Molecules in the Rovibrational Ground State, *Phys. Rev. Lett.* **101**, 133005 (2008).
- [32] T. Udem, J. Reichert, R. Holzwarth, and T. W. Hänsch, Absolute Optical Frequency Measurement of the Cesium *D*₁ Line with a Mode-Locked Laser, *Phys. Rev. Lett.* **82**, 3568 (1999).
- [33] D. J. Jones, S. A. Diddams, J. K. Ranka, A. Stentz, R. S. Windeler, J. L. Hall, and S. T. Cundiff, Carrier-Envelope Phase Control of Femtosecond Mode-Locked Lasers and Direct Optical Frequency Synthesis, *Science* **288**, 635 (2000).
- [34] S. T. Cundiff and J. Ye, Colloquium: Femtosecond optical frequency combs, *Rev. Mod. Phys.* **75**, 325 (2003).
- [35] F. Dalfovo, S. Giorgini, L. P. Pitaevskii, and S. Stringari, Theory of Bose-Einstein condensation in trapped gases, *Rev. Mod. Phys.* **71**, 463 (1999).
- [36] J. Stuhler, A. Griesmaier, T. Koch, M. Fattori, T. Pfau, S. Giovanazzi, P. Pedri, and L. Santos, Observation of Dipole-Dipole Interaction in a Degenerate Quantum Gas, *Phys. Rev. Lett.* **95**, 150406 (2005).
- [37] T. Lahaye, T. Koch, B. Fröhlich, M. Fattori, J. Metz, A. Griesmaier, S. Giovanazzi, and T. Pfau, Strong dipolar effects in a quantum ferrofluid, *Nature* **448**, 672 (2007).
- [38] H. P. Büchler, E. Demler, M. Lukin, A. Micheli, N. Prokof'ev, G. Pupillo, and P. Zoller, Strongly Correlated 2D Quantum Phases with Cold Polar Molecules: Controlling the Shape of the Interaction Potential, *Phys. Rev. Lett.* **98**, 060404 (2007).

- [39] L. Santos, G. V. Shlyapnikov, P. Zoller, and M. Lewenstein, Bose-Einstein Condensation in Trapped Dipolar Gases, *Phys. Rev. Lett.* **85**, 1791 (2000).
- [40] G. Pupillo, A. Micheli, H. P. Büchler, and P. Zoller, *Cold Molecules: Theory, Experiment, Applications* (Taylor & Francis, Boca Raton, 2009).
- [41] D. DeMille, Quantum Computation with Trapped Polar Molecules, *Phys. Rev. Lett.* **88**, 067901 (2002).
- [42] S. F. Yelin, K. Kirby, and R. Côté, Schemes for robust quantum computation with polar molecules, *Phys. Rev. A* **74**, 050301 (2006).
- [43] A. André, D. DeMille, J. M. Doyle, M. D. Lukin, S. E. Maxwell, P. Rabl, R. J. Schoelkopf, and P. Zoller, A coherent all-electrical interface between polar molecules and mesoscopic superconducting resonators, *Nat Phys* **2**, 636 (2006).
- [44] G. Quémener and J. L. Bohn, Strong dependence of ultracold chemical rates on electric dipole moments, *Phys. Rev. A* **81**, 022702 (2010).
- [45] G. Quémener and J. L. Bohn, Electric field suppression of ultracold confined chemical reactions, *Phys. Rev. A* **81**, 060701 (2010).
- [46] A. Micheli, Z. Idziaszek, G. Pupillo, M. A. Baranov, P. Zoller, and P. S. Julienne, Universal Rates for Reactive Ultracold Polar Molecules in Reduced Dimensions, *Phys. Rev. Lett.* **105**, 073202 (2010).
- [47] J. J. Zirbel, K.-K. Ni, S. Ospelkaus, T. L. Nicholson, M. L. Olsen, P. S. Julienne, C. E. Wieman, J. Ye, and D. S. Jin, Heteronuclear molecules in an optical dipole trap, *Phys. Rev. A* **78**, 013416 (2008).
- [48] J. Zirbel, Ultracold Fermionic Feshbach Molecules, Ph.D. thesis, University of Colorado at Boulder, 2008.
- [49] S. Ospelkaus, C. Ospelkaus, L. Humbert, K. Sengstock, and K. Bongs, Tuning of Heteronuclear Interactions in a Degenerate Fermi-Bose Mixture, *Phys. Rev. Lett.* **97**, 120403 (2006).
- [50] J. J. Zirbel, K.-K. Ni, S. Ospelkaus, J. P. D’Incao, C. E. Wieman, J. Ye, and D. S. Jin, Collisional Stability of Fermionic Feshbach Molecules, *Phys. Rev. Lett.* **100**, 143201 (2008).
- [51] A. Marian, M. C. Stowe, J. R. Lawall, D. Felinto, and J. Ye, United Time-Frequency Spectroscopy for Dynamics and Global Structure, *Science* **306**, 2063 (2004).
- [52] M. J. Thorpe, K. D. Moll, R. J. Jones, B. Safdi, and J. Ye, Broadband Cavity Ringdown Spectroscopy for Sensitive and Rapid Molecular Detection, *Science* **311**, 1595 (2006).
- [53] A. D. Ludlow *et al.*, Sr Lattice Clock at 1×10^{-16} Fractional Uncertainty by Remote Optical Evaluation with a Ca Clock, *Science* **319**, 1805 (2008).

- [54] S. M. Foreman, A. D. Ludlow, M. H. G. de Miranda, J. E. Stalnaker, S. A. Diddams, and J. Ye, Coherent Optical Phase Transfer over a 32-km Fiber with 1 s Instability at 10^{-17} , *Phys. Rev. Lett.* **99**, 153601 (2007).
- [55] R. J. Jones, K. D. Moll, M. J. Thorpe, and J. Ye, Phase-Coherent Frequency Combs in the Vacuum Ultraviolet via High-Harmonic Generation inside a Femtosecond Enhancement Cavity, *Phys. Rev. Lett.* **94**, 193201 (2005).
- [56] J. K. Ranka, R. S. Windeler, and A. J. Stentz, Visible continuum generation in air-silica microstructure optical fibers with anomalous dispersion at 800 nm, *Opt. Lett.* **25**, 25 (2000).
- [57] M. G. Littman and H. J. Metcalf, Spectrally narrow pulsed dye laser without beam expander, *Appl. Opt.* **17**, 2224 (1978).
- [58] C. J. Hawthorn, K. P. Weber, and R. E. Scholten, Littrow configuration tunable external cavity diode laser with fixed direction output beam, *Rev. Sci. Instrum.* **72**, 4477 (2001).
- [59] D. Wang, B. Neyenhuis, M. H. G. de Miranda, K.-K. Ni, S. Ospelkaus, D. S. Jin, and J. Ye, Direct absorption imaging of ultracold polar molecules, *Phys. Rev. A* **81**, 061404 (2010).
- [60] H. A. Bethe, Theory of Disintegration of Nuclei by Neutrons, *Phys. Rev.* **47**, 747 (1935).
- [61] E. P. Wigner, On the Behavior of Cross Sections Near Thresholds, *Phys. Rev.* **73**, 1002 (1948).
- [62] N. Balakrishnan and A. Dalgarno, Chemistry at ultracold temperatures, *Chemical Physics Letters* **341**, 652 (2001).
- [63] J. M. Hutson and P. Soldn, Molecular collisions in ultracold atomic gases, *International Reviews in Physical Chemistry* **26**, 1 (2007).
- [64] P. S. Julienne, Ultracold molecules from ultracold atoms: a case study with the KRb molecule, *Faraday Discussions* **142**, 361 (2009).
- [65] S. Kotochigova, Dispersion interactions and reactive collisions of ultracold polar molecules, *New Journal of Physics* **12**, 073041 (2010).
- [66] S. Ospelkaus, K.-K. Ni, G. Quéméner, B. Neyenhuis, D. Wang, M. H. G. de Miranda, J. L. Bohn, J. Ye, and D. S. Jin, Controlling the Hyperfine State of Rovibronic Ground-State Polar Molecules, *Phys. Rev. Lett.* **104**, 030402 (2010).
- [67] J. Aldegunde, B. A. Rivington, P. S. Żuchowski, and J. M. Hutson, Hyperfine energy levels of alkali-metal dimers: Ground-state polar molecules in electric and magnetic fields, *Phys. Rev. A* **78**, 033434 (2008).
- [68] Z. Idziaszek and P. S. Julienne, Universal Rate Constants for Reactive Collisions of Ultracold Molecules, *Phys. Rev. Lett.* **104**, 113202 (2010).

- [69] P. Langevin, , *Ann. Chim. Phys.* **5**, 245 (1905).
- [70] Z. Idziaszek and P. S. Julienne, Universal Rate Constants for Reactive Collisions of Ultracold Molecules, *Phys. Rev. Lett.* **104**, 113202 (2010).
- [71] N. Masuhara, J. M. Doyle, J. C. Sandberg, D. Kleppner, T. J. Greytak, H. F. Hess, and G. P. Kochanski, Evaporative Cooling of Spin-Polarized Atomic Hydrogen, *Phys. Rev. Lett.* **61**, 935 (1988).
- [72] C. R. Monroe, E. A. Cornell, C. A. Sackett, C. J. Myatt, and C. E. Wieman, Measurement of Cs-Cs elastic scattering at $T=30 \mu\text{K}$, *Phys. Rev. Lett.* **70**, 414 (1993).
- [73] J. L. Bohn, M. Cavagnero, and C. Ticknor, Quasi-universal dipolar scattering in cold and ultracold gases, *New Journal of Physics* **11**, 055039 (2009).
- [74] B. DeMarco, J. L. Bohn, J. P. Burke, M. Holland, and D. S. Jin, Measurement of p -Wave Threshold Law Using Evaporatively Cooled Fermionic Atoms, *Phys. Rev. Lett.* **82**, 4208 (1999).
- [75] R. Grimm, M. Weidemller, and Y. B. Ovchinnikov, Optical Dipole Traps for Neutral Atoms, *Advances In Atomic, Molecular, and Optical Physics* **42**, 95 (2000).
- [76] H. Moritz, One-dimensional Atomic Gases, Ph.D. thesis, Swiss Federal Institute of Technology, Zurich, 2006.
- [77] M. Greiner, Ultracold quantum gases in three-dimensional lattice potentials, Ph.D. thesis, Ludwig Maximilians Universitaet Muenchen, 2003.
- [78] A. M. Rey, UltraCold Bosonic Atoms in Optical lattices, Ph.D. thesis, University of Maryland College Park, 2004.
- [79] B. Gadway, D. Pertot, R. Reimann, M. G. Cohen, and D. Schneble, Analysis of Kapitza-Dirac diffraction patterns beyond the Raman-Nath regime, *Opt. Express* **17**, 19173 (2009).
- [80] J. H. Denschlag, J. E. Simsarian, H. Häffner, C. McKenzie, A. Browaeys, D. Cho, K. Helmerson, S. L. Rolston, and W. D. Phillips, A Bose-Einstein condensate in an optical lattice, *J. Phys. B: At. Mol. Opt. Phys.* **35**, 3095 (2002).
- [81] M. Ben Dahan, E. Peik, J. Reichel, Y. Castin, and C. Salomon, Bloch Oscillations of Atoms in an Optical Potential, *Phys. Rev. Lett.* **76**, 4508 (1996).
- [82] M. Greiner, I. Bloch, O. Mandel, T. W. Hänsch, and T. Esslinger, Exploring Phase Coherence in a 2D Lattice of Bose-Einstein Condensates, *Phys. Rev. Lett.* **87**, 160405 (2001).
- [83] M. Köhl, H. Moritz, T. Stöferle, K. Günter, and T. Esslinger, Fermionic Atoms in a Three Dimensional Optical Lattice: Observing Fermi Surfaces, Dynamics, and Interactions, *Phys. Rev. Lett.* **94**, 080403 (2005).

- [84] I. B. Spielman, P. R. Johnson, J. H. Huckans, C. D. Fertig, S. L. Rolston, W. D. Phillips, and J. V. Porto, Collisional deexcitation in a quasi-two-dimensional degenerate bosonic gas, *Phys. Rev. A* **73**, 020702 (2006).
- [85] R. N. Zare, Laser Control of Chemical Reactions, *Science* **279**, 1875 (1998).
- [86] J. Aldegunde, M. P. de Miranda, J. M. Haigh, B. K. Kendrick, V. Sáez-Rábanos, and F. J. Aoiz, How Reactants Polarization Can Be Used to Change and Unravel Chemical Reactivity, *The Journal of Physical Chemistry A* **109**, 6200 (2005).
- [87] A. Gijsbertsen, H. Linnartz, C. A. Taatjes, and S. Stolte, Quantum Interference as the Source of Steric Asymmetry and Parity Propensity Rules in NORare Gas Inelastic Scattering, *Journal of the American Chemical Society* **128**, 8777 (2006), pMID: 16819871.
- [88] A. Micheli, G. Pupillo, H. P. Büchler, and P. Zoller, Cold polar molecules in two-dimensional traps: Tailoring interactions with external fields for novel quantum phases, *Phys. Rev. A* **76**, 043604 (2007).
- [89] B. C. Sawyer, B. K. Stuhl, M. Yeo, T. V. Tscherbul, M. T. Hummon, Y. Xia, J. Klos, D. Patterson, J. M. Doyle, and J. Ye, Cold heteromolecular dipolar collisions, *arXiv:1008.5127* (2010).
- [90] R. V. Krems, Molecules near absolute zero and external field control of atomic and molecular dynamics, *International Reviews in Physical Chemistry* **24**, 99 (2005).
- [91] L. D. Carr, D. DeMille, R. V. Krems, and J. Ye, Cold and ultracold molecules: science, technology and applications, *New Journal of Physics* **11**, 055049 (2009).
- [92] C. Ticknor, Quasi-two-dimensional dipolar scattering, *Phys. Rev. A* **81**, 042708 (2010).
- [93] G. Quémener and J. L. Bohn, Dynamics of molecules in confined geometry and electric field, *manuscript in preparation* (2010).
- [94] A. Kastberg, W. D. Phillips, S. L. Rolston, R. J. C. Spreeuw, and P. S. Jessen, Adiabatic Cooling of Cesium to 700 nK in an Optical Lattice, *Phys. Rev. Lett.* **74**, 1542 (1995).
- [95] D. S. Petrov and G. V. Shlyapnikov, Interatomic collisions in a tightly confined Bose gas, *Phys. Rev. A* **64**, 012706 (2001).
- [96] Z. Li and R. V. Krems, Inelastic collisions in an ultracold quasi-two-dimensional gas, *Phys. Rev. A* **79**, 050701 (2009).
- [97] B. Capogrosso-Sansone, C. Trefzger, M. Lewenstein, P. Zoller, and G. Pupillo, Quantum Phases of Cold Polar Molecules in 2D Optical Lattices, *Phys. Rev. Lett.* **104**, 125301 (2010).
- [98] M. Baranov, Theoretical progress in many-body physics with ultracold dipolar gases, *Physics Reports* **464**, 71 (2008).